Simulations of Molecular Clouds: Resolution Requirements and Core Formation

INAUGURAL-DISSERTATION

zur
Erlangung des Doktorgrades
der Mathematisch-Naturwissenschaftlichen Fakultät
der Universität zu Köln

vorgelegt von

Prabesh Raj Joshi
aus Baglung, Nepal

Köln 2019

Berichterstatter (Gutachter):
Prof. Dr. Stefanie Walch-Gassner
Prof. Dr. Peter Schilke

Vorsitzender der Komission:
Prof. Dr. Joachim Saur

Tag der mündlichen Prüfung:
28 März, 2019

For my parents and sisters

Abstract

The formation of molecular hydrogen (H_2) and carbon monoxide (CO) is sensitive to the volume and column density distribution of the turbulent interstellar medium. In order to obtain correct numerical approximations of the molecular cloud formation in nature, simulations that couple the gas dynamics and chemical evolution are gaining popularity over the last decade. However, a comprehensive study on the spatial resolution required to model different molecules is missing. The simulations presented in this thesis are designed to investigate the resolution requirements for a converged formation history of H_2 and CO molecules and serve to indicate whether such requirements have been met in existing studies.

For this purpose, the FLASH code is used to study H_2 and CO formation in a large set of hydrodynamical simulations of periodic boxes with driven supersonic turbulence and of colliding flows. The simulations include a non-equilibrium chemistry network, gas self-gravity, and diffuse radiative transfer. The resolution requirements are determined by identifying two critical conditions for numerical modelling: the simulation has to at least resolve the densities at which (1) the molecule formation time in each cell in the computational domain is equal to the dissociation time, and (2) the formation time is equal to the typical cell-crossing time. These requirements are affected by the composition of the gas as well as by the strength of turbulence and interstellar radiation field in the molecule forming regions. For the solar metallicity gas, which is subject to a solar neighbourhood interstellar radiation field and typical velocity dispersion observed in molecular clouds, the second criterion is found to be more restrictive, for both H_2 and CO formation. The numerical results and derived resolution criteria indicate that a spatial resolution of $\lesssim 0.2$ pc is sufficient for converged H_2 formation; the required resolution for CO convergence is $\lesssim 0.04$ pc. The expressions for the resolution requirements derived in this thesis can be used to check whether molecule formation is converged in any given simulation.

Finally, the chemically and dynamically resolved simulation of molecular clouds is used to investigate the formation of massive molecular cloud cores. The cores are found to accrete gas from the parent cloud primarily along designated channels defined by the filamentary structures in the molecular clouds.

Zusammenfassung

Die Entstehung von molekularem Wasserstoff (H_2) und Kohlen-Monoxid (CO) hängt sensitive mit der Volumendichte und Säulendichte Verteilung im interstellaren Medium zusammen. Um eine korrekte numerische Näherung der Entstehung von Molekülwolken zu erhalten, wurden im letzten Jahrzehnt Simulationen erstellt, die die Gasdynamik mit einer chemischen Evolution verbinden. Jedoch steht bist dato eine Untersuchung über die benötigte Auflösung aus, die benötigt wird um gewisse Moleküle zu modellieren. Simulationen in dieser Arbeit untersuchen die Anforderungen an die Auflösung, mit welcher die Bildung von H_2 und CO konvergiert. Es wird auch überprüft, ob vorangegangene Studien diese Erfordernisse erfüllen.

Dazu werden hydrodynamische Simulationen mit dem FLASH Code durchgeführt. Das oben genannte wird sowohl in periodischen Boxen mit getriebener super-sonischer Turbulenz oder von “colliding flow” Szenarios untersucht. Die Simulationen beinhalten ein chemisches Netzwerk im Nicht-Gleichgewicht, Selbstgravitation des Gases und Strahlungstransfer von diffuser Strahlung. Die nötige Auflösung wird durch zwei kritische Bedingungen identifiziert wobei die Zeit zur Bildung gleich der (1) Dissoziationszeit und (2) der typischen Informationszeit in einer Zelle sein muss. Diese Bedingungen sind abhängig von der Zusammensetzung des Gases sowie der Stärke der Turbulenz und des interstellaren Strahlungsfeldes. Wobei das zweite Kriterium in Umgebungen ähnlich der solaren Nachbarschaft als deutlich einschränkender gilt. Sowohl die Auswertung der numerischen Simulationen als auch der theoretischen Überlegungen ergeben räumliche Auflösungen von $\lesssim$ 0.2 pc bzw. $\lesssim$ 0.04 pc, die benötigt werden um die Entstehung von H_2 bzw. CO korrekt abzubilden. Erstmalig kann damit in Simulationen die Bildung von Molekülen auf Konvergenz überprüft werden.

Daraus werden chemisch und dynamisch aufgelöste Simulationen abgeleitet, in welchen die Entstehung von molekularen Kernen in Molekülwolken untersucht wird. Dabei zeigt sich, dass diese Kerne Gas ihrer Umgebung entlang vorgegebener Kanäle akkretieren. Die Ausrichtung der Kanäle entspricht der von filamentären Strukturen in der Wolke.

CONTENTS

1 INTRODUCTION **1**

2 THEORY OF THE INTERSTELLAR MEDIUM **3**

2.1 The composition of the ISM 3

2.2 Phases of the ISM 4

2.2.1 Heating and cooling in the ISM 4

2.3 Molecular clouds (MCs) 7

2.4 Molecular cloud cores 9

3 THE CHEMICAL EVOLUTION IN MOLECULAR CLOUDS **10**

3.1 Importance of H_2 and CO 10

3.2 H_2 formation and destruction 12

3.3 CO formation and destruction 13

3.4 The effect of turbulence on the MC chemistry 15

4 SIMULATION OF MOLECULAR CLOUD FORMATION **17**

4.1 Magneto-hydrodynamics (MHD) 17

4.2 Chemistry networks in simulations 19

4.3 Self-gravity 22

4.4 Dust and molecular shielding 23

4.5 Turbulence 24

4.6 Tracer particles 25

4.7 Simulation resolution 26

5 SIMULATION SETUP **30**

5.1 Turbulent box 30

5.2 Colliding flow 34

6 GENERAL PROPERTIES OF THE SIMULATED CLOUDS **39**

6.1 Column density distribution 39

6.2 Mean gas density 41

6.3 Mean velocity dispersion 42
6.4 Resolution effects on the gas structure 43
6.5 Chapter summary 46

7 CHEMICAL EVOLUTION IN TB SIMULATIONS **47**

7.1 Column density distribution 47
7.2 Evolution of H_2 in TB setup 50
7.3 Evolution of CO in TB setup 52
7.4 Density distribution 55
7.5 Chapter summary 58

8 CHEMICAL EVOLUTION IN CF SIMULATIONS **59**

8.1 The choice of the collision interface 59
8.2 Column density distribution 60
8.3 Evolution of H_2 in CF setup 63
8.4 Evolution of CO in CF setup 65
8.5 Density distribution 67
8.6 Chapter summary 68

9 RESOLUTION CRITERIA TO MODEL MOLECULE FORMATION **69**

9.1 Condition 1: Physical condition 70
9.2 Condition 2: Dynamical condition 71
9.3 Resolution requirements in CF runs 73
9.4 Resolution requirements in TB runs 78
9.5 Chapter summary 81

10 ASPECTS OF THE RESOLUTION CRITERIA **82**

10.1 A case of fast molecule dissociation 82
10.2 A general expression for the physical condition 84
10.3 The molecular content of unresolved dense regions 88
10.4 The effect of velocity dispersion 91
10.5 Time evolution of a fluid element 93
10.6 Fluid element through a region 95
10.7 Chapter summary 97

11 FORMATION OF MC CORES **98**

11.1 Identification of MC cores 98

11.2 Accretion onto the cores 100

11.3 Chapter summary 111

12 CONCLUSION **112**

13 PROSPECTS AND OUTLOOK **115**

1 | Introduction

The interstellar medium (ISM) is the combination of atoms, molecules, ions, electrons, dust, electromagnetic field, and cosmic rays, found in between the stars in a galaxy. It is not a standalone environment but a dynamical location where stars form, live, and eventually cease to exist.

In the ISM, the star formation process begins with the interaction between the atoms, molecules, charged particles, and dust. These interactions are mainly facilitated by feedback process such as ionizing radiation or supernova explosions from the existing stars. Besides the stars, the differential rotation of the galaxy, the accretion and outflow of matter from galaxies, or even mergers between galaxies affect the evolution of the ISM. It takes millions of years for the dilute and diffuse ISM to produce relatively dense structures like molecular clouds (MCs) via gravitational instabilities. The MCs contain dense sub-structures called filaments that in turn harbour molecular cloud cores. The cores collapse under the influence of gravity and begin the star formation process. The variation in the mass and size of the cores result in a variety of stars whose masses range from one-tenth to about 100 times the mass of the Sun. The stars are powered by the fusion of hydrogen atoms and produce heavier elements in their core during their lifetime. They influence the ISM via their radiation and winds. When the fusion reactions stop, the stars reach the end of their life. The low-mass stars enrich the ISM with the newly produced elements when their gaseous layers are separated from the stellar core. The high-mass stars (>8 solar mass) end their life in violent supernova events in which they inject highly energetic (kinetic energy of $\sim 10^{51}$ erg), metal-rich gas and radiation into the ISM. The gas is returned back to the ISM and the cycle of star formation continues. Thus, the ISM evolves into stars, the stars first affect the thermodynamical and chemical properties of the ISM and later “dissolve" in the same ISM. As a result, the evolution of the ISM becomes highly non-linear.

The chemical composition of the gas influences the thermal balance in the ISM via line emissions from atoms and molecules. Therefore, they determine the thermodynamical properties of the ISM. In addition to the light from stars, light absorption and emission by the chemical species in the ISM trace the physical structure of the gas. The chemical reactions in the ISM is greatly affected by the gas density, temperature, ionization fraction, as well as by the presence (or absence) of the radiation permeating the ISM. In such a dynamic environment, the chemical composition of the ISM is usually not in equilibrium.

It is not possible to carry out laboratory experiments of the large spatial and temporal scales of the ISM; therefore, numerical models are devised to study the non-linear evolution of the ISM under controlled environments. Since the “infinite resolution" of nature is not within the scope of simulations, they reproduce the natural phenomena via approximations. For example, to model the non-equilibrium evolution of the large amount of chemical species in nature, simulations use “simplified" chemistry-networks; out of the thousands of interactions happening in the ISM, such networks follow only selected reactions between selected chemical species. This thesis investigates the constraint set by the evolution of H_2 and CO on the resolution of a simulation, such that for all lower resolutions, the chemical modelling is prone to numerical errors.

For the investigation of the resolution constraint, simulations that resolve both the dynamical and chemical evolution of the gas up to the scale of massive molecular cloud cores are obtained. In this context, the second part of the thesis presents the mechanism of the gas accretion by the cores that form self-consistently from the diffuse ISM.

The thesis is organized as follows. In Chapter 2, the theoretical background of the ISM and its components is introduced. In Chapter 3, the chemical interactions in the ISM, leading to the formation of H_2 and CO molecules, are presented. Chapter 4 presents the physical and chemical processes commonly included in the simulations, and describes how they are implemented in the simulation presented in the thesis. Chapter 5 describes the setups of two numerical models of molecular cloud formation along with the complete list of the performed simulations. Chapter 6 presents some general properties of the molecular clouds formed in the simulations. The test of convergence of H_2 and CO formation in the two numerical models is presented in Chapter 7 and 8. Chapter 9 introduces a theory to describe the resolution requirements for converged H_2 and CO evolution in simulations, which is then used to explain the obtained simulation results. Chapter 10 discusses the aspects of the derived resolution criteria to provide proof of its robustness. Chapter 11 focuses on the formation of massive molecular cloud cores in a chemically and dynamically resolved simulation. The conclusions from this thesis are presented in Chapter 12.

2 | Theory of the Interstellar Medium

In this chapter, the theoretical background of the ISM relevant for the thesis is presented. The ISM contains matter at different thermodynamical and chemical phases. These phases are heated and cooled by chemical reactions and radiative processes happening at microscopic levels. The molecular cloud phase is a turbulent structure in the ISM whose major components are *simple* molecules such as H_2 and CO. The MCs are stellar nurseries that harbour MC cores, which are the earliest signatures of sites of possible star formation.

2.1 | THE COMPOSITION OF THE ISM

The atoms, molecules, and ions constitute the gaseous component of the ISM. Hydrogen accounts for the majority of the mass of the ISM (70%) followed by helium (28%) and the heavier elements (2%). Of the total hydrogen content, 60% of the mass is in atomic form (H), 23% in ionized form (H^+), and 17% in H_2 (Draine 2011). This basic composition is enriched by the elements produced in stars, commonly referred to as metals. The abundance of metals relative to hydrogen (termed metallicity) in the ISM varies greatly both within and outside a galaxy. For example, following the observation of numerous stars and star-clusters, Rolleston et al. (2000) determined that the galactic metallicity gradient for our Milky-Way is about -0.07 dex kpc^{-1} (new estimates from, for example Lemasle et al. (2018), is ~ -0.04 dex kpc^{-1}). Outside a galaxy, the intergalactic medium is relatively much poor in metallicity. The metallic components lead to the formation of molecules, such as CO, in the ISM. Until 2018, about 200 molecules have been detected in the ISM (Cologne Database for Molecular Spectroscopy, CDMS [1]).

The measurement of the starlight-extinction in the ISM shows absorption features over broad frequency ranges, while a widespread continuum emission spectrum is observed in the mid- and far-infrared regimes (eg. Goldreich & Kwan 1974; Draine & Lee 1984). This is attributed to the dust particles in the ISM that are distinct from the atomic, ionized, or the molecular phases. They are solid particles formed from metals, are $\sim 1\mu$m in size, and account for 1% of the mass in the ISM.

Both the gas and dust particles in the ISM interact with the interstellar radiation field (ISRF) and the cosmic rays. The ISRF is composed of the cosmic microwave background (CMB) emission, the black-body emission from stars, the dust emission, X-ray emission from hot plasma, and synchrotron emission from relativistic electrons. The ISFR induces many heating and cooling processes in the ISM and therefore, alters the thermo-chemical property of the gas. The cosmic rays are high-energy (up to 1 TeV), relativistic ions and electrons, that are mainly guided around in the ISM by the magnetic field lines. These mechanisms, together with turbulence and gravity, create a dynamic ISM environment.

---

[1] `https://cdms.ph1.uni-koeln.de/cdms/portal/home`

2.2 | PHASES OF THE ISM

On the basis of the thermal and chemical state of the gas, the ISM can be distinguished into various phase structures. Assuming thermal equilibrium in the atomic component of the ISM, Field et al. (1969) put forward the model with two phases that can coexist at a given range of pressures. The high temperature phase at $T \sim 10^4$ K (now known as the Warm Neutral Medium, WNM) and the low temperature phase at $T \sim 100$ K (now known as the Cold Neutral Medium, CNM) are the two stable phases. The thermally unstable atomic gas at intermediate temperature will either heat up to become the WNM phase or cool down to become the CNM phase. Later, McKee & Ostriker (1977) introduced a third phase of the ISM: the hot and ionized gas at $T \sim 10^6$ K originating in the supernova explosions (now known as the Hot Ionized medium, HIM). In addition, the ionized phase of the gas with density and temperature comparable to the WNM has also been observed (e.g Reynolds et al. 1973); this phase is commonly known as the Warm Ionized Medium (WIM). Finally, the well-known molecular phase of the gas in the ISM, usually enclosed by the diffuse WNM and the CNM, is the Molecular Cloud (MC) itself.

Together, these five phases existing at various spatial scales define the gaseous composition of the ISM. However, a significant fraction of the atomic ISM also exists in the thermally unstable regime, with typical temperatures between that of the WNM and CNM. This can be attributed to the fact that the ISM is not usually in thermal equilibrium and the ISM turbulence is responsible for mixing the various phases of the ISM.

2.2.1 | HEATING AND COOLING IN THE ISM

The heating and cooling mechanisms present in the different ISM phases determine their typical temperature. Such mechanisms are quite different in the atomic and/or ionized medium, and in the molecular medium. The density of the gas, the chemical composition, and the strength of the ISRF experienced by the gas are some of the essential factors influencing the heating and cooling processes.

PROMINENT HEATING MECHANISMS

Photoelectric heating: The electrons ejected from dust by the ISRF heat the gas by colliding with the surrounding atoms or molecules (Bakes & Tielens 1994; Wolfire et al. 2003).

Photo-dissociation of H_2: Dissociation of H_2 molecules due to the line absorption of ultraviolet photons and the cosmic ray ionization of H_2 deposit ~ 0.4 eV energy into the gas (Black & Dalgarno 1977).

Collision with Galactic Cosmic Rays (GCRs): The cosmic rays can penetrate deep into the molecular clouds and this ionization heating can balance the gas cooling (e.g. by CO, atomic C, O_2, and H_2O) in the dense regions to maintain the temperature at ~ 10 K (Goldsmith & Langer 1978).

H_2 formation on dust grains: The binding energy of 4.48 eV is released when H_2 forms on dust grains. This energy is either stored as the internal energy of the excited H_2 molecule, or transferred to other H_2 molecules via collisions. This leads to significant heating in places of rapid H_2 formation (Goldsmith & Langer 1978).

UV pumping of H_2 molecules: The Far-UV pumping of H_2 molecules in the surface of molecular clouds heat the dense clouds (Burton et al. 1990).

Dynamical heating: At high densities where the ISRF is mostly shielded, heating via adiabatic compression of the gas, or localized heating by turbulent dissipation at shocks also become effective.

PROMINENT COOLING MECHANISMS

Lyman-α cooling: At temperatures close to $\sim 10^4$ K, the excitation of atomic H leads to the ultraviolet emission lines of the H atom called the Lyman series.

Atomic cooling from metals: At temperatures $T \gtrsim 10^4$ K, the line cooling from C, O, Ne, and Fe become more effective than the Lyman-α cooling because the abundance of atomic H goes down (Gnat & Ferland 2012). The fine structure lines of C^+ ion in the diffuse ISM (WNM and CNM), the neutral O atom in the WNM, and the neutral C atom at fairly high densities (n up to around 100 cm^{-3}), are the important coolants that collectively cool the gas below 20 K (Wolfire et al. 1995; Klessen & Glover 2016).

H_2 cooling: H_2 is the most abundant molecular species in the ISM. The energy required to excite the rotational transition in a H_2 molecule is quite high and for this reason, H_2 cooling is effective only at temperatures $T > 100$ K. Furthermore, such rotational transitions are excited mostly via collision with other H_2 molecules, while collision with H atoms are less effective (Glover & Abel 2008). Usually, this combination of high temperature, high H_2 density gas is difficult to obtain in the quiescent ISM. Instead, the H_2 cooling is dominant mostly in the shocked regions of the ISM (Hollenbach & McKee 1979). While deuterated H_2 is more effective at cooling the gas with $T < 100$ K, this cooling is still negligible compared to the cooling by C^+, C, CO, and dust.

CO cooling: CO is the second most abundant molecular species in the ISM. The cooling via CO line emissions becomes effective in the dense gas with $T < 20$ K. However, due to the restrictions by the critical density at which the CO rotational levels reach local thermal equilibrium (LTE) and by the relatively high optical thickness of such rotational transitions, the CO cooling becomes comparable to the atomic C cooling over a narrow range of densities (10^3 $cm^{-3} \lesssim n \lesssim 10^4$ cm^{-3}) in the cold gas (Klessen & Glover 2016).

Dust cooling: When the density of H_2 molecules is higher than $\sim 10^4$ cm^{-3}, the cooling due to dust-gas collisions and the subsequent infrared emission by dust grains is known to be significant (Goldsmith & Langer 1978). In addition, the cooling of the gas via electron recombination dominates over the photoelectric heating for $T > 10^4$ K. As a result, the upper limit temperature of the WNM is maintained at $\sim 10^4$ K (Bakes & Tielens 1994).

NET HEATING AND COOLING

An analytic expression for the net cooling rate in the ISM is given by Koyama & Inutsuka (2002) and Vázquez-Semadeni et al. (2007) as

$$n\Lambda - \Gamma = \Gamma \left(\frac{n\Lambda}{\Gamma} - 1 \right) , \tag{2.1}$$

where n is the gas number density, $n\Lambda$ is the cooling rate, and Γ is the heating rate. The factor

$$\frac{n\Lambda}{\Gamma} = n \left[10^7 \exp \left(\frac{-1.184 \times 10^5}{T + 1000} \right) + 1.4 \times 10^{-2} \sqrt{T} \exp \left(\frac{-92}{T} \right) \right] \tag{2.2}$$

is dimensionless and $\Gamma = 2 \times 10^{-26}$ erg s^{-1}.

The **cooling time-scale** determines the time for gas to reach thermal equilibrium (i.e. $n\Lambda - \Gamma = 0$) in the ISM. The net cooling time is given by

$$\tau_{\text{cool}} = \frac{u}{n\Lambda - \Gamma} , \tag{2.3}$$

where u is the average internal energy density. If the cooling time is longer than the sound crossing time or the time interval between shocks, the gas is not in thermal equilibrium.

In typical CNM and MC conditions, τ_{cool} is found to be shorter than the turbulent transport time-scale (Scalo & Elmegreen 2004) or gravitational free-fall time-scale (Goldsmith & Langer 1978). One of the important instabilities occurring in the ISM is the thermal instability (also known as the cooling instability). The cooling gas becomes unstable to the thermal condensation and leads to rapidly growing non-linear density perturbations on the time-scale τ_{cool} (Field 1965). Therefore, the thermal instability has been attributed to generating substructure in the cooling ISM (Burkert & Lin 2000). Shock waves traveling through the ISM can easily initiate thermal instability to form cold and dense gas from the warm atomic gas.

For any given length-scale of a system, the **sound crossing time** is dictated by the local sound speed,

$$c_{\text{s}} = \sqrt{\frac{\gamma P}{\rho}} = \sqrt{\frac{\gamma k_{\text{B}} T}{\mu\, m_{\text{p}}}} , \tag{2.4}$$

where γ is the adiabatic index of the gas, P is the gas thermal pressure, and ρ is the mass density. For ideal gas, the second expression can be used, where k_B is the Boltzmann constant, T is the temperature of the gas in thermal equilibrium, μ is the mean molecular weight of the gas, and m_{p} is the proton mass. Under isothermal conditions, $\gamma = 1$, so that the sound speed is related only to the gas temperature and density.

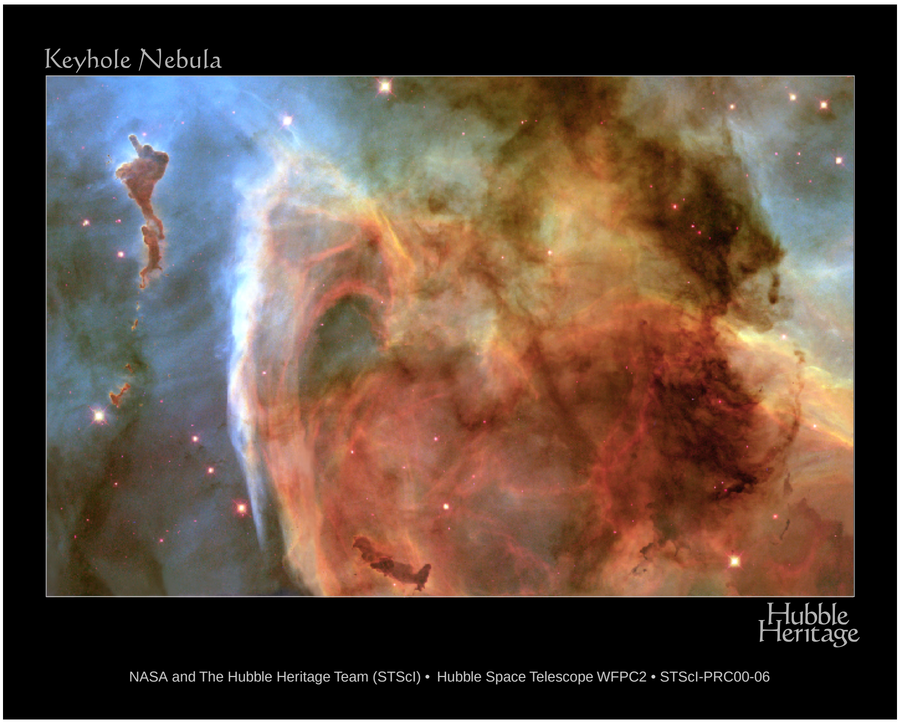
Keyhole Nebula
Hubble Heritage
NASA and The Hubble Heritage Team (STScI) • Hubble Space Telescope WFPC2 • STScI-PRC00-06

Figure 1: Hubble image of a part of the Carina Nebula, showing a rich sub-structure in the roughly circular feature of the Keyhole Nebula. The bright gaseous structures on the left and right edges of the cloud are fluorescing gas, heated by radiation from stars outside the field of view in the image. The extended dark features are turbulent molecular clouds containing cold gas and dust. The distinct features on the top left and bottom center are well-defined clouds that are probable sites of star formation. Image credits: NASA, The Hubble Heritage Team (AURA/STScI)

2.3 | MOLECULAR CLOUDS (MCS)

Molecular clouds are the dense and cold regions, rich in H_2 and CO molecules. The low density WNM and CNM occupy a large volume, but contain a small fraction of the mass in the ISM. On the other hand, the MCs occupy only 1–2% of the volume of the ISM, and account for about 20% of the mass in the ISM (Draine 2011).

Some decades ago, MCs were viewed as quasi-static entities with a relatively long life-time that slowly form stars (Zuckerman & Evans 1974). An early model of MC formation was introduced by Oort (1954). He proposed that the acceleration of cold masses of gas from the outskirts of ionizing stars collide with other such cold clouds to eventually form MCs. Such a cloud collision model can explain properties such as the cloud mass function, or the greater abundance of MCs in galactic spiral arms. However, it predicts the formation of MCs as isolated entities in the ISM, that form over a long time-scale. Following the numerous observations of molecular clouds, starting with Larson (1981), it is now well established that the ISM, and especially MCs, are turbulent in nature; they exhibit a self-similar behaviour over a large range of mass and size and are located well within the atomic phases (WNM and CNM) of the ISM (e.g. Williams et al. 2000; Arzoumanian et al. 2011; Motte et al. 2014). The power-law relation between the three dimensional velocity dispersion (σ) and the size (L) of a MC, describing the hierarchy of turbulent motions in MCs, was first presented by Larson (1981) as

$$\sigma \approx 1.10 \left(\frac{L}{1\,\mathrm{pc}}\right)^{\gamma}, \tag{2.5}$$

with the power-law exponent $\gamma = 0.38$ for $0.1\,\mathrm{pc} < L < 100\,\mathrm{pc}$. While the value of the exponent is a topic of debate (e.g. Solomon et al. 1987; Heyer & Brunt 2004), the power-law nature is now firmly established as the defining characteristic of a MC.

Two key time-scales determine the lifetime of turbulent MCs, namely the turbulent dissipation time and gravitational free-fall time. The rate of decay of the turbulent kinetic energy determines the **turbulent dissipation time-scale** ($\tau_{\mathrm{turb,dissip}}$). The dissipation time is found to be comparable to the turbulent crossing time (Mac Low et al. 1998) that depends on the size of the system at which turbulent energy is being injected and the velocity dispersion at that length-scale. Therefore, for the L and σ of a MC,

$$\tau_{\mathrm{turb,dissip}} = \frac{e}{\dot{e}} \sim \frac{L}{\sigma}, \tag{2.6}$$

where e denotes the turbulent kinetic energy density and $\dot{e}$ is it's decay rate.

The **gravitational free-fall time** is the characteristic time in which any given mass density distribution will collapse under gravity, if other competing forces are absent. For a uniform density distribution, it is given by (Spitzer 1978)

$$t_{\mathrm{ff}} = \sqrt{\frac{3\pi}{32G\rho}} \approx 1.4 \times 10^{6}\,\mathrm{yr} \left(\frac{n}{10^{3}\,\mathrm{cm}^{-3}}\right)^{-1/2}. \tag{2.7}$$

where G is the gravitational constant. Note that t_{ff} does not depend on the mass of the collapsing system, but only depends inversely on the initial mass density ρ.

Velocity dispersions in the range $1 - 10\,\mathrm{km\,s^{-1}}$ have been observed for typical MCs of size up to ~ 20 pc (Roman-Duval et al. 2010). Mac Low et al. (1998) and Stone et al. (1998) noted that the energy dissipation time-scale in supersonic turbulence observed in MC conditions is comparable to the typical free-fall gravitational collapse time. However, the MCs themselves are a few free-fall times old ($\tau_{\mathrm{MC,life}} \sim 3 \times 10^{7}$ yr); thus, energy has to be continuously injected into the MCs for them to retain their turbulent nature and provide support against the gravitational collapse (Mac Low et al. 1998; Mac Low & Klessen 2004). At present, MCs are considered to be dynamical objects dominated by turbulence that quickly form stars or stellar-clusters (Padoan et al. 1999; Ballesteros-Paredes et al. 1999; Elmegreen & Scalo 2004; Mac Low & Klessen 2004; Heitsch et al. 2006; Vázquez-Semadeni et al. 2007; Motte et al. 2014, to name a few). The lifetime of MCs end with the formation of stars; thus, MCs are now believed to be transient features in the ISM.

2.4 | MOLECULAR CLOUD CORES

The molecular cloud cores are the smallest of the MC structures observed in the ISM. They are dense objects in the interior of MCs, created due to the fragmentation of the cloud. A considerable fraction of the observed MC cores are starless clumps with masses ranging from 0.3 to 3 $M_\odot$ (Motte et al. 1998; Lada et al. 2008). Cores with mass $> 3\ M_\odot$ are generally gravitationally bound.

Cores that are formed from the fragmentation of the dense structures into multiple small-scale gravitating clumps usually lead to the formation of low-mass stars. On the other hand, cores formed from large-scale collapse of the parent molecular cloud such as Infrared Dark Clouds (IRDCs) pave way for the formation of extremely massive cores that are potential nurseries for a cluster of high-mass stars (e.g. Smith et al. 2011; Peretto et al. 2013). Both low-mass and massive cores are often observed in filamentary structures (e.g. Arzoumanian et al. 2019) that are linked together at a hub (the so called hub-filament structure, Myers 2009). In such an arrangement, low-density (and low-mass) cores are formed in the filaments themselves, and massive cores form at or near the hubs. As a result, a variety of molecular cloud cores are often observed to form in chains (Motte et al. 1998; Lada et al. 2008; Peretto et al. 2013).

In the dense cores, a variety of complex molecules are found. The molecules are not easily destroyed as in the outer regions; most of them are inferred to freeze-out on the surface of dust grains (Bergin & Tafalla 2007). The gas temperature in molecular cloud cores are determined via the line excitation of molecules such as ^{12}CO, ^{13}CO, NH_3, CH_3OH, HCO^+, etc. (Walmsley & Ungerechts 1983; Peretto et al. 2013) in the far-infrared regime. The radial temperature profile of observed cores show a temperature gradient from 8 K to 20 K, with isothermal conditions in the cold, inner regions of the core (Ward-Thompson et al. 2002). The thermal balance between the cosmic ray ionization heating, compressional heating, turbulence dissipation, CO line emissions, and gas-grain energy transfer regulate the temperature of the molecular cloud cores.

Observations by Campbell et al. (2016) conclude that only a small fraction of the starless cores show signs of inflow. On the other hand, Peretto et al. (2013) note the relatively large accretion velocities near massive cores. The details of gas accretion onto the cores is difficult to determine, because the low infall velocity into the cores can be easily obfuscated by, for example, core rotation (and outflow mechanisms, in case protostellar objects are present).

3 | The chemical evolution in molecular clouds

This chapter presents a short overview of the chemical interactions happening in the ISM, that lead to the formation of H_2 and CO molecules in the MCs. The interaction of the gas and dust with the ISRF in the turbulent ISM leads to a non-equilibrium chemical evolution. The ISM is heated or cooled by various processes presented in Section 2.2.1 of the previous chapter. At the same time, a vast number of gas-phase and grain-surface chemical reactions occur in the ISM. The evolution of MCs from the diffuse ISM is predominantly characterized by the chemical evolution of H_2 and CO. The formation of these molecules are preceded by numerous reactions in the diffuse ISM. They in turn facilitate the formation of complex molecules in the dense MC cores.

3.1 | IMPORTANCE OF H_2 AND CO

Two major chemical transitions occur during the evolution of MCs from the diffuse ISM. The diffuse cloud becomes molecular when most of the hydrogen in the evolving cloud is found in the form of H_2. After the shielding of the ISRF by H_2 molecules becomes effective, CO formation is accelerated. The MC is not observable during the transition from atomic WNM to H_2 molecules. The homo-nuclear H_2 molecule does not have a permanent dipole moment and does not emit any radiation at the typical temperature ($T \lesssim 50$ K) found in the MCs at this stage. On the other hand, the formation of CO is comparatively easy to observe, thanks to the CO emission from the dense regions of the MC. The formation mechanism of H_2 molecules from the interaction between the existing atoms, ions, and radiation is not so trivial. The evolution of CO is even more complicated due to multiple reaction paths creating and dissociating the CO molecule simultaneously. Nevertheless, the evolutionary track of these molecules in the ISM have been thoroughly investigated because they are the major constituents of any molecular cloud.

Glover et al. (2010) have demonstrated that the distribution of H_2 has a good correlation with the gas density distribution in MCs. The abundance of CO, on the other hand, does not have a straightforward relation with either the visual extinction (A_V) or the gas density (n), even though both of these are the most essential factors affecting the CO chemistry. This poor correlation is attributed to the fact that the turbulence in the ISM disrupts the trivial correlation between A_V and gas density. H_2 can exist at $A_V > 0.2$, thanks to its self-shielding behaviour (Wolfire et al. 2010) on top of the shielding of the interstellar radiation field (ISRF) by the dust. For

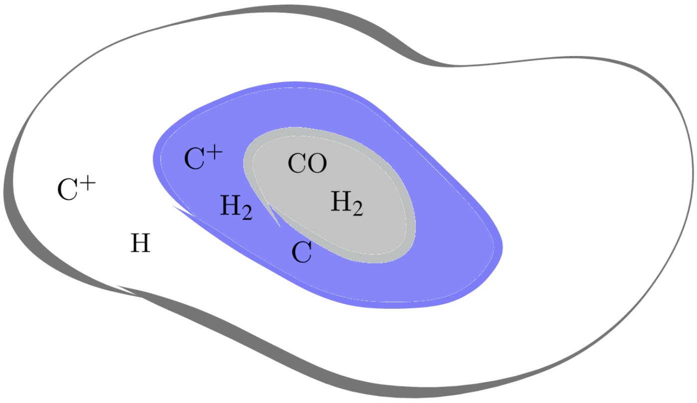

Figure 2: A simple model of a cloud showing the different layers that are mostly atomic (outer, white), partially molecular (CO-dark molecular gas, central, blue), and mostly molecular (CO-bright molecular gas, innermost, grey).

Table 1: Generic gas phase reactions for representative chemical species (A, B, C, D) and electrons (e).

SN	Reaction	Reaction type
1	$AB + \text{photon} \longrightarrow A + B$	Photo-dissociation
2	$A + B \longrightarrow C + D$	Neutral-Neutral
3	$A^+ + B \longrightarrow C^+ + D$	Ion-Molecule
4	$A^+ + B \longrightarrow A + B^+$	Charge exchange
5	$A + B \longrightarrow AB + \text{photon}$	Radiative association
6	$A^+ + e \longrightarrow C + D$	Dissociative recombination
7	$A^- + B \longrightarrow AB + e$	Associative detachment
8	$AB + C \longrightarrow A + B + C$	Collisional dissociation

$A_V < 3$, photo-dissociation takes its toll on the existence of CO and the abundance of CO in molecular clouds decreases drastically with decreasing A_V (Glover & Mac Low 2011). Thus, CO is generally found to sustain in environments with $A_V \gtrsim 3$. This leads to the existence of the so called CO-dark and CO-bright regions of MCs. In Figure 2, the schematic representation of the gas in MCs shows the simplified arrangement of the atomic, CO-dark, and CO-bright components of the ISM near MCs. The inner regions of MCs, where H_2 and CO are not readily destroyed, then become nurturing grounds for more complex molecules.

GAS-PHASE CHEMICAL REACTIONS

The chemical evolution in the ISM is mostly dictated by gas phase chemical reactions. The formation of CO via multiple reaction paths is a well-known example of such reactions. Some generic examples of the typical gas phase chemical reactions occurring in the various phases of the ISM are given in Table 1

GRAIN-ASSISTED CHEMICAL REACTIONS

The most important mechanism for the formation of H_2 molecules in the ISM is the association of atomic H on the surface of dust grains (Gould & Salpeter 1963). For the grain surface chemistry, factors such as the accretion rate of reacting species onto the grain and the migration rate of such accreted species on the surface of the grain come into play. Therefore, the thermal velocity of the gas, the size of the grain, and the number density of grains become important physical properties governing the chemical evolution on the grain surfaces (Hollenbach & McKee 1979).

3.2 | H_2 FORMATION AND DESTRUCTION

As mentioned above, the formation of H_2 is known to occur mostly by the grain-assisted association of two H atoms. Following Hollenbach et al. (1971), the factors affecting the H_2 formation is briefly described here.

The rate of H_2 formation on the dust grain surface is given by the expression

$$R_G = \frac{1}{2}\gamma\langle v_{\rm H}\rangle n_{\rm H} n_{\rm g}\langle\sigma_{\rm g}\rangle\,, \tag{3.1}$$

where γ refers to the recombination coefficient (fraction of the H atoms incident on the grain surface that eventually form H_2 molecules), $\langle v_{\rm H}\rangle$ is the average thermal velocity of H atoms, $n_{\rm H}$ is the number density of H atoms, $n_{\rm g}$ is the number density of dust grains, and $\langle\sigma_{\rm g}\rangle$ is the average geometric cross section of the dust grains. Although γ and $\langle v_{\rm H}\rangle$ both depend on the gas temperature, the expression $\gamma\langle v_{\rm H}\rangle$ has a weak dependence on the temperature and can be approximated as $\gamma\langle v_{\rm H}\rangle = 5\times 10^4$ cm s^{-1}. Another underlying assumption here is that every H atom that sticks to the grain (given by the so called sticking coefficient) will eventually form H_2 on the grain. For the typical HI cloud conditions in which H_2 form, this approximation is quite robust at gas temperatures between 4 K and 200 K. The constant dust-to-gas mass ratio of 0.01 helps to approximate $n_{\rm g}$ in terms of the gas density n. Finally, the average grain cross sectional area can be calculated from typical 0.2μ radius of dust grains. A rate coefficient can incorporate all these factors to give the H_2 formation rate as

$$R_G = k_{\rm H_2,g}\, n_{\rm H}\, n\,, \tag{3.2}$$

where the formation rate coefficient

$$k_{\rm H_2,g} \in [10^{-17}, 3\times 10^{-17}]\ {\rm cm^3\ s^{-1}} \tag{3.3}$$

is generally accepted for the assumptions made above (Jura 1975). However, since H_2 formation lays the foundation for the evolution of molecules in the ISM, a slightly general formulation of $k_{\rm H_2,g}$ is used in numerical modelling. For example, Glover et al. (2010) implement the rate coefficient

$$k_{\rm H_2,g} = 3\times 10^{-18}\sqrt{T}\, f_{\rm A}\, f_{\rm stick}\ {\rm cm^3\ s^{-1}}\,, \tag{3.4}$$

where T is the gas temperature in units of Kelvin, $f_{\rm A}$ is the fraction of H atoms that convert into H_2 in dust grains (the classical recombination coefficient γ as given in Hollenbach et al. (1971), but renamed here to avoid confusion with the adiabatic index of gas or, in case of chemical reactions, the notation for a photon) and is given by

$$f_{\rm A} = \left[1 + 10^4 \exp\left(\frac{-600}{T_{\rm d}}\right)\right]^{-1}\,, \tag{3.5}$$

and $f_{\rm stick}$ is the sticking coefficient given by

$$f_{\rm stick} = \frac{1}{1 + 0.04\sqrt{T + T_{\rm d}} + 0.002\,T + 8 \times 10^{-6}\,T^2}\,, \tag{3.6}$$

with the dust temperature $T_{\rm d}$ also in units of Kelvin.

Gould & Salpeter (1963) noted that all other formation processes of H_2 are much slower. In atomic medium with magnitude of visual extinction larger than 5 and high electron density, other formation processes (e.g. via H^- radical) can be taken into account, besides the grain-assisted formation. Nevertheless, formation rate of these other mechanisms are orders of magnitude smaller than the formation rate on dust grains.

The H_2 molecules are usually embedded in CNM rich in atomic H. Collisional dissociation of H_2 molecules is possible only in warm and dense regions, that are atypical in the ISM. The binding energy of the H_2 molecule is 4.48 eV; however, only high energy photons (14.7 eV) can dissociate the H_2 molecules directly. Since such energetic photons do not reach the typical regions of H_2 formation near molecular clouds, H_2 dissociation occurs mostly via the two-stage process discussed by Stecher & Williams (1967). First, the H_2 molecule is excited to vibrational states via the absorption of UV photons. Then, the H_2 molecule can undergo a radiative decay either to the vibrational continuum and subsequently dissociate or to the ro-vibrational level and survive the excitation. Draine & Bertoldi (1996) noted that the probability of dissociation in this manner is about 15% on average. In addition, cosmic rays can also dissociate the H_2 molecules, although this rate is about 5 orders of magnitude smaller than the UV dissociation rate (e.g. Hollenbach et al. 1971).

H_2 FORMATION TIME-SCALE

From the rate coefficient in Equation 3.3, the resulting **steady state H_2 formation time-scale** is given by (Hollenbach et al. 1971; Hollenbach & McKee 1989; Goldsmith & Li 2005)

$$\tau_{{\rm H_2,eq}} = \frac{n_{\rm H}}{R_G} \sim 10^3\ {\rm Myr} \left(\frac{\bar{n}}{1\ {\rm cm}^{-3}}\right)^{-1}\,, \tag{3.7}$$

where $\bar{n}$ is the mean gas number density in the region of interest. With the rate coefficient in Equation 3.4, a more **general H_2 formation time-scale** is obtained for individual fluid element as

$$\tau_{{\rm H_2,form}} = \frac{1}{3 \times 10^{-18}\,\sqrt{T}\,f_{\rm A}\,f_{\rm stick}}\,\frac{1}{n}\ {\rm seconds}\,. \tag{3.8}$$

3.3 | CO FORMATION AND DESTRUCTION

The formation CO in MCs is complicated as there is no single dominant formation mechanism as for H_2. Multiple reaction paths via either oxygen-bearing species or carbon-bearing species determine the CO formation (see e.g. Glover & Clark 2012; Klessen & Glover 2016). Of the many oxygen-bearing species, the formation of OH^+ is the most important reaction step. Once OH^+ is formed, OH forms rapidly and then the formation CO follows immediately via reactions such as

$$C + OH \longrightarrow CO + H\,, \tag{3.9}$$
$$C^+ + OH \longrightarrow CO^+ + H\,, \tag{3.10}$$
$$CO^+ + H \longrightarrow CO + H^+\,, \tag{3.11}$$
$$CO^+ + H_2 \longrightarrow HCO^+ + H\,, \tag{3.12}$$
$$HCO^+ + e^- \longrightarrow CO + H\,. \tag{3.13}$$

In the cold gas of the CNM or molecular clouds, OH^+ is formed via two main paths for which H_2 and H_3^+ are required:

$$O + H_3^+ \longrightarrow OH^+ + H_2\,, \tag{3.14}$$
$$O^+ + H_2 \longrightarrow OH^+ + H\,. \tag{3.15}$$

On the other hand, the CO formation via hydrocarbon pathway is initiated by the formation of CH_2^+ ions (Tielens & Hollenbach 1985)

$$C^+ + H_2 \longrightarrow CH_2^+ + \gamma\,, \tag{3.16}$$
$$C + H_3^+ \longrightarrow CH_2^+ + H\,, \tag{3.17}$$

The CH_2^+ ions quickly form species like CH and CH_2, which react with atomic O to produce CO as

$$CH + O \longrightarrow CO + H\,, \tag{3.18}$$
$$CH_2 + O \longrightarrow CO + H_2\,, \tag{3.19}$$
$$CH_2 + O \longrightarrow CO + H + H\,. \tag{3.20}$$

Furthermore, in regions with high abundance of neutral atomic carbon, the C atoms directly form CH and CH_2 as

$$C + H \longrightarrow CH + \gamma\,, \tag{3.21}$$
$$C + H_2 \longrightarrow CH_2 + \gamma\,. \tag{3.22}$$

Finally, the H_3^+ radical, that is involved in both the CO formation pathways, forms quickly once H_2^+ is formed via cosmic ray ionization as

$$H_2 + \text{cosmic-ray} \longrightarrow H_2^+ + e^-\,. \tag{3.23}$$

The H_3^+ radical readily dissociates to excited H_2, which will produce UV photons upon de-excitation that can dissociate CO molecules

$$H_3^+ + e^- \longrightarrow H_2 + H\,. \tag{3.24}$$

Thus, reactions 3.16, 3.17, 3.23, 3.24, as well as the formation of H_2 are treated as the limiting reactions for CO formation.

Photo-dissociation is again the most important destruction mechanism of CO. If the visual extinction is not sufficiently high, UV photons with energy $E > 11.09$ eV excite the CO molecules, that then undergo radiative decay. Unlike H_2, CO is mostly dissociated during this process (van Dishoeck & Black 1988). Compared to H_2, the CO molecules absorb a broader spectrum of UV photons, leading to a less effective self-shielding behaviour of CO (Klessen & Glover 2016). In regions where the ISRF is highly shielded, CO is destroyed either by cosmic ray induced photons (emitted from excited H_2 molecules) or by reaction with He^+ that are produced by cosmic ray ionization of He atoms.

The shielding of the ISRF by H_2 molecules is important for CO to sustain in the dense regions of the ISM. As noted above, the H_2 molecule is actively involved in intricate chemical reactions for CO formation and destruction. Note that H_3^+ is obtained via the cosmic ray ionization of H_2. Thus, the abundance of CO is sensitive to the abundance of H_2.

CO FORMATION TIME-SCALE

The formation rate of CH_2^+ via reaction 3.16 is

$$R_{CH_2^+,1} = k_{CH_2^+,1} n_{C^+} n_{H_2} , \tag{3.25}$$

where $k_{CH_2^+,1}$ denotes the rate coefficient for reaction 3.16 and n_x denotes the number density of the chemical species x.

The formation rate of CH_2^+ via the H_3^+ pathway (reaction 3.17) can be combined with the rate of H_3^+ formation/destruction (reactions 3.23, 3.24) to obtain the net formation rate (see Glover & Clark 2012, for further details)

$$R_{CH_2^+,2} = 2\,\zeta_H\, n_{H_2} \frac{k_{CH_2^+,2}}{k_{dr}} \frac{n_C}{n_{e^-}} . \tag{3.26}$$

Here, ζ_H is the cosmic ray ionization rate of atomic hydrogen, $k_{CH_2^+,2}$ denotes the rate coefficient for reaction 3.17, and k_{dr} denotes the rate coefficient for the dissociative recombination reaction 3.24.

Thus, analogous to the H_2 formation time-scale, the **net CO formation time-scale** is then given by

$$\tau_{CO,form} = \tau_{H_2,form} + \frac{n_C^+}{R_{CH_2^+,1}} + \frac{n_C}{R_{CH_2^+,2}} . \tag{3.27}$$

Here, $\tau_{H_2,form}$ enters the CO formation time-scale because H_2 formation is also a limiting reaction for CO chemistry. Naturally, the expression for CO formation time-scale is vastly more complicated than that for the H_2 formation time-scale. A simple density dependent formation time (like Equation 3.7 for H_2) cannot be obtained for CO, since multiple local, non-linear mechanisms dominate the CO evolution.

3.4 | THE EFFECT OF TURBULENCE ON THE MC CHEMISTRY

The turbulence in the MCs brings fundamental changes in the dynamical and chemical properties of the compressible, gravitating, and magnetic gas. It is relevant for the chemistry in MCs because the turbulent timescales (Equation 2.6) are quite-often smaller than the typical chemical time-scales (i.e. formation, dissociation, or equilibrium time-scales for molecule formation). The turbulent medium is long known to prevent the chemistry in the MCs from reaching a equilibrium state (Phillips & Huggins 1981).

In general, turbulence is able to affect the chemical evolution in the ISM by continuously transporting the gas into regions with varying physical/thermodynamical conditions and by introducing shock heating into the chemical reactions happening in the gas; it also redistributes the ionized species, thereby affecting the ion-neutral reactions (Scalo & Elmegreen 2004). Density enhancements at the shocks become nurturing grounds for molecule formation (Hollenbach & McKee 1979) and such intermittent regions can lead to a “faster-than-average" H_2 formation (Glover & Mac Low 2007b; Micic et al. 2012; Valdivia et al. 2016; Seifried et al. 2017). Near the shocks, the triggered chemical reactions and radiative absorption/emission change the energetics of the system. At the site of molecule formation, the cooling time-scales are usually shorter than the typical dynamical time-scales, leading to near isothermal conditions (Scalo & Elmegreen 2004). As a result, the compression factor at the shock front can be much larger than in the adiabatic case. Therefore, the interaction between the chemistry and turbulence in the ISM is highly nonlinear.

4 | Simulation of molecular cloud formation

This chapter gives a description of physical and chemical processes that are generally incorporated in simulations and how the evolution of MC in nature have been modelled in numerical studies. The components of the software/code used to include these processes in the simulations presented in the thesis are described. A particular focus is given to the modelling of chemical interactions in the ISM and MC via chemical-networks that are now growing in complexity with increasing computational power. The capacity of the simulations to resolve various spatial and temporal scales determines what kind of results can be drawn confidently from them. At the end of the chapter, a representative list of simulations that have been performed over the last decade to investigate the formation of MC is provided.

4.1 | MAGNETO-HYDRODYNAMICS (MHD)

A real gas begins to behave like ideal gas if its density is low and temperature is high. If the mean-free path between the gas particles is orders of magnitude shorter than the scale at which the flow of the gas is studied, and the gas is in local thermal equilibrium, it can be described as a fluid. The phases of the ISM satisfy these criteria and can be treated as a fluid. An element of the fluid represents the average thermodynamical properties of an ensemble of gas particles.

A fluid element in the ISM can be described by four independent variables: the mass density ρ, the momentum density $\rho\mathbf{v}$ corresponding to velocity $\mathbf{v}$, the total energy density E, and the magnetic flux density $\mathbf{B}$. The conservation of of these densities govern the motion of the gas. In the absence of any external source/sink terms for these gas-properties, the equation of motion are given by the Euler equations. For the ISM, the modified set of Euler equations with additional source terms for self-gravity, turbulent motions, and radiative heating/cooling is

$$\frac{\partial \rho}{\partial t} + \nabla \cdot (\rho \mathbf{v}) = 0\,, \tag{4.1}$$

$$\frac{\partial (\rho \mathbf{v})}{\partial t} + \nabla \cdot \left[\rho \mathbf{v}\mathbf{v}^{\mathrm{T}} + \left(P + \frac{\mathbf{B}^2}{8\pi}\mathbf{I} \right) - \frac{\mathbf{B}\mathbf{B}^{\mathrm{T}}}{4\pi} \right] = \rho(\mathbf{g} + \mathbf{F})\,, \tag{4.2}$$

$$\frac{\partial E}{\partial t} + \nabla \cdot \left[\left(E + \frac{\mathbf{B}^2}{8\pi} + \frac{P}{\rho} \right) \mathbf{v} - \frac{(\mathbf{B} \cdot \mathbf{v})\mathbf{B}}{4\pi} \right] = \rho \mathbf{v} \cdot (\mathbf{g} + \mathbf{F}) + \dot{u}_{\mathrm{chem}}\,, \tag{4.3}$$

$$\frac{\partial \mathbf{B}}{\partial t} - \nabla \times (\mathbf{v} \times \mathbf{B}) = 0\,. \tag{4.4}$$

These equations relate the time evolution of the four density variables in a volume of the fluid element with their flux through the surface of the volume. Here, t is time, P is the thermal pressure, $\mathbf{I}$ is the identity matrix, $\mathbf{g}$ is the acceleration due to self-gravity, $\mathbf{F}$ is the random acceleration introduced in the gas by turbulence, and $\dot{u}_{\mathrm{chem}}$ is the net rate of change of internal energy of the gas due to the heating from the attenuated uniform background interstellar radiation field (ISRF), radiative cooling, and chemical reactions.

The thermal pressure of the fluid given by

$$P = (\gamma - 1)u\,, \tag{4.5}$$

where u is the internal energy density, γ is the adiabatic index of the ideal gas. The total energy density of the fluid is

$$E = u + \frac{\rho \mathbf{v}^2}{2} + \frac{\mathbf{B}^2}{8\pi}\,, \tag{4.6}$$

where the second and the third terms denote the ram pressure and magnetic pressure, respectively. For the hydrodynamical simulations considered in this thesis, the effects of magnetic field are not included. Therefore, $\mathbf{B} = 0$ and the divergence-free criterion $\nabla \cdot \mathbf{B} = 0$ is trivial in this context.

THE FLASH CODE

The code used to perform the simulations described in this thesis is the versatile FLASH[1] (Fryxell et al. 2000; Dubey et al. 2008) code. It is a publicly available code, designed to model various physical processes, and is commonly used in the astrophysical community for three-dimensional (3D) MHD simulations. It solves the MHD equations on an Eulerian grid; the computational domain is discretized into finite volume sub-domains called blocks. The blocks are the primary computational entities that in turn contain multiple computational cells (8^3 by default, but this can be customized as required). The various physical phenomena are organized as simulation units (or modules) that can access the block structure of the grid. For example, an independently developed CHEMISTRY unit can be used to include the chemical and thermal evolution in a numerical study. The various physical processes included as separate units in the FLASH version 4.3 are briefly introduced in the following sections.

The HYDRO unit of FLASH is used to solve the modified Euler equations for compressible gas dynamics in 3D. A directionally split, finite-difference scheme based on the Bouchut MHD solver HLL5R (Waagan et al. 2011) is used to model the non-linear flow of gas between the computational cells. At each of the six boundaries of every cell, the flux of various quantities between two cells is calculated by solving a Riemann problem. The Riemann problem is solved in three rounds, since the flux along each dimension is determined one after another (MUSCL scheme as presented by van Leer 1979).

---

[1] `http://flash.uchicago.edu/site/flashcode/`

4.2 | CHEMISTRY NETWORKS IN SIMULATIONS

Molecular Clouds are turbulent structures, rich in chemical species that are not in equilibrium (see Section 2.3). If the chemical and dynamical evolution of MCs were loosely coupled, they could be conveniently treated separately. For example, the fluid elements in hydrodynamical simulations without chemistry can be associated with equilibrium values of the chemical species via chemical post-processing. However, it has long been known that various chemical species in MCs are not in chemical-equilibrium (e.g. Leung et al. 1984). The overall density structure of the MC is known to significantly affect the chemical composition since it influences the shielding of the ISRF experienced by various regions within the cloud (e.g. Stutzki & Guesten 1990; Safranek-Shrader et al. 2017). In addition, Glover et al. (2010) suggest that the MC composition is dependent on the history of the gas since the dynamical time-scale and the molecule formation time-scale are comparable in MC conditions. Therefore, simulations of MCs should couple the dynamical and chemical evolution to obtain correct approximations of the MC formation in nature. In order to do so, chemistry networks have to be introduced in numerical models that can evaluate the chemical abundances at every hydrodynamical time-step. Since this is a computationally demanding task (e.g. Glover et al. 2010), only simple chemical networks are affordable.

In the early 2000s, Koyama & Inutsuka (2000, 2002) and Bergin et al. (2004) implemented the non-equilibrium chemistry of H_2 and CO in their one- and two-dimensional hydrodynamic simulations. It was important to include CO chemistry (carbon chemistry in general) in the numerical models because CO is the most important tracer of H_2 and C^+, C, and CO are essential coolants in the ISM. With the increase in computational capabilities, chemistry networks with more species and reactions were introduced in 3D MHD simulations (e.g. Glover & Mac Low 2007a,b). Later, Glover et al. (2010) presented a chemistry network with 32 species linked by 218 reactions, which allows for an accurate treatment of H_2 and CO formation in 3D simulations. A simpler, computationally cheaper network, based on Glover & Mac Low (2007a,b) and Nelson & Langer (1997) has been applied in many recent high-resolution (M)HD simulations (e.g. Walch et al. 2011; Micic et al. 2012; Walch et al. 2015; Girichidis et al. 2016; Gatto et al. 2017; Pardi et al. 2017; Peters et al. 2017; Seifried et al. 2017). Similarly, a few works (e.g. Glover & Clark 2012; Clark et al. 2012b; Szűcs et al. 2014) have used a more complex network (termed “NL99") that combines the CO chemistry of Nelson & Langer (1999) with the hydrogen chemistry of Glover & Mac Low (2007a,b). The NL99 network is used in the work presented here. Alternative, simplified networks for H_2 and/or CO formation have also been presented by Keto & Caselli (2008), Valdivia et al. (2016), and Gong et al. (2017). In simulations of star-forming filaments, Seifried & Walch (2016) presented the use of a heavier network containing 287 reactions between 37 chemical species, implemented as part of the KROME package (Grassi et al. 2014). Recently, Mackey et al. (2018) presented simulations with an updated NL99 chemistry network that incorporates updated reaction rates suggested by Gong et al. (2017).

In addition to these chemistry networks coupled to the gas dynamics, (Albertsson et al. 2013) presented a chemical network with several thousands of chemical reactions between about 700 different species to approximate the chemical evolution for a given set of initial conditions. Similarly, Stéphan et al. (2018) studied the chemical evolution of hot molecular cores with photon dominated regions via a chemical network with up to 334 species; the chemical abundances of such a large number of species were calculated by taking the evolution of gas density, temperature, and radiation intensity as input parameters.

The CHEMISTRY unit of FLASH incorporates the **NL99 chemical network**, which combines the hydrogen chemistry taken from Glover & Mac Low (2007a,b) and the CO network from Nelson & Langer (1999). This network was implemented in FLASH by Mackey et al. (2018).

CHEMICAL SPECIES

The network tracks the abundances of 15 chemical species, including free electrons. Of the 15 species, the networks follows the non-equilibrium evolution of 9 species: H_2, H^+, C^+, CH_x, OH_x, CO, HCO^+, He^+, M^+. The abundances of remaining 6 species (atomic H, He, C, O, M, and electrons) are calculated via conservation laws. Here, CH_x refers to intermediate carbon-bearing such as CH, CH_2, and OH_x to oxygen-bearing species OH or OH^+. These species allow for an accurate evolution of CO molecules (see Section 3.3) in the simulation. Similarly, M represents the combined effects of low ionization potential metals such as Na, Mg, Ca, Fe and M^+ denotes ionized metals. This network considers multiple pathways of CO formation via CH_x and OH_x species (e.g. CH, CH_2, OH, H_2O, etc.), and CO destruction via photo-dissociation as well as via reaction with ions such as H_3^+ and He^+ that are very sensitive to the cosmic ray ionization rate (Bisbas et al. 2015) and the X-ray energy density (Mackey et al. 2018). The recent update to the chemistry network by Mackey et al. (2018) to incorporate the detailed X-ray ionization effects is not a part of the chemistry used for this study.

A total of 42 reactions are included in the NL99 chemistry network used in this study. The reactions included in the chemistry network used in the project are listed in Table 2.

HEATING, COOLING, AND ELEMENTAL ABUNDANCES

The various heating and cooling mechanisms in the ISM due to line emissions, chemical reactions, the photoelectric effect on dust grains, UV radiation, X-ray, and cosmic rays via the diffuse ISRF, mentioned in Chapter 2, are taken into account by the chemical network. For the chemical evolution, the simulation domain is immersed in the uniform ISRF with the strength of $G_0 = 1.7$ in units of the Habing field (Habing 1968; Draine 1978). The relative abundances (number of atoms relative to total H nuclei in the gas) of total He, C, O, and M are standard solar abundances: $x_{\mathrm{He}} = 0.1$, $x_{\mathrm{C}} = 1.4 \times 10^{-4}$, $x_{\mathrm{O}} = 3.2 \times 10^{-4}$, and $x_{\mathrm{M}} = 1.0 \times 10^{-7}$ (Sembach et al. 2000). The cosmic ray ionization rate of atomic hydrogen is $\zeta_{\mathrm{H}} = 3 \times 10^{-17}$ s^{-1} and the cosmic ray ionization rate for other chemical species are then scaled as $\zeta_{\mathrm{H}_2} = 2 \times \zeta_{\mathrm{H}}$, $\zeta_{\mathrm{He}} = 1.09 \times \zeta_{\mathrm{H}}$, and $\zeta_{\mathrm{C}} = 3.83 \times \zeta_{\mathrm{H}}$ using the factors from Liszt (2003) based on data from the UMIST[2] database (McElroy et al. 2013).

EVOLUTION OF CHEMICAL SPECIES

The mass density of each chemical species is advected through the fluid just like the gas density. Therefore, the continuity equation for each non-equilibrium chemical

---

[2] `http://www.rate99.co.uk`

Table 2: Chemical reactions to follow the non-equilibrium evolution of 9 (out of 15) species included in the network NL99. Reactions are compiled with help from the list accumulated by Mackey et al. (2018).

SN	Reaction	Reaction type
	H^+	
1	$H + e \longrightarrow H^+ + 2e$	Collisional ionization
2	$H^+ + e \longrightarrow H + \gamma$	Radiative recombination
3	$H^+ + e \longrightarrow H$	Grain-assisted recombination
4	$H_2^+ + H \longrightarrow H_2 + H^+$	Charge exchange
5	$He^+ + H_2 \longrightarrow He + H + H^+$	Dissociative charge exchange
6	$HCO^+ + FUV \longrightarrow CO + H^+$	Photo-dissociation
7	$H + CR \longrightarrow H^+ + e$	Cosmic-ray ionization
8	$H_2 + CR \longrightarrow H^+ + H + e$	Cosmic-ray ionization
9	$H_2 + CR \longrightarrow H_2^+ + e$	Cosmic-ray ionization (Required for Reaction 4)
10	$H + X\text{-ray} \longrightarrow H^+ + e$	Secondary ionization
	H_2	**Reactions 5, 8, 9, and**
11	$H_2 + e \longrightarrow 2H + e$	Collisional dissociation
12	$H_2 + H \longrightarrow 3H$	Collisional dissociation
13	$H_2 + H_2 \longrightarrow H_2 + 2H$	Collisional dissociation
14	$H + H(s) \longrightarrow H_2$	H_2 formation (H(s): H atom adsorbed on dust surface.)
15	$H_3^+ + M \longrightarrow M^+ + H_2 + H$	Dissociative charge exchange
16	$H_3^+ + e \longrightarrow H_2 + H$	Dissociative recombination
17	$H_3^+ + C \longrightarrow CH_x + H_2$	Formation of CH_x species
18	$H_3^+ + O \longrightarrow OH_x + H_2$	Formation of OH_x species
19	$H_3^+ + CO \longrightarrow HCO^+ + H_2$	Proton transfer
20	$He^+ + H_2 \longrightarrow He + H_2^+$	Charge exchange
21	$C^+ + H_2 \longrightarrow CH_x + H$	Formation of CH_x species
22	$C + H_2 \longrightarrow CH_x$	Radiative association
23	$H_2 + FUV \longrightarrow 2H$	Photo-dissociation
24	$H_2 + CR \longrightarrow 2H$	Cosmic ray dissociation
	C^+	**Reaction 21 and**
25	$C^+ + e \longrightarrow C + \gamma$	Radiative recombination
26	$He^+ + CO \longrightarrow He + C^+ + O$	Dissociative charge exchange
27	$C^+ + OH_x \longrightarrow HCO^+$	HCO^+ formation
28	$C + FUV \longrightarrow C^+ + e$	Photo-ionization
29	$C + CR \longrightarrow C^+ + e$	Cosmic-ray ionization
30	$C + CR\text{-photon} \longrightarrow C^+ + e$	Ionization by Cosmic-ray-induced photon
	CH_x	**Reactions 17, 21, 22, and**
31	$O + CH_x \longrightarrow CO + H$	CO formation
32	$CH_x + FUV \longrightarrow C + H$	Photo-dissociation
	OH_x	**Reactions 18, 27, and**
33	$C + OH_x \longrightarrow CO + H$	CO formation
34	$OH_x + FUV \longrightarrow O + H$	Photo-dissociation
	HCO^+	**Reactions 6, 19, 27, and**
35	$HCO^+ + e \longrightarrow CO + H$	CO formation
	CO	**Reactions 6, 19, 26, 31, 33, 35, and**
36	$CO + FUV \longrightarrow C + O$	Photo-dissociation
37	$CO + CR \longrightarrow C + O$	Cosmic-ray dissociation
38	$CO + CR\text{-photon} \longrightarrow C + O$	Dissociation by Cosmic-ray-induced photon
	M^+	**Reaction 15 and**
39	$M^+ + e \longrightarrow M + \gamma$	Radiative recombination
40	$M + FUV \longrightarrow M^+ + e$	Photo-ionization
	He^+	**Reactions 5, 20, 26, and**
41	$He^+ + e \longrightarrow He + \gamma$	Radiative + dielectric recombination
42	$He + CR \longrightarrow He^+ + e$	Cosmic-ray ionization

species i in the network is analogous to Equation 4.1:

$$\frac{\partial \rho_i}{\partial t} + \nabla \cdot (\rho_i \mathbf{v}) = C_i(\rho, T, ...) - D_i(\rho, T, ...) \,, \tag{4.7}$$

where ρ_i is the mass density of species i, v is the gas velocity, C_i and D_i are the creation and destruction rates, respectively. The creation/destruction rates depend on the density and temperature of the gas as well as on the density of other chemical species. The operator splitting method is utilized for the non-equilibrium evolution of the chemical species. In order to do so, the advection terms on the left side of Equation 4.7 are separated from the source (C_i) and sink (D_i) terms on the right side, so that two sets of *simpler* equations are obtained. The first set of equations is given by

$$\frac{\partial \rho_i}{\partial t} + \nabla \cdot (\rho_i \mathbf{v}) = 0 \,. \tag{4.8}$$

These equations consider the existing chemical abundances in the simulation domain as scalars, and can be solved by the HYDRO unit of FLASH as for any other scalar field variable. The remaining part of Equation 4.7 is given by another set of equations

$$\frac{\mathrm{d}\rho_i}{\mathrm{d}t} = C_i(\rho, T, ...) - D_i(\rho, T, ...) \,, \tag{4.9}$$

which is a set of ordinary differential equations (ODEs). These ODEs are solved together with the ODE obtained by operator splitting the internal energy term $\dot{u}_{\mathrm{chem}}$ from Equation 4.3. These ODEs are solved simultaneously so that the change in chemical abundances due to chemical reactions is immediately reflected in the internal energy.

4.3 | SELF-GRAVITY

The acceleration due to gas self-gravity ($\mathbf{g} = -\nabla\Phi$) is obtained by solving the Poisson equation for the gas

$$\Delta\Phi = 4\pi G\rho \,, \tag{4.10}$$

where Φ and G refer to the gravitational potential and the gravitational constant, respectively.

The GRAVITY unit in FLASH, developed by Wünsch et al. (2018), calculates $\mathbf{g}$ in a PARAMESH-based 3D Cartesian grid with an OctTree-based method. The tree structure defines how a computational domain is divided into smaller parts. In the most common OctTree structure, the 3D domain is divided into eight sub-domains of equal volume (called blocks in FLASH, but also referred to as the nodes of the tree structure). Note that each such sub-domain in turn contain 8^3 cells. This division is repeated until the cells provide a desired numerical or spatial resolution.

While calculating the gravitational potential, in some cases, the total mass and centre of mass provided by a certain block might be acceptable to obtain sufficiently accurate results. In other cases, detailed mass distribution from smaller blocks within the block might be required. The Multi-pole Acceptance Criterion (MAC) is used to decide which route to follow during a calculation. For the calculation of $\mathbf{g}$ in the simulations, the geometric MAC introduced by Barnes & Hut

(1986) is used. The criterion is based on the ratio of the angular size of the block containing the gravitating source and the distance between this source block and the computational cell where the gravitational acceleration is to be determined. In the simulations presented here, a block is accepted by the MAC if the angular size is smaller than the limiting angle parameter $\theta_{\rm lim} = 0.5$.

4.4 | DUST AND MOLECULAR SHIELDING

The chemical reactions, radiative heating, and cooling of the various phases of the ISM are affected by the intensity of the radiation felt locally. In order to model the attenuation of the ISRF due to dust, H_2 and CO (self-)shielding and the shielding of CO by H_2 in every single cell in the computational domain, the OPTICALDEPTH unit by Wünsch et al. (2018) is used. The algorithm is similar to the TREECOL algorithm (Clark et al. 2012a) and has been used in Gatto et al. (2015); Walch et al. (2015); Girichidis et al. (2016); Gatto et al. (2017); Peters et al. (2017) and Seifried et al. (2017).

For each cell, the OPTICALDEPTH unit creates a HEALPIX structure (pixelized sphere around the cell, Górski et al. 2005) to facilitate the calculation of radiation intensity reaching the cell from all directions. The recommended number of HEALPIX pixels of $N_{\rm PIX} = 48$ is used so that the angular size of each HEALPIX pixel is similar to the limiting angle used for MAC, i.e. $\theta_{\rm lim} = 0.5$ (see Wünsch et al. 2018). The unit constructs the column density of total hydrogen nuclei, of the H_2 molecules, and of the CO molecules in each HEALPIX pixel around a cell. Then, the unit stores three different variables that can be accessed globally: average visual extinction $A_{\rm V}$, and two shielding coefficients ($f_{\rm shield,H_2}$ and $f_{\rm shield,CO}$), so that other units such as CHEMISTRY can use them for chemical reactions, heating, and cooling. The calculation of these variables is briefly described below.

AVERAGE VISUAL EXTINCTION ($A_{\rm V}$)

Once the total hydrogen column density ($N_{\rm H,tot}$) in a pixel is known, the corresponding visual extinction $A_{\rm V}$ along that line of sight is calculated via the expression (Draine & Bertoldi 1996; Glover et al. 2010)

$$A_{\rm V} = \frac{N_{\rm H,tot}}{1.87 \times 10^{21}\ {\rm cm}^{-2}}\,. \tag{4.11}$$

In the simulation, the visual extinction experienced by each cell are $A_{\rm V}$ values averaged in 3D over all the HEALPIX pixel values

$$A_{\rm V} = -\frac{1}{2.5}\ln\left[\frac{1}{N_{\rm PIX}}\sum_{i_{\rm PIX}=1}^{N_{\rm PIX}} \exp\left(-2.5\frac{N_{{\rm H,tot},i_{\rm PIX}}}{1.87 \times 10^{21}\ {\rm cm}^{-2}}\right)\right]. \tag{4.12}$$

The mean $A_{\rm V}$ is calculated in this manner because the shielding of the ISRF by dust is an exponential function of $A_{\rm V}$ (for example, $f_{\rm dust,CO} = \exp(-2.5A_{\rm V})$, as mentioned below). Thus, unless otherwise stated, the $A_{\rm V}$ mentioned in this thesis is the 3D, average visual extinction; this is different from the $A_{\rm V}$ magnitude commonly derived from the column density maps in observational studies.

SHIELDING COEFFICIENTS

The H_2 photo-dissociation rate given by Draine & Bertoldi (1996)

$$R_{\mathrm{pd,H_2}} = R_{\mathrm{pd,H_2,thin}} \, f_{\mathrm{dust,H_2}} \, f_{\mathrm{shield,H_2}} \,, \tag{4.13}$$

where $R_{\mathrm{pd,H_2,thin}} = 3.3 \times 10^{-11}\ \mathrm{s^{-1}}\ G_0$ is the H_2 photo-dissociation rate in optically thin medium and $G_0 = 1.7$ in Habing units denotes the strength of the interstellar radiation field. The factor $f_{\mathrm{dust,H_2}} = \exp(-3.5 A_{\mathrm{V}})$ accounts for the dust extinction experienced by the radiation responsible for the dissociation H_2 molecules. If $f_{\mathrm{dust,H_2}} = 0$, the radiation incident on the H_2 molecules is completely attenuated by dust. Similarly, $f_{\mathrm{shield,H_2}}$ is the H_2 self-shielding factor which is a function of H_2 column density and gas temperature

$$f_{\mathrm{shield,H_2}} = \frac{0.965}{(1 + x/b_5)^2} + \frac{0.035}{\sqrt{1+x}} \exp\left(-8.5 \times 10^{-4} \sqrt{1+x}\right) , \tag{4.14}$$

where $x = N_{\mathrm{H_2}} / \left(5 \times 10^{14}\ \mathrm{cm^{-2}}\right)$, $b_5 = b / \left(10^5\ \mathrm{cm\,s^{-1}}\right)$, and $b = \sqrt{k_{\mathrm{B}} T / m_{\mathrm{H}}}$ is the Doppler broadening parameter.

The CO photo-dissociation rate is given by van Dishoeck & Black (1988)

$$R_{\mathrm{pd,CO}} = R_{\mathrm{pd,CO,thin}} \, f_{\mathrm{dust,CO}} \, f_{\mathrm{shield,CO}} \,, \tag{4.15}$$

where $R_{\mathrm{pd,CO,thin}} = 1.235 \times 10^{-10}\ \mathrm{s^{-1}}\ G_0$ is the CO photo-dissociation rate in optically thin medium and $f_{\mathrm{dust,CO}} = \exp(-2.5 A_{\mathrm{V}})$ is the dust shielding of the radiation responsible for CO dissociation. The factor $f_{\mathrm{shield,CO}}$ incorporates the shielding contribution from H_2 as well as CO, as tabulated by Lee et al. (1996). For H_2 column densities $N_{\mathrm{H_2}} \gtrsim 10^{21}\ \mathrm{cm^{-2}}$, the shielding factor of CO by H_2 becomes < 0.5 and for CO column densities $N_{\mathrm{CO}} \gtrsim 10^{15}\ \mathrm{cm^{-2}}$, the CO self-shielding factor becomes < 0.5.

4.5 | TURBULENCE

A fluid is said to be turbulent in nature when the fluid motion is nonlinear, and the fluid elements are being compressed, dilated, or stretched by the velocity field. In such a scenario, the velocity field also distorts the existing gravitational or magnetic fields in the system, that in turn exert feedback onto the velocity field. A turbulent medium is a strongly fluctuating medium with motions on multiple scales. A well known effect of turbulence in the fluid is the way kinetic energy is distributed among the various spatial scales, leading to the concept of the turbulent cascade. This cascade is characterized by the presence of the so called inertial range of turbulence where the flow of kinetic energy is not directly affected by either the energy injection at large scales or the energy dissipation at small scales. Such an inertial range has been shown to exist for both the incompressible and compressible turbulence (Frisch 1995; Aluie 2013).

The energy of the turbulence is injected on the largest scales via galactic processes (Roman-Duval et al. 2010; Salomé et al. 2016), galactic mergers (Kennicutt et al. 1987), etc. and on the comparatively smaller scales via various stellar feedback processes (Mac Low & Klessen 2004; Gatto et al. 2015; Haid et al. 2016). The kinetic energy then cascades down to smaller and smaller scales, eventually dissipating via atomic viscosity. In addition, the thermal instability (see Section 2.2.1), shear instability (Kelvin-Helmholtz instability), and non-linear thin shell instability (NTSI, Vishniac (1994)) occur when layers of fluid elements flow with differential velocity or collide with each other at an interface. In contrast to the energy injection process mentioned above, these instabilities induce density sub-structures at small scales of the ISM. Overall, turbulence is a vital component in determining the density and velocity structure of the phases of the ISM besides gravity, magnetic field, and the thermo-chemical properties of the gas (Elmegreen & Scalo 2004).

In order to introduce random turbulent motion in the fluid, numerical models often use an additional acceleration term in the Euler equation. It exerts an additional force in the fluid and is often called a forcing term or a stirring term. This term can either be static in space but vary with time, or it can be specified to vary in both space and time.

The STIR unit in FLASH, developed by Federrath et al. (2010); Konstandin et al. (2015), is used to drive turbulent velocities in the gas. It uses a random forcing field that varies in space and time via the Ornstein-Uhlenbeck process . In Fourier space, the forcing acceleration ($\mathbf{F}$) in Equations 4.2 and 4.3 evolves as

$$\mathrm{d}\tilde{\mathbf{F}}(\mathbf{k},t) = \tilde{F}_0(\mathbf{k},t)\mathcal{P}^{\zeta}(\mathbf{k})\mathrm{d}\mathbf{W}(t) - \tilde{\mathbf{F}}(\mathbf{k},t)\frac{\mathrm{d}t}{T_{\mathrm{ac}}}\,. \tag{4.16}$$

Here, $\tilde{\mathbf{F}}(\mathbf{k},t)$ is the Fourier transform of the forcing acceleration as a function of wave-vector $\mathbf{k}$ and time t.

The first term on the right hand side is a diffusion term. $\tilde{F}_0(\mathbf{k},t)$ is the forcing amplitude of the $\mathbf{k}$ mode. The $\mathbf{W}(t)$ factor is the Wiener process that introduces Gaussian random perturbations in $\tilde{F}_0(\mathbf{k},t)$; therefore, $\mathrm{d}\mathbf{W}(t)$ is simply $\mathcal{N}(0,\mathrm{d}t)$, i.e. a normal distribution with zero mean and standard deviation $\mathrm{d}t$. The projection operator $\mathcal{P}^{\zeta}(\mathbf{k})$ projects the perturbed Fourier amplitudes to $\mathbf{k}$ in order to obtain a desired mixture of solenoidal to compressive modes. For $\zeta = 0.5$, a thermal mix of modes is obtained, which is a 2:1 ratio of the solenoidal and compressive modes in the forcing field. The second term represents the exponential decay of the correlation of the Fourier modes with themselves over a time-scale T_{ac}. The auto-correlation time T_{ac} is set similar to the turbulent dissipation time or the turbulent crossing time (see Equation 2.6).

4.6 | TRACER PARTICLES

Tracer particles help to visualize and study the fluid flow properties. Leaves or wood splinters on a flowing river are some crude examples of such tracer particles readily found in nature. In lab experiments, light absorbing materials, highly reflective spheres, or fluorescent spheres can be introduced in the fluid as tracer particles. In the numerical modelling, tracer particles (also referred to as passive particles) can be simulated, whose only task is to follow the fluid flow and store various physical and chemical properties of the local environment as the fluid evolves in the simulation domain.

THE NEED FOR TRACER PARTICLES IN GRID CODES

The evolution of gas in astrophysical mechanisms can be carried out with either (a) the Eulerian-scheme based grid code simulations such as the AMR techniques used in this project or (b) the Lagrangian-scheme based Smooth Particle Hydrodynamics (SPH) simulations (for e.g. Gingold & Monaghan 1977; Price 2012). In grid codes such as FLASH, the volume of the simulation domain is discretized and the physical properties such as the mass, momentum, and energy are transferred from one volume element (i.e. the individual cell in the simulation) to another. In doing so, the evolutionary history of a fluid element moving through the simulation domain is lost. On the other hand, SPH simulations have unique particles moving through the simulation domain and such particles trivially provide the trajectory of the gas packets. However, such particles provide information about the conserved physical properties such as the mass density of the gas only as derived quantities. In order to mimic the ability of the particles to provide the gas-trajectory in SPH codes, grid codes implement tracer particles. Tracer particles are passive particles, i.e. they do not affect the dynamical or chemical evolution of the gas in any sense. Using the velocity of the gas in a cell containing a certain particle, each particle can be advected through the gas, similar to how the chemical species are advected via Equation 4.8.

The FLASH code allows to introduce tracer particles in a simulation via the PARTICLES unit and uses the local velocity field method of advection to follow the gas packets. Genel et al. (2013) studied two different methods to advect the particles through the grid codes: the local velocity field method and the Monte Carlo sampling method. They conclude that the Monte Carlo sampling of tracer particles, based on the flux of mass through the cell boundaries, provides a greater accuracy in tracing the gas flow with the passive particles. Therefore, this caveat of the tracer particle implementation in the FLASH code must be taken into consideration during the analysis of the tracer particles.

4.7 | SIMULATION RESOLUTION

The finite volume discretization method divides a computational domain into small volume elements, generally called cells or zones. These cells represent individual fluid elements and store information about the thermodynamical and chemical quantities as cell-averaged values. Usually, the domain is made up of cells that are identical in size; this method of discretization is called “uniform refinement" where the computational grid has the same resolution throughout the domain. However, when only certain regions of the computational domain are of interest for a study, it is usually unnecessary to spend the computational power to resolve dynamically unimportant or dormant regions. Thus, in order to selectively resolve high-gradient regions of a fluid flow, DeZeeuw & Powell (1993) presented a method for adaptive refinement of the Cartesian mesh.

In the simulations of fluid dynamics, the spatial and temporal resolution with which the various physical and chemical processes are being modelled require scrutiny. The gas distribution becomes consistent only if the gas dynamics is resolved. For instance, Heitsch et al. (2011) have illustrated the effect of the simulation resolution on the velocity dispersion. With increasing resolution, thermal instabilities occur at smaller scales and restrict the growth of dynamical instabilities only near their place of origin (Vietri et al. 1997). As a result, thermal effects are found to lower the velocity dispersion of the gas by removing contributions from dynamical instabilities. Ideally, correct numerical modelling of the evolution of the ISM should be able to resolve all such scales where instabilities originate. At the same time, it is not possible to computationally achieve the infinite resolution found in nature. Therefore, numerical errors always arise from the approximations made by a simulation at the highest allowed spatial/temporal resolution.

While working with finite resolution, different aspects of the simulation need to be resolved depending on the quantity we want to investigate. One famous example is the relation between the spatial resolution and the temporal resolution of the simulation. Similar to the finite volume discretization of the computational domain into cells, the system is evolved in time via discrete time-steps called **the hydrodynamical time-step**. This time is closely coupled with the spatial resolution (i.e. the size of each individual cell). It is constrained by the Courant-Friedrichs-Lewy (CFL) condition (Courant et al. 1967).

$$\Delta t = \mathrm{CFL} \times \frac{\Delta x}{v}, \tag{4.17}$$

where Δx is the size of the grid cell, v is the velocity of the fluid element in the cell, and the constant factor $\mathrm{CFL} \leq 1$ (see e.g. Derigs et al. 2016). This condition constrains a fluid element to traverse not more than one cell size Δx in a time step Δt, and is necessary to ensure the convergence of the fluid flow mechanism in explicit time integration schemes. When the hydrodynamical time-scale becomes comparable to other physical time-scales, such as the free-fall time, cooling time, or molecule formation time, numerical artefacts may arise.

Another example is the Truelove et al. (1997) criterion to resolve the Jeans length-scale by at least 4 grid cells in order to avoid any artificial fragmentation in a collapsing cloud. This criterion is based on the finding by Jeans (1902) that perturbations on spatial scales larger than the Jeans length (λ_J), given by

$$\lambda_J = \sqrt{\frac{\pi c_s^2}{G\rho}} \tag{4.18}$$

are unstable because the thermal pressure of the gas cannot balance the gas self-gravity. This length-scale decreases on decreasing the sound speed (c_s) and on increasing the density of the gas (ρ). Since the numerical errors occur at the scale of the spatial resolution, ensuring this resolution scale is sufficiently smaller than the local Jeans length keeps the errors/perturbations from becoming unstable.

FLASH implements the adaptive mesh refinement (AMR) method via the PARAMESH package of the GRID unit; it determines whether a particular region of the simulation domain needs to be further refined based on the second derivative of a certain cell-variable. The cell-variable that is used to check the refinement can be defined by the user; a practical variable for such AMR techniques is the density of the cell, so that large density gradients are refined. In particular, if the total second derivative of density in a cell is more than 80% of the average gradient of density around the cell, the block containing the cell will be refined in the next step. In addition to the refinement of density gradient, the Jeans refinement is used to resolve the

Jeans length (Equation 4.18) with at least N_J cells in one dimension. The Truelove et al. (1997) criterion suggests $N_J \geq 4$. A combination of these refinement methods allows the simulation to handle the formation of H_2 from the WNM/CNM at large spatial scales, as well as the evolution of H_2 and CO in the small, dense and gravitating regions.

The resolution of a simulation using the AMR method is commonly noted in terms of the refinement level (R). A single block containing 8^3 cells (i.e. 8 cells along each dimension) corresponds to the first refinement level ($R = 1$). For each higher refinement level, the number of blocks along each dimension increases by 2; thus, the cell size obtained for any refinement level R is

$$\Delta x = \frac{L_0}{2^{R-1} \times 8} = \frac{L_0}{2^{R+2}}, \tag{4.19}$$

where L_0 is the size of the block at $R = 1$. In uniform refinement methods, R is constant throughout the simulation domain. The AMR methods allow R to vary between the minimum (R_{min}) and maximum (R_{max}) values indicated during the setup of a simulation.

RESOLUTION IN EXISTING SIMULATIONS

The influence of the numerical resolution on the structure and composition of MCs should be a matter of discussion in the analyses of results from every simulation. Federrath (2013) performed very high resolution isothermal TB simulations without gravity and concluded that a numerical resolution of 1024^3 or higher is needed to get a converged density distribution with $< 20\%$ difference from the “infinite-resolution limit". In the simulations by Glover et al. (2010), Micic et al. (2012), Valdivia et al. (2016), Seifried et al. (2017) – all of which model the formation of MCs with coupled chemistry networks – it is noted that a spatial resolution of ~ 0.1 pc seems to be necessary and also sufficient to follow the H_2 abundance accurately. CO has a comparatively complex chemistry, and its abundance is mostly dependent on the local density and shielding properties of the gas. Gong et al. (2018) concluded that a resolution of $\sim$ 2 pc is sufficient to obtain a converged CO-to-H_2 conversion factor in the chemical post-processing of their simulation of a region of a galactic disk; however, the convergence of the total CO abundance is not achieved for a spatial resolution of up to $\sim$ 1 pc. In Table 3, a brief overview of some existing numerical studies accompanied by their spatial resolution is listed.

Many studies with a coupled chemistry network have done some convergence tests. However, the tests are limited to the investigation of whether the mean gas density distribution or H_2 distribution in the simulation is similar upon increasing the resolution. So far, the spatial resolution needed to model the different chemical species in such 3D simulations has not been consistently determined.

Table 3: Some existing numerical studies of MC formation involving chemistry networks and their resolution. * The mass resolution is converted to spatial resolution according to the conversion factor from Seifried et al. (2017).

Study	**Chemistry information**	**Resolution**
Glover & Mac Low (2007a,b)	Non equilibrium chemistry of H_2	$\Delta x = 0.04$ pc
Dobbs et al. (2008)	SPH simulation to investigate the formation of H_2 molecules in the spiral shocks of a galaxy	mass resolution: 5.4 $M_\odot$ *$\Delta x \sim 3.9$ pc
Walch et al. (2011)	H_2 Chemistry and the evolution of the cold ISM	$\Delta x = 0.9$ pc
Glover & Mac Low (2011)	The relation between the distribution of H_2/CO, gas density, and visual extinction	$\Delta x = 0.15$ pc
Micic et al. (2012)	H_2 formation in different turbulent forcing mechanisms	$\Delta x = 0.08$ pc
Glover & Clark (2012)	Comparison of chemical evolution in multiple chemistry networks	$\Delta x = 0.15$ pc
Clark et al. (2012b)	SPH simulation of the Colliding Flow mechanism with non-equilibrium chemistry	mass resolution: 0.7 $M_\odot$ *$\Delta x \sim 0.5$ pc
Szűcs et al. (2014)	Self consistent evolution of the ^{12}CO and ^{13}CO using non-equilibrium chemistry network	mass resolution: 0.5 $M_\odot$ *$\Delta x \sim 0.3$ pc
Walch et al. (2015)	H_2 and CO chemistry in a region of the galactic disc with supernova driven turbulence	$\Delta x = 4$ pc
Duarte-Cabral et al. (2015)	Synthetic observations of H_2 and CO molecules via SPH simulation of a galaxy	mass resolution: ~ 300 $M_\odot$ *$\Delta x \sim 200$ pc
Valdivia et al. (2016)	The influence of the gas dynamics on the H_2 formation, destruction, and distribution	$\Delta x = 0.05$ pc
Seifried & Walch (2016)	Detailed chemistry of H_2 and CO in star-forming filaments	$\Delta x = 40.3$ AU
Pardi et al. (2017)	H_2 chemistry in the supernova-driven ISM with varying strengths of magnetic field	$\Delta x = 1$ pc
Seifried et al. (2017)	Dynamical and chemical(H_2 and CO) evolution of the molecular clouds formed in the SILCC simulations (Walch et al. 2015)	$\Delta x = 0.12$ pc

5 | Simulation Setup

NOTE

This chapter is adapted from the paper “On the resolution requirements for modelling molecular gas formation in solar neighbourhood conditions" (Joshi et al. 2019), published in Monthly Notices of the Royal Astronomical Society (MNRAS).

This chapter describes the setup of two numerical models used to study the non-equilibrium evolution of chemical species in molecular clouds. The two setups have the same implementation of gravity and chemistry but differ in the size of the computational domain, the initial and boundary conditions, the mechanism of turbulence generation, and the refinement techniques. The setup parameters are chosen such that the simulations resemble existing studies to some degree. A complete list of all the simulations performed for the study is given at the end of the chapter.

As discussed in Chapter 2, MCs are are now understood as short lived, turbulent structures formed out of the diffuse atomic ISM. This is possible via the collision of low density gas, that are initiated by random motion at large scales. This turbulent energy then cascades down to smaller scales, triggers various instabilities in the post-shock regions near the collision interface, that then rapidly produce dense, cold gas. Such a scenario of diffuse cloud collision can be realised in simulations via two common methods: the turbulent periodic box and the colliding flows. In this thesis, these two controlled environments are utilized to follow the non-equilibrium chemical evolution in the ISM self-consistently.

5.1 | TURBULENT BOX

The Turbulent box (TB) simulations became popular following the understanding that turbulence in the MCs is driven via energy injection at large spatial scales (see Section 4.5). The TB model is a controlled system that allows the study of molecular cloud evolution in desired strengths of turbulence. This is achieved by fine-tuning the rate of kinetic energy injection at the desired spatial scales in the simulation domain. In the last two decades, the nature of MCs as dynamical objects dominated by turbulence has been explored via many simulations of driven supersonic turbulence (e.g. Padoan et al. 1999; Mac Low & Klessen 2004; Kritsuk et al. 2011; Federrath 2013). Recently, Padoan et al. (2016) suggested that such TB models are

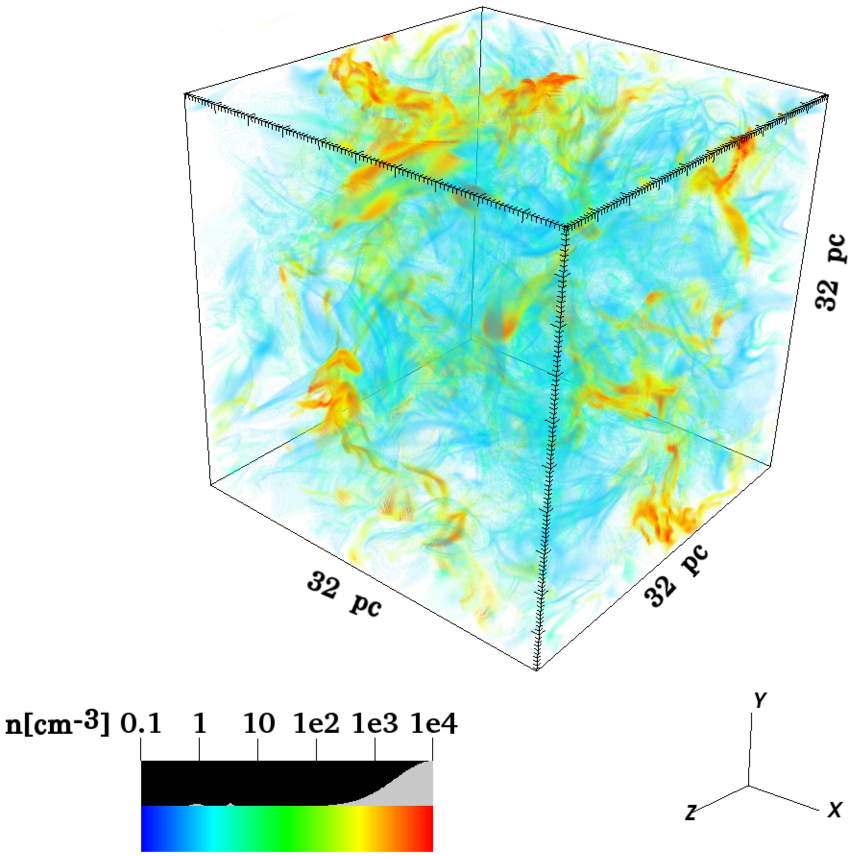

Figure 3: A snapshot of the TB-R6-n030 simulation showing the volume-rendered gas number density distribution at $t = 20$ Myr. Here, the opacity of the surrounding low-density medium is reduced to reveal the dense structures formed inside, as indicated by the opacity bar above the color bar.

close approximations to the supernova-driven turbulence in the ISM. By now, multiple TB simulations using coupled chemistry have been performed (e.g. Glover & Mac Low 2007a; Glover et al. 2010; Walch et al. 2011; Micic et al. 2012; Glover & Clark 2012; Padoan et al. 2017) to study the formation of MCs from WNM or CNM.

The TB simulations presented here are performed in a (32 pc)^3 box – shown in Figure 3 – with periodic boundary conditions for hydrodynamics and gravity.

GAS INITIAL CONDITIONS

The initial densities of H nuclei in the TB simulations span two orders of magnitude: $n_0 = 3$ cm^{-3} (low density), $n_0 = 30$ cm^{-3} (intermediate density), and $n_0 = 300$ cm^{-3} (high density). Table 4 shows the initial conditions, namely the equilibrium values of temperature, sound speed, and the abundance of the chemical species relative to H nuclei in a quiescent medium (without gravity, shielding, and turbulence) for each initial density considered in the simulations. The equilibrium conditions are calculated self-consistently by running the chemical network on a one-zone model with density n_0 for 10^4 Myr and assuming no shielding of the ISRF. The gas remains atomic with all of the hydrogen in H and all of the car-

Table 4: Initial conditions for the different TB and CF simulations: initial gas density ρ_0 (2nd column), number density n_0 of H nuclei (3rd column), temperature T_0 (4th column), and the sound speed c_s (5th column). The initial relative abundances of $x_{\rm He} = 0.1$, $x_{\rm C} = 1.4 \times 10^{-4}$, $x_{\rm O} = 3.2 \times 10^{-4}$, and $x_{\rm M} = 1 \times 10^{-7}$ are common for all the TB and CF simulations. The initially atomic gas with $\mu = 1.27$ contains all of the hydrogen as H atoms and all of the carbon as C^+ ions.

Setup	ρ_0 [g cm^{-3}]	n_0 [cm^{-3}]	T_0 [K]	c_s [km s^{-1}]
TB	7×10^{-24}	3	880	2.4
TB	7×10^{-23}	30	122	0.9
TB	7×10^{-22}	300	88	0.7
CF	1.7×10^{-24}	0.75	4082	5.1

bon atoms as C^+ ions. The isothermal sound speed, c_s, in Table 4 is calculated via Equation 2.4 with $\gamma = 1$ and $\mu = 1.27$.

Figure 4 shows the equilibrium density-temperature curve obtained by the balance of heating and cooling mechanisms implemented in the chemistry network. The multiple equilibrium curves are calculated for gas in a single cell in which the ISRF is attenuated by four different, constant hydrogen nuclei column densities (red: $N_{\rm H} = 10^{18}$ cm^{-2}, green: $N_{\rm H} = 10^{19}$ cm^{-2}, blue: $N_{\rm H} = 10^{20}$ cm^{-2}, and magenta: $N_{\rm H} = 10^{21}$ cm^{-2}). With increasing column density, the equilibrium curve shifts to lower densities and lower temperatures. The thin, dashed line is the analytic equilibrium curve for which $n\Lambda - \Gamma = 0$ (Equation 2.1). Since a realistic shielding of the ISRF is not taken into account for the isolated cell, the gas does not cool to ~ 10 K at high densities. The red, green, and blue dots indicate the position of the three different initial conditions in the TB setup. Thermal instability in the low and intermediate density TB simulations will rapidly produce CNM. The high density TB run starts with gas in the CNM phase. Therefore, a combination of thermal instability and turbulent motions in the simulation will trigger the formation of H_2 and CO from the three different initial conditions.

SIMULATION NOMENCLATURE

The simulations are named TB-R[x]-n[ddd], where TB denotes the Turbulent Box model. R[x] denotes the refinement level x (Equation 4.19) that corresponds to a certain uniform resolution (i.e. $R_{\rm min} = R_{\rm max}$). For $L_0 = 32$ pc,

$$\Delta x = \frac{32 \text{ pc}}{2^{R+2}} = 2^{3-R} \text{ pc}\,. \tag{5.1}$$

The TB simulations are evolved with four different uniform resolutions ranging from the cell size of $\Delta x = 0.5$ pc (64^3 cells; R4) to $\Delta x = 0.063$ pc (512^3 cells; R7). The n[ddd] tag denotes the initial number density of H nuclei in the homogeneous gas. For example, TB-R7-n030 is a turbulent box simulation with $n_0 = 30$ cm^{-3} and refinement level 7. Note that a uniform resolution is obtained in the TB simulations by setting $R_{\rm min} = R_{\rm max}$.

A second set of test simulations with $n_0 = 30$ cm^{-3} and $v_{\rm rms} = 1, 2, 3,$ and 6 km s^{-1} are performed in a smaller (8 pc)^3 box. These simulations have the uniform spatial resolution corresponding to the TB-R[5,6,7]-n030 runs, and are designed to test the effect of $v_{\rm rms}$ on the convergence of the H_2 and CO chemistry (only used in Chapter 10). These 12 special simulations have a “-v[x]" tag at the

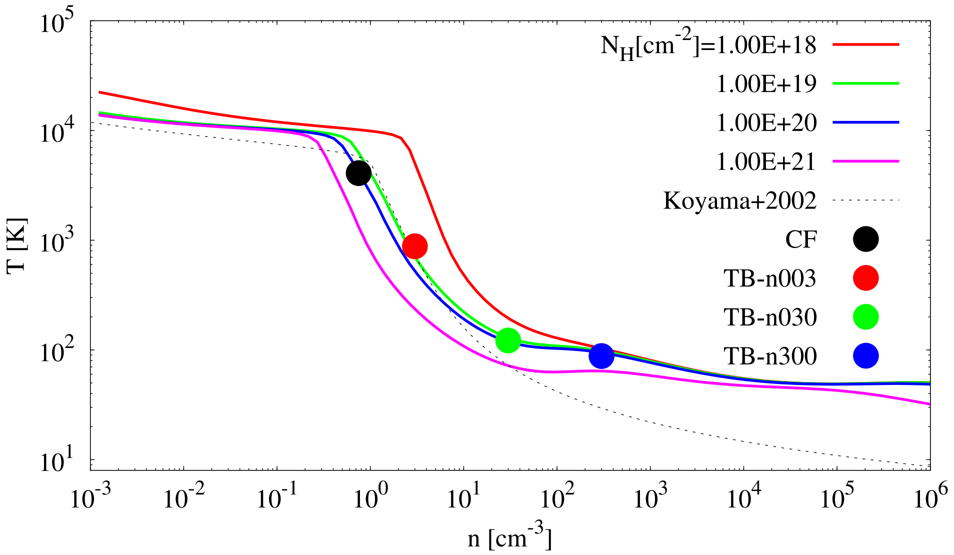

Figure 4: The density-temperature equilibrium curve showing the balance of heating and cooling in the gas. The coloured lines show the balance of heating and cooling calculated by the NL99 chemical network for a cell that is subject to four different hydrogen column density values. The thin, dashed line denotes the equilibrium curve obtained from the rates suggested by Koyama & Inutsuka (2002). The initial conditions for the TB and CF setups are indicated by coloured, filled circles.

end, which indicates the driving velocity, and are run only up to 10 Myr.

Turbulent motions are introduced in the TB simulations on the box scale (size of the box, L pc) such that the forcing amplitude $\tilde{F}_0(\mathbf{k}, t) \neq 0$ (Section 4.5) only for $|\mathbf{k}| = 1$, where $|\mathbf{k}|$ is measured in units of $2\pi/L$. The forcing mechanism is configured to maintain the mass weighted root-mean-square velocity $v_{\rm rms}$ of the gas at 10 km s^{-1} . Therefore, the auto-correlation time in the (32 pc)^3 box, for example, is $T_{\rm ac} = L/v_{\rm rms} = 3.13$ Myr. In order to avoid large-scale advection of fluid, the bulk velocity of the simulation domain is re-normalized to zero in every forcing step throughout the simulation time. To allow for a direct comparison of the different resolution runs, the same turbulence driving pattern is used in all the simulations with the (32 pc)^3 box.

The TB runs are hydrodynamic simulations that exclude magnetic fields. Self-gravity is activated for the simulations only after 10 Myr, when the turbulence is well-developed. For the calculation of dust shielding and molecular (self-)shielding by the OpticalDepth module (Section 4.4), only the contributions from gas within a sphere with radius 16 pc from the cell of interest are included. This radius corresponds to half the box side length in the TB simulations and avoids duplicate contributions from the same gaseous sub-structure across periodic boundary conditions.

The evolution of MCs in the TB simulations are modelled for $t = 20$ Myr. The runs with $n_0 = 300$ cm^{-3} are stopped shortly after 10 Myr because the medium is so dense that some regions collapse immediately due to gravity (further explanation in Chapter 6). The complete list of the TB simulations is given in Table 5.

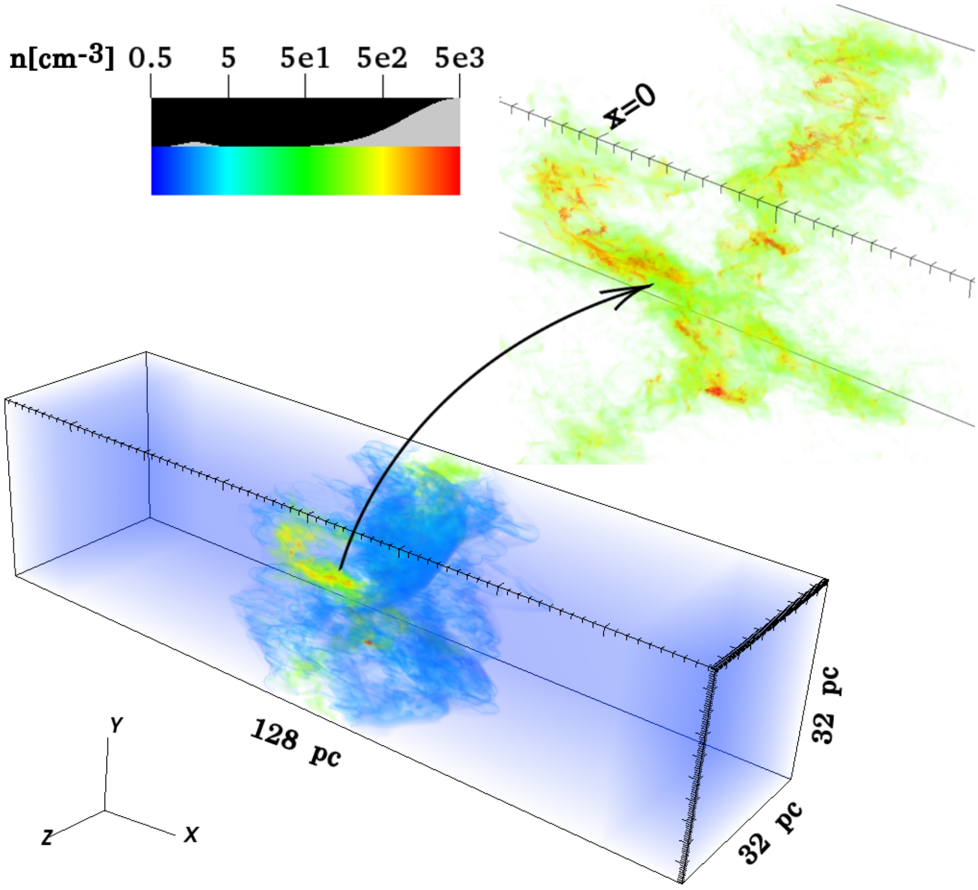

Figure 5: A snapshot of the CF-R6 simulation, showing the volume-rendered gas number density distribution at $t = 20$ Myr. As in Figure 3, the opacity of the incoming low density is reduced to show the dense objects formed in the centre. The zoomed-in region shows the formed filamentary sub-structure.

5.2 | COLLIDING FLOW

The TB models describe random flows, and to form a dense cloud, some sort of convergent flow is required. In order to model the formation of massive MCs from the WNM, the TB models need to simulate an extremely large domain containing the diffuse gas, at the expense of numerical resolution. Therefore, TB models often simulate MC formation from the CNM phase.

The Colliding flow (CF) simulation is a “simple" scenario to model gas accumulation, where two flows of WNM converge to quickly form clumps of cold molecular gas in the resulting collision interface. Various dynamical and thermal instabilities generate turbulence at the interface and the continuous accretion of the inflowing diffuse gas becomes the natural source of turbulence inside the MCs. Thus, the CF models can capture the dynamics and chemistry of the WNM in galactic scales as well as that of molecular clouds in parsec and sub-parsec scales. An extensive set of CF simulations have been performed over the last two decades (e.g. Ballesteros-Paredes et al. 1999; Heitsch et al. 2006; Vázquez-Semadeni et al. 2007; Hennebelle

& Audit 2007; Hennebelle et al. 2007, 2008; Banerjee et al. 2009; Clark et al. 2012b; Körtgen & Banerjee 2015; Fogerty et al. 2016). These CF simulations are able to reproduce the typical velocity dispersion and column densities observed in the MCs (e.g. Klessen & Hennebelle 2010; Heitsch et al. 2011; Valdivia et al. 2016).

The domain of the CF simulation presented here is a 128 pc × 32 pc × 32 pc rectangular cuboid (shown in Figure 5) with inflow boundary conditions in the x–direction and periodic boundaries in the y– and z–directions. Similarly, the gravity boundary condition is isolated in the x–direction and periodic along the y– and z–directions (see Wünsch et al. 2018, for the implementation of mixed gravity boundary conditions). The whole domain is initially filled with WNM, that has a uniform H nuclei number density of $n_0 = 0.75\ \mathrm{cm}^{-3}$. As in Section 5.1, the chemical network is used to calculate the equilibrium temperature and chemical composition for this n_0 and is indicated by the black dot in the Figure 4. The initial conditions for the CF setup is also summarized in Table 4. The dust and molecular shielding is calculated in the same manner as for the TB setup; only the contributions from gas within a sphere with radius 16 pc (half of the y– and z– side length) from the cell of interest are included. Unlike the TB setup, it is not necessary to inject random turbulent accelerations in the gas to form turbulent MCs in the CF setup.

COLLISION INTERFACE

An irregular interface is constructed at the centre of the simulation box to trigger nonlinear thin-shell instabilities. This is an extension of the one-dimensional sinusoidal interface implementation in Heitsch et al. (2006). The collision interface that separates the flows is created by perturbing the $x = 0$ plane using the function

$$x' = A\left[\cos(2 - yz)\cos(k_y y + \phi) + \cos(0.5 - yz)\sin(k_z z)\right] \tag{5.2}$$

where x' is the x–coordinate of the perturbed interface. The parameters that allow one to vary the structure of the collision interface are the amplitude of the perturbation A, the wave-numbers along the y– and z–axis, k_y and k_z, and the phase ϕ. The velocities in y– and z–direction are initially zero, the x–velocity on either side of this interface is assigned with a value of $v_x = \pm 13.6\ \mathrm{km\,s}^{-1}$, so that the collision occurs immediately upon the start of the simulation.

Figure 6 shows the slices of multiple colliding interfaces at the $x = 0$ plane (black regions correspond to positive v_x, white regions to negative v_x). For the presented CF simulations, the interface I5 with $A = 1.6$ pc, $k_y = 2$, $k_z = 1$, and $\phi = 0$, that produces an intermediate amount of molecular gas among the considered interfaces, is chosen. The effect of the choice of the collision interface on the formation of molecules is discussed in Chapter 8 via the CF-R6-I[1-7] runs where I1-I7 denote the different interfaces. The system is evolved up to 20 Myr to allow for dense MC cores to form and evolve.

SIMULATION NOMENCLATURE

The complete list of CF simulations is given in Table 5. The simulations are named CF-R[x] where CF denotes the Colliding Flow model and R[x] denotes the refinement level x that corresponds to a maximum resolution reached via the AMR technique (Equation 4.19). The CF simulation domain is constructed using $4 \times (32\ \mathrm{pc})^3$ blocks stacked along the x–direction. Thus, the relation in Equation 5.1 holds for

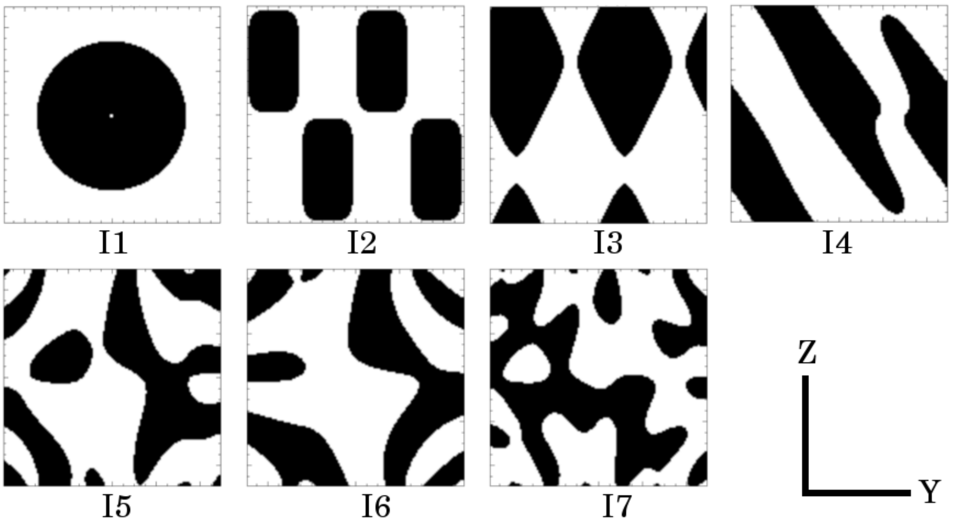

Figure 6: Slices of various collision interfaces at the $x = 0$ plane, showing the x-component of the velocity. Black regions denote gas flowing out of the plane of paper (with positive v_x) and white regions have negative v_x. All the colliding flow simulations presented in this thesis have the interface I5.

the CF runs as well.

The low-resolution CF-R4 and CF-R5 runs have uniform resolution (i.e. $R_{\text{min}} = R_{\text{max}}$). For all higher resolution runs, the base-grid resolution is $\Delta x = 0.25$ pc ($R_{\text{min}} = 5$) and the maximum resolution is achieved using AMR. The refinement via the threshold on the second spatial derivative of the gas density (PARAMESH refinement) is allowed up to $R = 6$ ($\Delta x = 0.125$ pc). For higher refinement levels, the Jeans refinement criterion (see Section 4.7) is used with $N_J = 8$.

TRACER PARTICLES INJECTION

The observations of density and inflow velocity profiles of cores, discussed in Section 2.4, are fairly consistent with the properties of cores in pressure equilibrium formed in simulations of colliding flows (Ballesteros-Paredes et al. 2003). The formation of MC cores in the high resolution CF run is, therefore, an ideal scenario to follow the formation of cores from diffuse WNM and the accretion of gas onto the cores. This thesis focuses on the directionality of the core accretion mechanism, i.e. whether the core accretion is anisotropic (accretion through designated channels) or isotropic (via radial collapse). Note that the CF setup does not include radiative feedback process and magnetic fields, that are known to provide support against the infall of gas onto the cores.

For the purpose of this thesis work, the default functionality of the PARTICLES unit of FLASH is extended to inject new tracer particles into the simulation domain from one or more specified directions at regular time-intervals. In doing so, special care is taken to assign new, unique tags to the particles so that the information carried by existing particles are not lost. The CF simulation is initialized with a uniform number density of tracers n_{tracer}. For the cell-size Δx and gas-velocity v_x at the x–

boundaries, the tracer leaves the cell at the boundary in time

$$t_{\mathrm{tracer,cross}} = \Delta x / |v_x| \tag{5.3}$$

Thus, in order to trace the inflowing fluid elements, new tracers need to be injected at the x–boundaries at time-intervals of $t_{\mathrm{tracer,cross}}$. To keep the mass resolution per tracer particle constant, the number density of the injected particles also needs to be n_{tracer}. For an area of injection A_{inj} at each x–boundary, the volume in which the new tracers need to be injected is $V_{\mathrm{inj}} = \Delta x\, A_{\mathrm{inj}}$. The corresponding number of particles to inject is given by

$$N_{\mathrm{inj}} = n_{\mathrm{tracer}}\, V_{\mathrm{inj}} = n_{\mathrm{tracer}}\, \Delta x\, A_{\mathrm{inj}} \tag{5.4}$$

Thus, a uniform distribution of N_{inj} particles needs to be initialized at the boundary in time-intervals of $t_{\mathrm{tracer,cross}}$.

For the study of the evolution of the gas with tracer particles in the CF simulation, the CF-R10 run is utilized. With $n_{\mathrm{tracer}} = 8$ per pc^3, $|v_x| = 13.6\ \mathrm{km\,s^{-1}}$, $\Delta x = 0.5$ pc (tracer injected only after it crosses through 2 cells), and $A_{\mathrm{inj}} = 1024$ pc^2, $N_{\mathrm{inj}} = 4096$ particles are injected from each x–boundary at regular time intervals of $t_{\mathrm{tracer,cross}} = 0.037$ Myr. The newly injected particles need ~ 5 Myr to reach the central region, where they end up mostly in MCs and MC cores.

In addition to the default position and velocity information, the tracers are configured to store the information of various cell properties such as the density, temperature, total energy, internal energy, gravitational potential energy, the 3D visual extinction A_{V}, as well as the mass fraction of various chemical species such as H, H$_2$, CO, C, and CHx. Due to the periodic boundary conditions in y– and z–directions, none of the particles are lost. This special setup is named CF-R10-tracer. Over the 20 Myr evolution of the gas, more than 5 million tracer particles are handled by the simulation.

Table 5: List of simulations performed for this study, TB – Turbulent box and CF – Colliding flows. R[4-10] denotes the refinement level, related to the spatial resolution Δx (column 2) via Equation 5.1. In the TB runs, the tags of the form n[ddd] denote the initial density of the H nuclei in the homogeneous medium (n_0, column 3). There are two sets of TB runs, one in a $(32\ \mathrm{pc})^3$ box with $v_{\mathrm{rms}} = 10\ \mathrm{km\,s^{-1}}$ and one in a $(8\ \mathrm{pc})^3$ box with different v_{rms}. The latter has a “-v[x]" tag and is used in Chapter 10 to verify the derived resolution requirement. The (effective) resolution of the simulations is denoted by Δx. In the TB runs, the value in parentheses denotes the number of finite volume cells used. In the CF runs, the “AMR" in parentheses denotes that the maximum resolution is obtained via adaptive mesh refinement. The CF-R6-I[1-7] runs are used to study the effect of the choice of collision interface on molecule formation. The CF-R10-tracer run includes tracer particles. Column 5 shows the total simulation time t_{sim}.

Run	Δx	n_0 [cm^{-3}]	v_{rms} [km s^{-1}]	t_{sim} [Myr]
Turbulent box: box size (32 pc)^3				
TB-R4-n003	0.500 pc (64^3)	3	10	20
TB-R4-n030	0.500 pc	30	10	20
TB-R4-n300	0.500 pc	300	10	10
TB-R5-n003	0.250 pc (128^3)	3	10	20
TB-R5-n030	0.250 pc	30	10	20
TB-R5-n300	0.250 pc	300	10	10
TB-R6-n003	0.125 pc (256^3)	3	10	20
TB-R6-n030	0.125 pc	30	10	20
TB-R6-n300	0.125 pc	300	10	10
TB-R7-n003	0.063 pc (512^3)	3	10	20
TB-R7-n030	0.063 pc	30	10	20
TB-R7-n300	0.063 pc	300	10	10
Small turbulent box: box size (8 pc)^3				
TB-R5-n030-v1	0.250 pc (32^3)	30	1	10
TB-R5-n030-v2	0.250 pc	30	2	10
TB-R5-n030-v3	0.250 pc	30	3	10
TB-R5-n030-v6	0.250 pc	30	6	10
TB-R6-n030-v1	0.125 pc (64^3)	30	1	10
TB-R6-n030-v2	0.125 pc	30	2	10
TB-R6-n030-v3	0.125 pc	30	3	10
TB-R6-n030-v6	0.125 pc	30	6	10
TB-R7-n030-v1	0.063 pc (128^3)	30	1	10
TB-R7-n030-v2	0.063 pc	30	2	10
TB-R7-n030-v3	0.063 pc	30	3	10
TB-R7-n030-v6	0.063 pc	30	6	10
Colliding flow				
CF-R4	0.500 pc	0.75	–	20
CF-R5	0.250 pc	0.75	–	20
CF-R6	0.125 pc (AMR)	0.75	–	20
CF-R6-I[1-7]	0.125 pc (AMR)	0.75	–	15
CF-R7	0.063 pc (AMR)	0.75	–	20
CF-R8	0.032 pc (AMR)	0.75	–	20
CF-R9	0.016 pc (AMR)	0.75	–	20
CF-R10	0.008 pc (AMR)	0.75	–	20
CF-R10-tracer	0.008 pc (AMR)	0.75	–	20

6 | General properties of the simulated clouds

NOTE

This chapter is an adaption of the paper “On the resolution requirements for modelling molecular gas formation in solar neighbourhood conditions" (Joshi et al. 2019). As the leading author of the paper, I have performed the required simulations and produced the necessary plots for analysis. The co-authors of the paper have provided me with valuable suggestions, and improved the quality of both the analysis of the results and the conclusion from the research.

The setups of the TB and CF simulations are quite different and thus, the gas evolves differently in each model. The turbulence in the TB runs is continuously driven and energy is injected to maintain a constant velocity dispersion. On the other hand, the turbulence in the CF simulations is a result of various instabilities and the energy is injected via the incoming flows. In addition, the evolution of the gas distribution differs for each initial condition in the different TB and CF runs; therefore, the chemical evolution should also be different.

This chapter provides the description of some general properties of the molecular clouds formed in the simulations. Column densities of the total gas in four representative runs are compared to provide a visual insight into the structure of the formed cloud. The evolution of the mean density and mean velocity dispersion are presented as basic cloud-averaged properties. Finally, the effects of numerical/spatial resolution on the evolution of mean gas density and the column density distribution are shown. Therefore, this chapter provides a guiding narrative to the evolution of gas in the TB and CF simulations. The details of the chemical evolution in the TB and CF models at various resolutions are presented in subsequent chapters.

6.1 | COLUMN DENSITY DISTRIBUTION

The column density distribution is the 2D visualization of the distribution of gas-density in 3D simulations. Similar to how the eye accumulates the 3D information around us by projecting it on the 2D surface of the retina, the column density maps are produced by integrating the density of the gas along a line-of-sight (or column), i.e.

$$\Sigma = \int \rho \, \mathrm{d}s \tag{6.1}$$

where Σ the column density corresponding to the gas volume density ρ and s is the integration path (the line-of-sight).

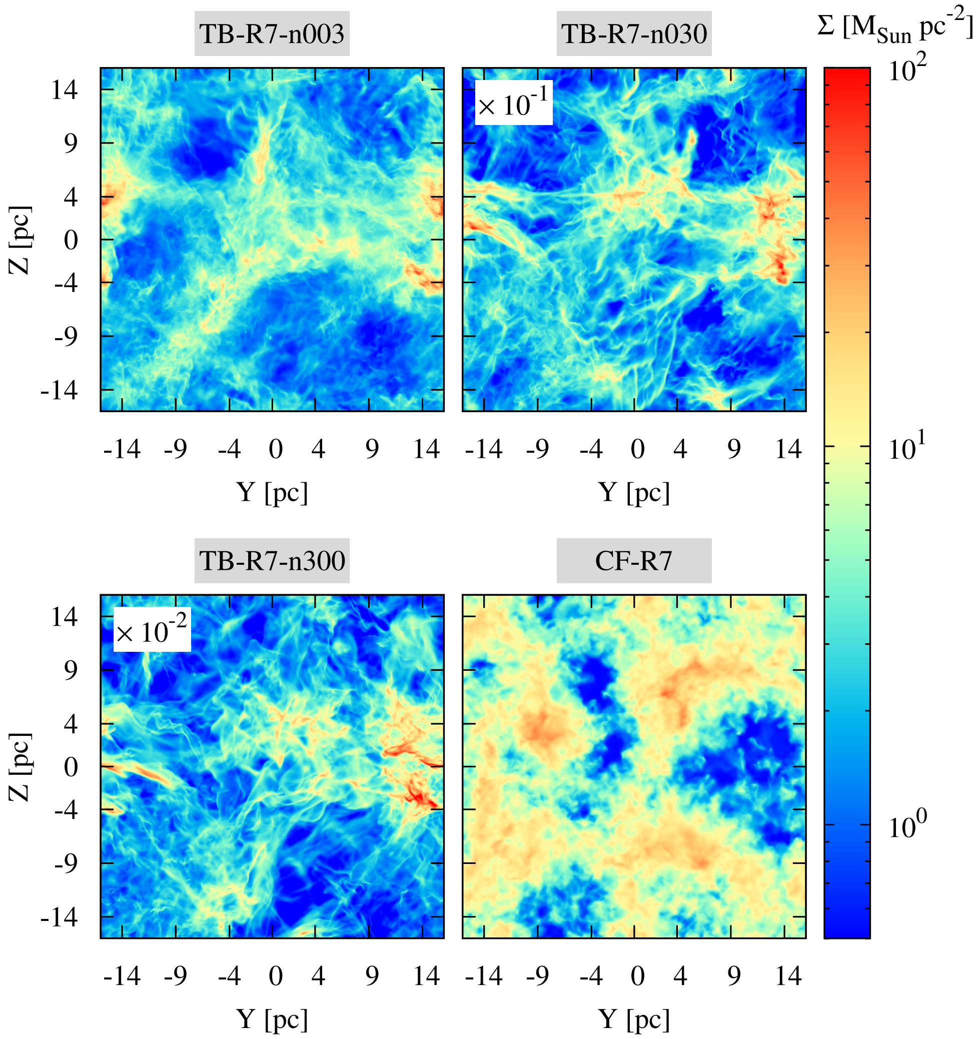

Figure 7: The column density of the total gas in the TB-R7-n003, TB-R7-n030, TB-R7-n300 and CF-R7 simulations with $\Delta x = 0.063$ pc at $t = 10$ Myr, integrated along the x–direction. The column densities of TB-R7-n030 and TB-R7-n300 runs are scaled with a factor of 0.1 and 0.01, respectively, so that the formed sub-structure for all simulations are clearly visible with the same colour-bar. For the CF-R7 run, only the gas near the collision layer with $\mathrm{T} < 4000$ K is taken into account.

To get a general overview of the different gas morphology produced by the TB and CF runs, their column density maps of total gas are compared in Figure 7. The gas density is integrated along the x-axis and the projection on the yz-plane is obtained. Three of the maps correspond to the TB simulations with various mean initial densities and the bottom-right map corresponds to the CF simulation, all at the same spatial resolution ($\Delta x = 0.063$ pc, R7) and at $t = 10$ Myr.

Although the same mechanism is used to produce turbulence in the TB runs, the different runs produce visibly different distribution of the gas column density distribution. In the TB-R7-n003 run, gas column densities as high as $\Sigma \sim 10^2$ $M_\odot$ pc^{-2} are reached. The column density of the TB-R7-n030 and TB-R7-n300 runs are scaled down by a factor of 10 and 100, respectively, for easier comparison with the same scale of the colour-bar. The TB-R7-n030 and TB-R7-n300 runs reach column densities of $\Sigma \sim 10^3$ and 10^4 $M_\odot$ pc^{-2}, respectively (in agreement with the different initial density of the atomic gas in the three runs). Note that the TB runs evolve until $t = 10$ Myr without self-gravity. Therefore, the credit for the filamentary structures in all TB simulations goes to turbulent motions in the gas. In the TB-R7-n003 run, there is a gradual change from the high to low column density areas; the other two TB runs show comparatively sharper transitions and have numerous striation-like structures.

The CF simulation with gravity produces comparatively larger, diffuse clumps with dense gas at their centre and gas column density as high as $\Sigma \sim 10^2$ $M_\odot$ pc^{-2} is obtained. The gradual shift from high to low column density region is even more pronounced in the CF simulation. In the CF runs, gravity is activated from the beginning of the simulation; thus, the combination of turbulent motion and gravitational effects is responsible for structure formation. The thesis focuses only on the evolution of turbulent gas near the collision layer. Thus, unless otherwise stated, the contribution of the stable WNM with $T > 4000$ K flowing along the x-axis is ignored for further analyses.

6.2 | MEAN GAS DENSITY

The evolution of the mean density of the gas in a simulation provides a basic insight into the gas-dynamics. In particular, the mass-weighted mean density helps to easily probe the density inhomogeneities occurring in the simulation. Figure 8 shows the evolution of the mass-weighted mean number density of the gas, $\langle n \rangle_{\mathrm{mass}}$, for the four runs – TB-R7-n003, TB-R7-n030, TB-R7-n300 and CF-R7. The vertical, dashed line at $t = 10$ Myr denotes that gravity is activated in the TB simulations after the turbulence is well-developed in the gas for ~ 3 crossing times.

In all three TB runs, the jumps in $\langle n \rangle_{\mathrm{mass}}$ after 1 Myr arise from local density enhancements when the homogeneous gas first experiences shocks due to the turbulent driving. The value of $\langle n \rangle_{\mathrm{mass}}$ increases by an order of magnitude, and is maintained at this level until gas self-gravity is activated at 10 Myr. In the TB-R7-n003 run, the effect of gravity is not significant. In TB-R7-n030, gravity causes the fragmentation of gas and leads to high density regions. The results of the TB-R[4-7]-n300 runs with gravity are not used for analysis; shortly after self-gravity is switched on at 10 Myr, most of the mass in these runs (above 30%) resides in unresolved dense structures that undergo gravitational collapse (see Section 10.3 for further details on the unresolved densities in the simulations).

In the CF-R7 run, $\langle n \rangle_{\mathrm{mass}}$ experiences a jump at ~ 1 Myr when the colliding streams of gas start to cool down in the centre. After that, it increases smoothly and remains at $\langle n \rangle_{\mathrm{mass}} \sim 30$ cm^{-3} for the first 16 Myr. During this period, $\langle n \rangle_{\mathrm{mass}}$ for the CF run is similar to that of the low density TB run (TB-R7-n003). Self-gravity dominates the gas-dynamics shortly after $t \sim 16$ Myr and increases the mean gas density to

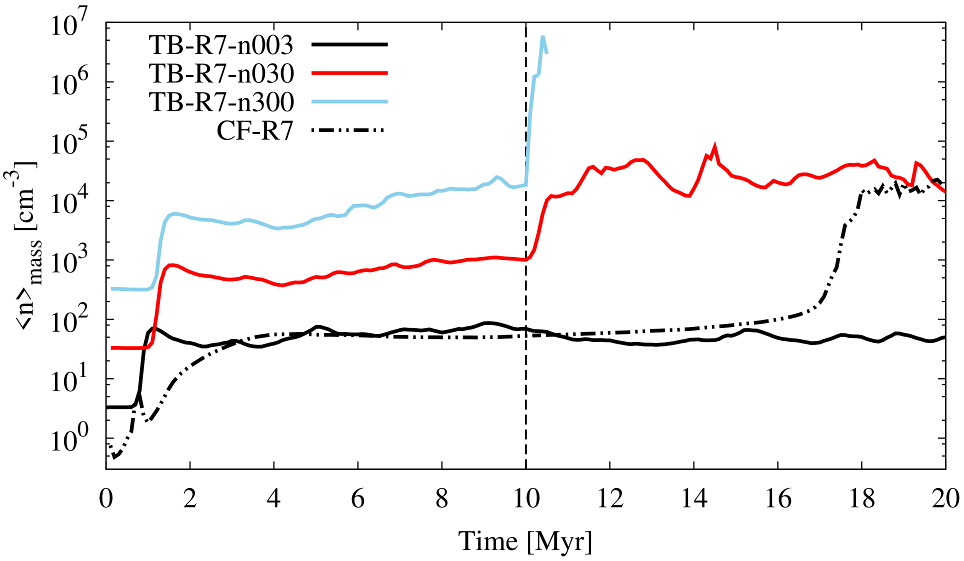

Figure 8: Evolution of the mass-weighted mean number density $\langle n \rangle_{\text{mass}}$ of the gas in the TB-R7-[n003,n030,n300] and CF-R7 runs with $\Delta x = 0.063$ pc. The vertical, dashed line denotes when gravity is turned on in the TB simulations. The TB-R7-n300 run is stopped shortly after gravity is turned on because the box is dominated by free-fall collapse. For the CF-R7 run, only the gas near the collision interface with $T < 4000$ K is taken into account.

$\langle n \rangle_{\text{mass}} \sim 2 \times 10^4$ cm^{-3}, which is similar to that of the intermediate density TB run (TB-R7-n030). Thus, in general, the gravitational effect is not substantial for gas with $\langle n \rangle_{\text{mass}} < 100$ cm^{-3} in both the TB and CF runs.

6.3 | MEAN VELOCITY DISPERSION

The statistical dispersion of velocities of fluid elements about the mean velocity of the gas is a measure of the strength of turbulence in the gas. Figure 9 shows the mass-weighted mean 3D velocity dispersion of the gas ($\langle \sigma \rangle_{\text{mass}}$) for the same four runs – TB-R7-n003, TB-R7-n030, TB-R7-n300 and CF-R7.

All the TB runs maintain $\langle \sigma \rangle_{\text{mass}} \approx 10$ km s^{-1} once the density inhomogeneities arise after 1 Myr. This is enforced by the turbulent driving described in Section 4.5. The fluctuations in $\langle \sigma \rangle_{\text{mass}}$ are quickly settled by adjusting the rate of injection of kinetic energy. On the other hand, for the CF run, the mean velocity dispersion is initially high due to the colliding WNM. The drastic fall of $\langle \sigma \rangle_{\text{mass}}$ at ~ 1 Myr is attributed to the first instances of the dense gas, formed due to thermal and dynamical instabilities. As soon as these slightly over-dense regions are advected by the colliding flows, the value of $\langle \sigma \rangle_{\text{mass}}$ rises. When the dense regions gradually accumulate more gas and cool down in the process (due to thermal instability), the mean velocity dispersion is gradually lowered to $\langle \sigma \rangle_{\text{mass}} = 6$ km s^{-1} by the end of the simulation.

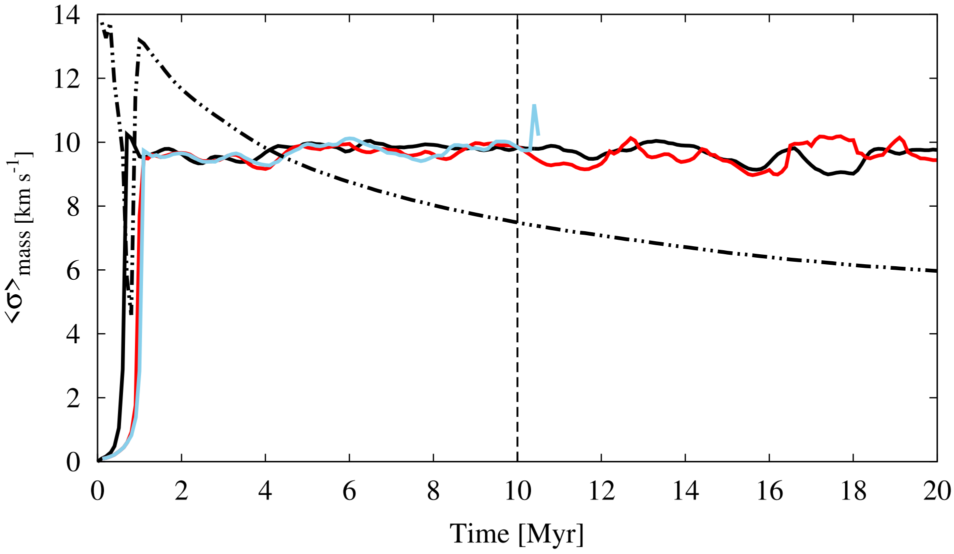

Figure 9: Evolution of the mass-weighted mean 3D velocity dispersion $\langle\sigma\rangle_{\text{mass}}$ of the gas in the TB-R7-[n003,n030,n300] and CF-R7 runs with $\Delta x = 0.063$ pc. The mean velocity dispersion is maintained at a required value in the TB runs and is gradually decreasing in the CF run.

6.4 | RESOLUTION EFFECTS ON THE GAS STRUCTURE

The major factors influencing the chemical evolution in a simulation are the density of the gas in a cell and the distribution of gas, dust, and molecules around it. In this section, the differences in the evolution of these two factors at different resolutions are shown for the intermediate density TB runs (i.e. TB-R[*]-n030). The general trends in the structure of the gas in these runs are valid for the other TB and CF runs, even though they have different initial conditions.

EFFECT ON THE MEAN GAS DENSITY

Figure 10 shows the evolution of the mass weighted mean number density of the gas for the TB-R[4-7]-n030 runs. The high resolution runs have a higher mean density, suggesting that the density of cells in the shocked regions and/or gravitating regions increase with increasing resolution. This holds for both the non-gravitating and the gravitating gas, although the differences are higher when gravity is activated. One exception to this trend is the TB-R6-n030 run, in which the mean density decreases by almost an order of magnitude after $t \sim 13$ Myr. Thus, the turbulence in the TB setup can not only balance, but also overcome the gravitational collapse and eventually destroy the dense regions. The fact that such events occur only at some resolutions further clarifies how the dynamical and chemical evolution of the gas is sensitive to the resolution of the simulation.

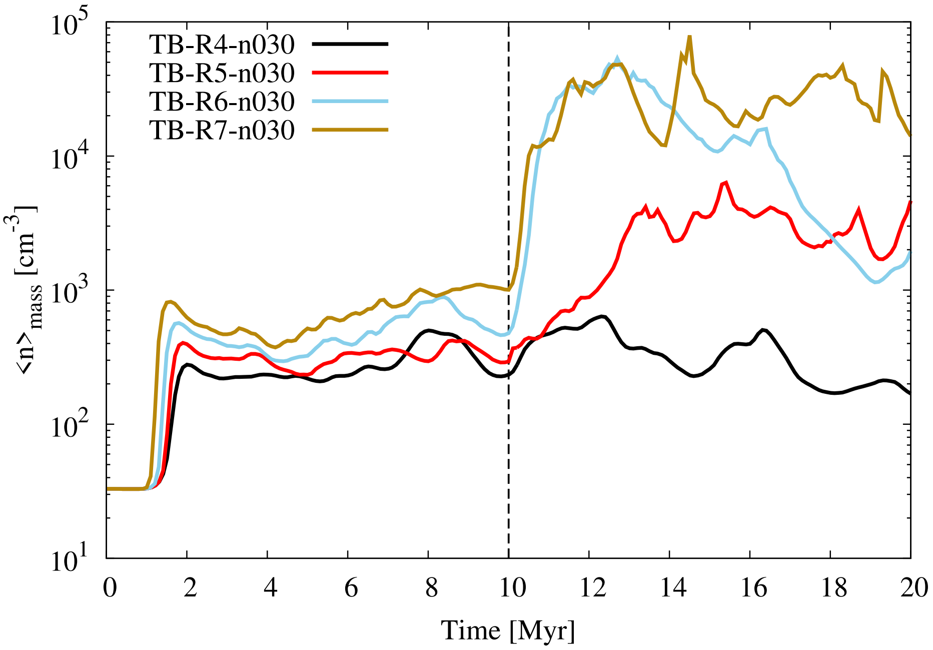

Figure 10: The evolution of the mass weighted mean density $\langle n \rangle_{\text{mass}}$ of the gas in the TB-R[4-7]-n030 runs. The mean density increases, in general, with increasing resolution.

EFFECT ON THE COLUMN DENSITY DISTRIBUTION

Figure 11 shows the evolution of the total gas column density in TB-n030-R5 (first column) and TB-n030-R7 (second column) at $t = 5$, 10, 15 and 20 Myr (top to bottom). The top two rows show that the large scale discrepancy already occurs between the runs with different resolutions as the gas evolves without gravity until 10 Myr. Note that all the runs have the same forcing mechanism to produce and maintain the turbulence. Thus, the position of some dense structures are still similar. However, sub-structures evolve differently. Small variations in the density enhancements between the two different resolution runs get amplified over time and result in large scale differences. The bottom two rows show that these differences are further amplified due to the local gravitational collapse events. The most dense structures no longer lie at similar positions. Throughout the simulation, the low resolution run produces large clumps of gas whereas the high resolution run contains numerous small, filamentary structures. Thus, significant changes are seen as the initial shocks and the dense gravitating structures are resolved more with increasing resolution.

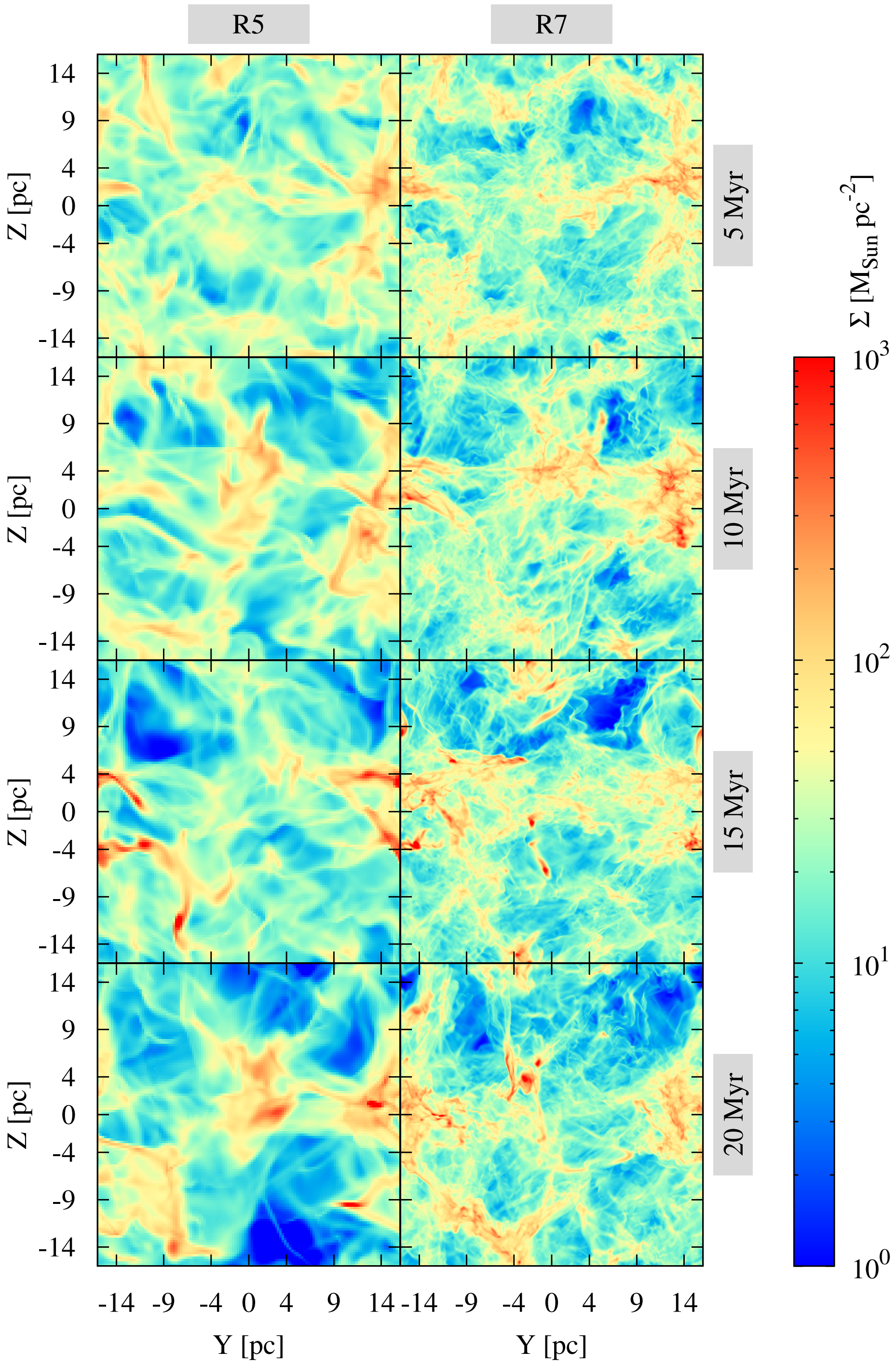

Figure 11: Column density of the total gas in the TB-R5-n030 (first column) and TB-R7-n030 (second column) runs showing the evolution of the gas (top to bottom). Small variations between the different resolution runs at early times result in significant differences in the evolution of both small and large scale structures.

6.5 | CHAPTER SUMMARY

The first part of the chapter presented the differences in the properties of the gas in TB and CF setups, simulated with the same spatial resolution. After 10 Myr of evolution, the strong turbulent motions in the TB setup result in the formation of filamentary structures throughout the simulation domain; this is consistent for all three sets of initial conditions. On the other hand, the mildly turbulent and gravitating gas in the CF setup produces diffuse clumps from the WNM.

For each set of initial conditions in the TB and CF setups, the evolution of the mean gas density is different. The local density enhancements in the turbulent box simulations form rather quickly in the beginning, showing an order of magnitude increase in the mean density. The increase in mean density is comparatively more gradual in the CF simulation. If the mean density of the gas if above 100 cm^{-3}, the effects of gas-self gravity is quite obvious due to rapid accretion processes. The TB setup maintains a mean velocity dispersion of $\langle\sigma\rangle_{\mathrm{mass}} = 10\,\mathrm{km\,s}^{-1}$ in the dense MCs. In the CF setup, the initially high velocity dispersion due to the colliding WNM is gradually reduced as the dense MCs evolve near the collision interface.

The second part of the chapter presented the general effects of the simulation resolution on the evolution of mean gas density and the distribution of the gas in the simulation domain. With increasing resolution, the density of gas in the shocked and/or gravitating regions increases, leading to orders of magnitude difference in the mean density. The column density maps show that low resolution simulations produce large clumps of gas, while thinner filaments with a completely different sub-structure are developed at a higher resolution. This drastic change in the density and the distribution of the gas in the simulation domain is bound to significantly affect the chemical evolution.

7 | Chemical evolution in TB simulations

NOTE

This chapter is an adaption of the paper “On the resolution requirements for modelling molecular gas formation in solar neighbourhood conditions" (Joshi et al. 2019).

The detailed results of the turbulent box simulations are presented in this chapter. In particular, the effect of resolution on the cloud properties such as the gas distribution and molecular content are investigated in the three sets of TB simulations, with initial atomic H number density of 3, 30, and 300 cm^{-3}. First, the column densities of the total gas, hydrogen-species (H and H_2), and carbon-species (C^+, C, and CO) at four different resolutions are presented in Section7.1. This is followed by the evolution of H_2 (Section 7.2) and CO (Section 7.3) in each simulation at different resolutions. The study of chemical evolution is limited to the resolution effects on the evolution of total H_2/CO mass and their average formation time in the simulation. The chapter ends with an investigation of the gas density distribution at various resolutions.

7.1 | COLUMN DENSITY DISTRIBUTION

The changes in the 3D distribution of gas density are reflected in column density maps. It is possible to study the column density not only of the total gas, but also of the individual chemical species. Out of the three sets of TB runs, the runs with intermediate initial density (TB-R[4-7]-n030) are used here to visualize the resolution effects. Since it is not feasible to show the time evolution of 2D maps here, the column density maps at the end of the simulation ($t = 20$ Myr) are presented.

Figure 12 displays the column densities of the total gas, H, and H_2 (from top to bottom) integrated along the x–axis. The resolution of the simulation increases from left to right, as indicated by the refinement levels (R[4-7]) on the top. The gas has already evolved with gravity for 10 Myr at this point. The H column density maps are scaled by $\alpha_{\mathrm{H}} = 10$ to make their low column density visible on the same color scale. The regions with low column densities, in units of $\mathrm{M}_\odot\ \mathrm{pc}^{-2}$, are in blue and

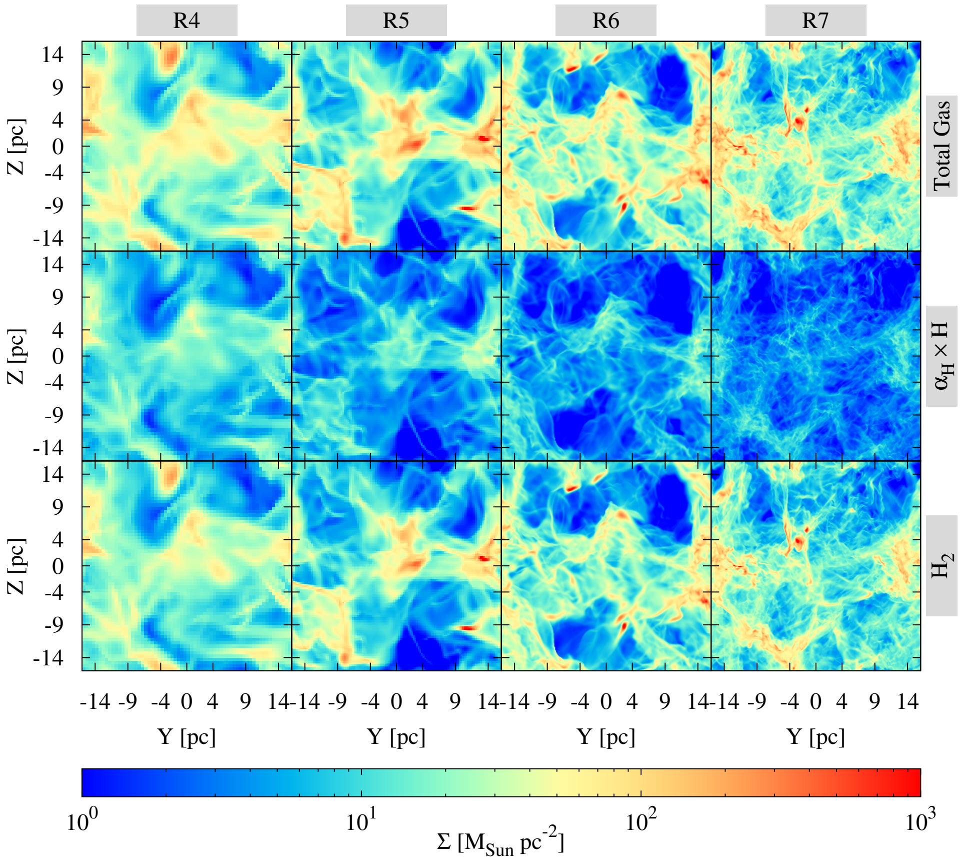

Figure 12: Column density, integrated along the x–direction, of the total gas, H, and H_2 (top to bottom) for increasing resolution (left to right) in the TB-R[4-7]-n030 runs at $t = 20$ Myr. The H column densities are scaled by a factor of $\alpha_H = 10$ to make them visible on the same color scale. Higher resolution runs produce more filamentary structures with more H_2 and CO while the mass in H is reduced.

high column densities are in red. Both the large-scale and the small-scale gas morphology in a simulation change with resolution. In general, the high-resolution runs produce regions with larger column densities. The TB-R7-n030 run contains multiple regions with $\Sigma \gtrsim 10^3\ \mathrm{M}_\odot\ \mathrm{pc}^{-2}$, while the maximum column density in the TB-R4-n030 run is still below $\Sigma = 10^3\ \mathrm{M}_\odot\ \mathrm{pc}^{-2}$. With increasing resolution, numerous denser, but finer and more filamentary structures form. Interestingly, the column density of H decreases as the resolution increases since more H is converted to H_2 that resides either in the dense cores or in the filamentary structures. At all resolutions, the H_2 column density map closely resembles the total gas column density, indicating the gas is mostly molecular at this stage.

Figure 13 shows the comparison of the column densities of carbon-species – C^+, C, and CO (from top to bottom) – with the same layout and colour-bar-scale as in Figure 12. These column densities are scaled by a factor

$$\alpha_C = \frac{1}{x_{C,tot} \times \mu_C} = 595\,, \tag{7.1}$$

where $x_{C,tot} = 1.4 \times 10^{-4}$ is the relative abundance of carbon atoms in the sim-

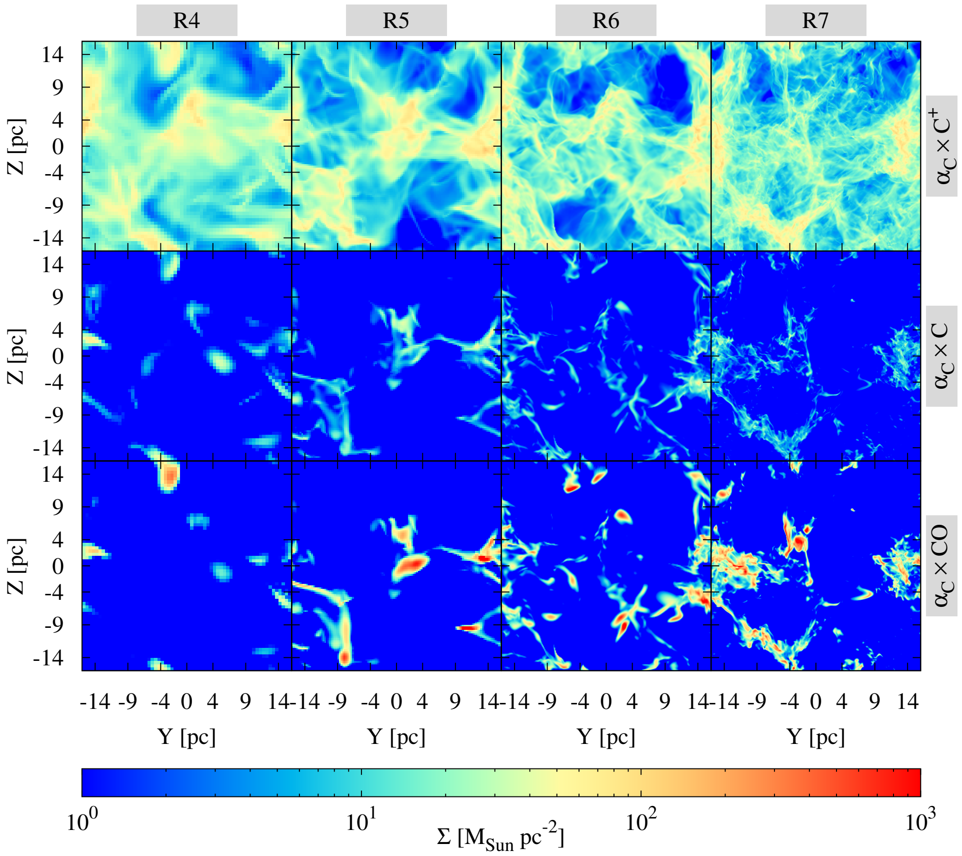

Figure 13: As in Figure 12, now for the carbon-species. The column densities are scaled by a factor of $\alpha_C = 595$ (see Equation 7.1) for an easier comparison with the column densities of hydrogen-species on the same color-scale. Higher resolution runs produce more filamentary structures with more CO inside the H_2 rich regions while the mass in C is reduced.

ulations and $\mu_C = m_C/m_H = 12.011$ is the atomic mass of carbon. This factor accounts for the lower abundance but higher mass of the carbon atoms compared to the H atoms, and allows for an easier comparison with the column densities of hydrogen-species.

A low and diffuse C^+ column density is found throughout the simulation domain. The column density of C is also low and mainly traces the outskirts of the CO rich regions, showing regions of active photo-dissociation. The regions of high CO column density are only found inside the H_2-rich regions. Here, the amount of both C^+ and C is negligible.

Thus, the distribution of all chemical species at the end of the simulation differ greatly with increasing resolution. In other words, the evolution of chemical species in a simulation is substantially affected by the choice of resolution. In the following sections, the evolution of the total H_2 and CO content in all 12 TB runs are presented.

7.2 | EVOLUTION OF H_2 IN TB SETUP

This section presents the evolution of H_2 in the TB simulations with various initial conditions and resolutions. At first, two quantities are calculated to compare the evolution of H_2 at four different resolutions.

MASS-FRACTION OF H_2

The maximum total mass of all H_2 molecules in a simulation is the total mass of all hydrogen nuclei. Analogously, the maximum number of H_2 molecules in a simulation is half of the total hydrogen nuclei. The mass-fraction of H_2 (f_{H_2}) captures the essence of both of these ideas and is defined as

$$f_{\mathrm{H}_2} = \frac{M_{\mathrm{H}_2}}{M_{\mathrm{H,tot}}} \equiv \frac{2\,N_{\mathrm{H}_2}}{N_{\mathrm{H,tot}}}\,, \tag{7.2}$$

where M_{H_2} is the total mass of H_2 and $M_{\mathrm{H,tot}}$ is the total mass of all hydrogen nuclei. The second, equivalent expression is the ratio of the number of H atoms in H_2 molecules ($2\,N_{\mathrm{H}_2}$) and total hydrogen atoms ($N_{\mathrm{H,tot}}$).

AVERAGE H_2 FORMATION TIME

Using the mass of all the H nuclei and the mass of H_2 in the simulation domain, a simple estimate of the average time-scale of H_2 formation (τ_{H_2}) in the simulation can be obtained as

$$\tau_{\mathrm{H}_2} = \frac{M_{\mathrm{H,tot}}}{\dot{M}_{\mathrm{H}_2}}\,, \tag{7.3}$$

where $\dot{M}_{\mathrm{H}_2}$ is the H_2 formation rate that is averaged over 2 Myr for every point.

Figure 14 shows the results of low, intermediate, and high density runs (denoted by the abbreviations – n003, n030, and n300) in the first, second, and third row, respectively. Since the first density inhomogeneities due to the turbulence appear after 1 Myr (see Figure 8), the evolution of the molecular content starting from 2 Myr is shown. The vertical, dashed lines denote that gravity is switched on at $t = 10$ Myr. Note that the TB-R[4-7]-n300 runs evolve only for a short time after 10 Myr due to the reasons mentioned in Chapter 6.

The first column shows the evolution of f_{H_2}, with a maximum value of 1 when 100% of the H atoms are in the form of H_2. In all three setups with different initial densities, the higher resolution runs generally have higher f_{H_2} at any given time. One exception to this is the TB-R6-n003 run, that contains more H_2 than the TB-R7-n003 run after 10 Myr. In the low density runs, only about 20% of the H atoms are in H_2 by the end of the simulation. In the intermediate density runs, the mass fraction gradually increases and reaches $f_{\mathrm{H}_2} \approx 1$ after about 14 Myr of evolution. Note that higher resolution runs reach $f_{\mathrm{H}_2} \approx 1$ faster. The runs with low and intermediate density do not show any significant gravitational effects on the evolution of f_{H_2} for any resolution. The high density runs produce H_2 molecules rather fast. After about 5 Myr of evolution, $f_{\mathrm{H}_2} \approx 1$ is obtained for various resolutions. This is trivial because the molecular content in these high initial density runs saturates and the gas becomes fully molecular regardless of the resolution. The large variation in the evolution of f_{H_2} for different resolutions derives directly from the changing gas morphology, as shown in Figure 12.

The second column shows the evolution of τ_{H_2} for various resolutions along with the theoretical estimate for the equilibrium H_2 formation time-scale $\langle\tau_{H_2,eq}\rangle_{mass}$ (Equation 3.7, mass-weighted mean value) as dashed lines. In all of the low, intermediate, and high density runs, the H_2 formation at all resolutions is faster than $\langle\tau_{H_2,eq}\rangle_{mass}$ before the saturation level is reached. This “faster-than-equilibrium" H_2 formation in turbulent media has been shown by Glover & Mac Low (2007b) and recently noted by Micic et al. (2012), Valdivia et al. (2016), and Seifried et al. (2017). This occurs due to the shorter formation time of H_2 molecules in intermittent high density regions. For the low density runs in the first row, $\tau_{H_2} \to \infty$ when H_2 is being destroyed.

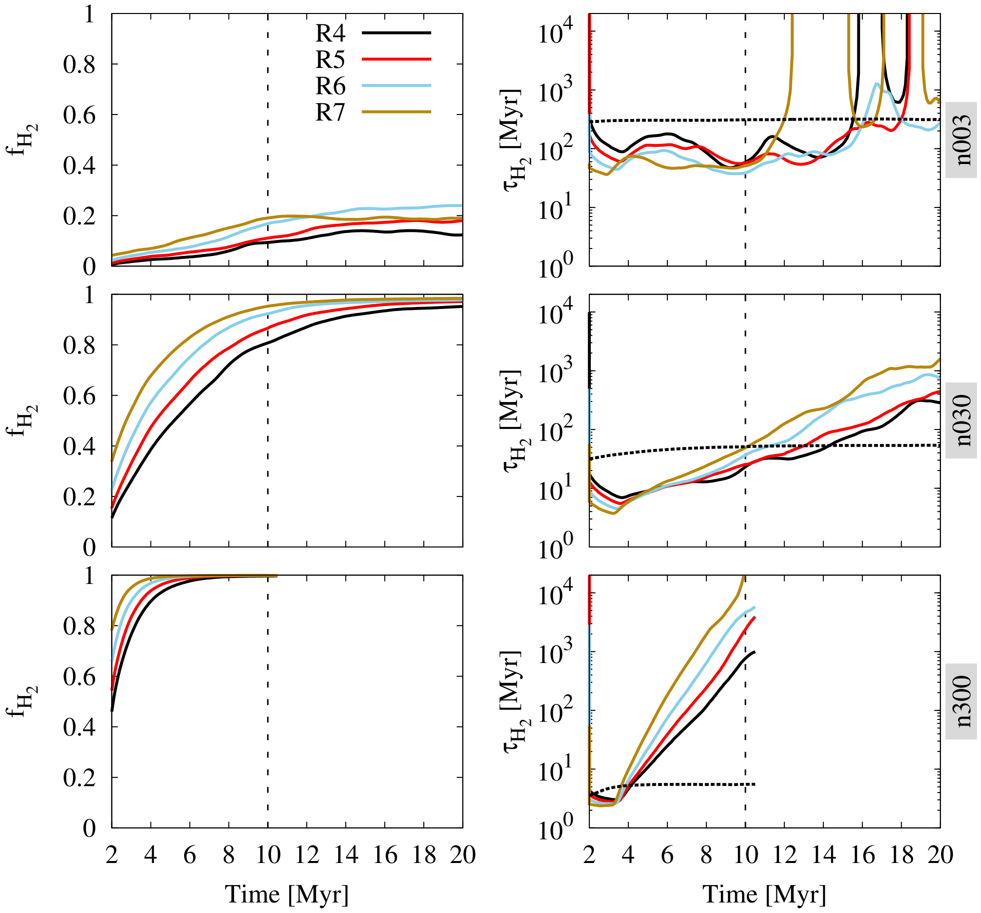

Figure 14: Evolution of H_2 in TB simulations with different resolutions. The vertical, dashed lines separate the time evolution without ($t <$ 10 Myr) and with ($t >$ 10 Myr) self-gravity. Results of different initial conditions are arranged in different rows. The high density runs in the third row are not evolved for long once self-gravity is turned on (see Figure 8). Column 1: the evolution of the H_2 mass fraction (f_{H_2}, Equation 7.2). Column 2: the evolution of the H_2 formation time-scale (τ_{H_2}, Equation 7.3). When H_2 is being destroyed, $\tau_{H_2} \to \infty$. The dashed line is the mass-weighted mean equilibrium H_2 formation time-scale ($\langle\tau_{H_2,eq}\rangle_{mass}$, Equation 3.7).

There is a common trend for the runs in all three rows: after the first density inhomogeneities set in and H_2 formation starts, τ_{H_2} becomes shorter with increasing resolution. Consequently, the saturation level of $f_{\mathrm{H_2}}$ is reached faster for higher resolution runs. After $f_{\mathrm{H_2}}$ reaches the saturation point in the higher resolution runs, however, $\tau_{\mathrm{H_2}}$ becomes longer for higher resolution because the low-resolution runs are still producing H_2. This is less obvious for the low density runs in the first row, but clearly visible in the intermediate and high density runs.

H_2 CONTENT FOR DIFFERENT RESOLUTIONS

So far, the trend of the H_2 evolution with increasing resolution is discussed qualitatively. In order to investigate the convergence of H_2, the run with the highest refinement level, $\mathrm{R_{max}}$, is now taken as a reference simulation. The total mass of H_2 in all simulations are compared with this reference using the ratio

$$\eta_{\mathrm{H_2}} = \frac{f_{\mathrm{H_2}}}{f_{\mathrm{H_2,R_{max}}}}, \tag{7.4}$$

Note that $\eta_{\mathrm{H_2}}$ only reflects the trend of the simulations with increasing resolution, and $\eta_{\mathrm{H_2}} = 1$ is not the expected converged state. However, if $\eta_{\mathrm{H_2}} \sim 1$ is achieved for three or more different resolutions, it can be concluded that the molecule formation is converged.

Figure 14 shows the time evolution of $\eta_{\mathrm{H_2}}$ for all 12 TB runs, for which $R_{\mathrm{max}} = 7$ with $\Delta x = 0.063$ pc. In the low density runs (first row), the TB-R4-n003 and TB-R5-n003 runs produce less H_2 than the TB-R7-n003 run (i.e. $\eta_{\mathrm{H_2}} < 1$), while the TB-R6-n003 run has $\eta_{\mathrm{H_2}} > 1$ shortly after 10 Myr. This occurs due to a gradual destruction of H_2 in the TB-R7-n003 run, as seen in the first row of Figure 14. In the intermediate (second row) and high density runs (third row), $\eta_{\mathrm{H_2}} \leq 1$ for all the lower resolution runs. With increasing resolution, $\eta_{\mathrm{H_2}} \approx 1$ is achieved faster. Although $\eta_{\mathrm{H_2}} \rightarrow 1$ with time in all cases, the evolutionary history of total H_2 is significantly different for the various resolutions. Therefore, the formation of H_2 in runs with resolutions $\Delta x \geq 0.125$ pc is not converged. No conclusion can be drawn for the TB-R7-n[003,030,300] runs due to the absence of reference simulations with higher resolution. Since these simulations with non-equilibrium chemical evolution are computationally expensive (for instance, $\sim 500,000$ CPU-hours for the TB-R7-n030 run), it is currently not possible to go to resolutions as high as achieved in the isothermal TB simulations by Federrath (2013).

7.3 | EVOLUTION OF CO IN TB SETUP

Similar to the results for the formation of H_2, three quantities are calculated to study the formation of CO at different resolutions.

MASS-FRACTION OF CO

The mass fraction of CO is defined as

$$f_{\mathrm{CO}} = \frac{\frac{12}{28} M_{\mathrm{CO}}}{M_{\mathrm{C,tot}}} \equiv \frac{N_{\mathrm{CO}}}{N_{\mathrm{C,tot}}}, \tag{7.5}$$

where $\frac{12}{28} M_{\mathrm{CO}}$ is the total mass of carbon in CO molecules and $M_{\mathrm{C,tot}}$ is the total mass of all the carbon atoms. The equivalent expression is the ratio of the number

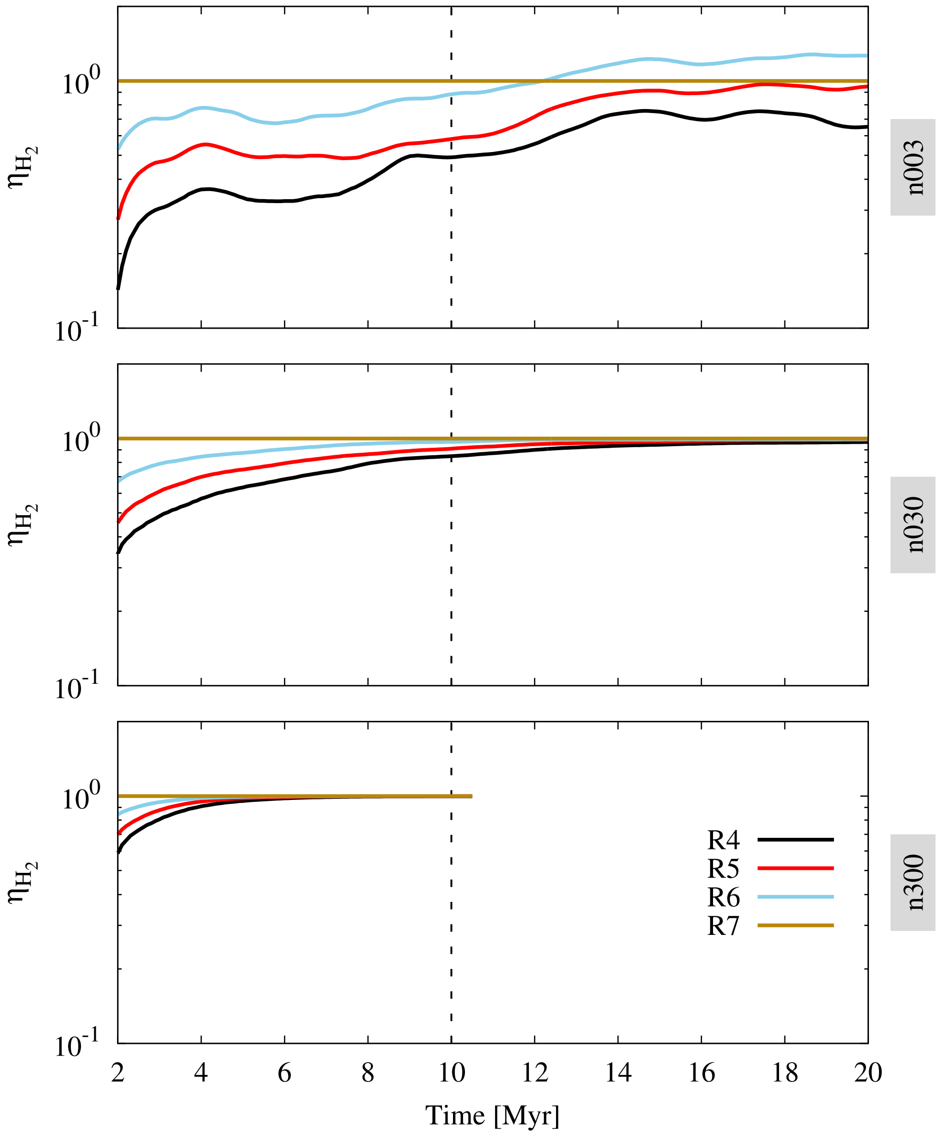

Figure 15: The evolution of η_{H_2} (Equation 7.4) to compare the results for various resolutions, taking the highest resolution run (R7) as a reference. The low, intermediate, and high density runs are arranged in the first, second, and third row, respectively. The runs clearly show that the formation of H_2 is not converged in any of the three sets of simulations.

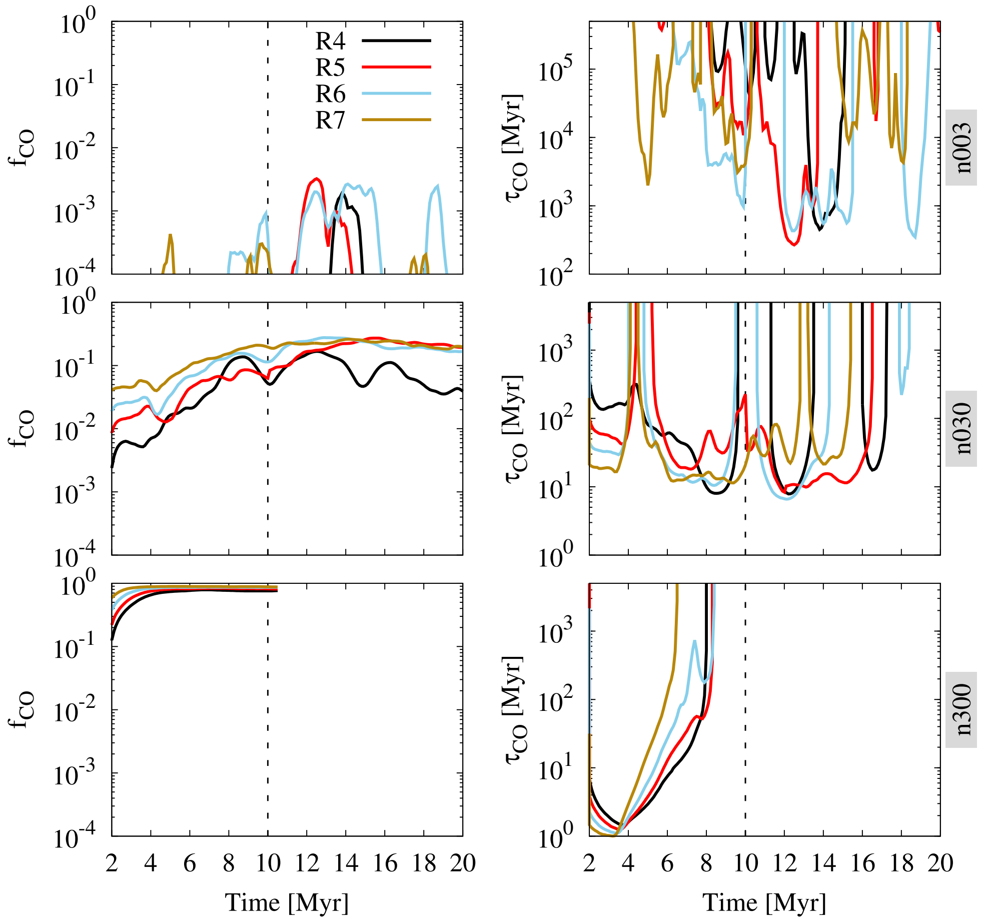

Figure 16: As in Figure 14, now for CO. Column 1: the evolution of the CO mass fraction (f_{CO}, Equation 7.5). Column 2: the evolution of the CO formation time-scale (τ_{CO}, Equation 7.6). In the second column, $\tau_{\text{CO}} \to \infty$ when CO is being destroyed.

of carbon atoms in CO molecules, N_{CO}, to total carbon atoms, $N_{\text{C,tot}}$.

AVERAGE CO FORMATION TIME

The CO formation time-scale in the simulation is defined as

$$\tau_{\text{CO}} = \frac{M_{\text{C,tot}}}{\frac{12}{28}\dot{M}_{\text{CO}}}, \tag{7.6}$$

where $\dot{M}_{\text{CO}}$ is the CO formation rate, that is averaged over 2 Myr for each point. The factor 12/28 corrects for the mass of oxygen.

Figure 16 shows the evolution of f_{CO} in the first column with a maximum value of 1 when 100% of the C atoms are in CO. In the low density runs (first row), there is very little mass contained in the box, the mean density in the turbulent medium is low and any kind of shielding is ineffective, leading to insignificant CO abundances. Nevertheless, the differences with increasing resolution can still be investigated. There is no clear tendency of the changes in CO formation with regard to the resolution. For the intermediate density runs (second row), f_{CO} increases with time and saturates at $f_{\rm CO} \sim 0.2$ (i.e. when 20% of the C atoms are in CO molecules) for the TB-R5-n030, TB-R6-n030, and TB-R7-n030 runs. As the resolution increases, the fluctuations of $f_{\rm CO}$ decrease . Note that the TB-R5-n030, TB-R6-n030, and TB-R7-n030 runs have similar $f_{\rm CO}$ towards the end of the simulation, although their gas distribution is quite different, as shown in Section 6.4. For the high density runs (third row), CO is initially rapidly produced. With increasing resolution, $f_{\rm CO}$ saturates faster and at slightly higher values, similar to H_2 in Figure 14.

The second column shows the evolution of $\tau_{\rm CO}$. Since CO is easily destroyed, multiple instances of $\tau_{\rm CO} \to \infty$ is seen. In the low density runs, the evolution of $\tau_{\rm CO}$ is chaotic since the environment suitable for CO formation is changing rapidly due to the turbulent stirring. In the intermediate density runs, the general trend of $\tau_{\rm CO}$ with increasing resolution is difficult to discern but it lies between 10 and 1000 Myr for the various resolution runs. In the high density runs, $\tau_{\rm CO} < 10$ Myr before the CO content is saturated during the early evolution at $t < 4$ Myr; this corresponds to the rapid initial increase in $f_{\rm CO}$. Notably, $\tau_{\rm CO}$ can occasionally become shorter than $\tau_{\rm H_2}$ during this phase, due to the artificial setup of the cold neutral medium, in which the equilibrium CO formation is found to be shorter than the equilibrium H_2 formation time-scale (Seifried et al. 2017; Gong et al. 2018, and see Section 9.1). Similar to $\tau_{\rm H_2}$, the value of $\tau_{\rm CO}$ is large for higher resolution runs once $f_{\rm CO}$ begins to saturate.

CO CONTENT FOR DIFFERENT RESOLUTIONS

The values of $f_{\rm CO}$ for various resolutions are compared using the ratio

$$\eta_{\rm CO} = \frac{f_{\rm CO}}{f_{\rm CO,R_{max}}} \, . \tag{7.7}$$

Figure 17 shows the time evolution of $\eta_{\rm CO}$ calculated with $\rm R_{max}$ =R7. As expected, there are large, random variations in $\eta_{\rm CO}$ for the low density runs (row 1). In the intermediate density runs (row 2), $\eta_{\rm CO} \to 1$ with time for the TB-R5-n030 and TB-R6-n030 simulations, while the TB-R4-n030 run shows a large offset. The high density runs (row 3) show that the large initial differences quickly settle down once $f_{\rm CO}$ saturates and the $\eta_{\rm CO} \approx 1$ at all resolutions towards the end of the runs. Again, similar to the H_2 formation, the formation of CO in runs with resolutions $\Delta x \geq 0.125$ pc is not converged.

7.4 | DENSITY DISTRIBUTION

The effective formation of CO molecules occurs in the dense regions which are reasonably well-shielded from external radiation. Thus, it is necessary to probe the mass-weighted density distribution at various resolutions. The mass contribution in the $i^{\rm th}$ density bin of the probability density function (PDF) is calculated as

$$M_i = \sum_{j=1}^{\rm N_{cells,\it i}} \rho_j V_j \, , \tag{7.8}$$

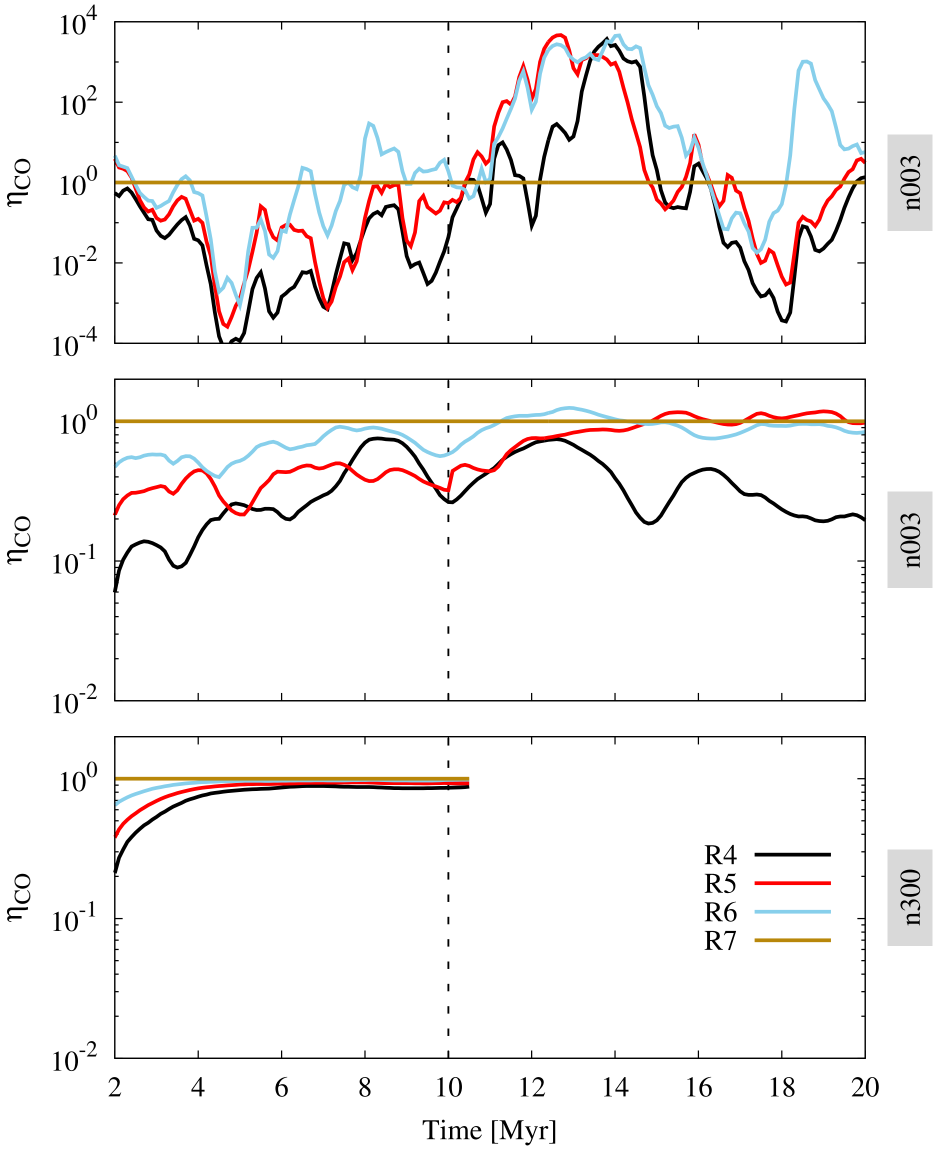

Figure 17: The evolution of η_{CO} (Equation 7.7). Similar to the results for H_2, the formation of CO is also not converged in all three sets of simulations.

where ρ_j and V_j are the density and volume of the j^{th} cell, respectively, and $\mathrm{N}_{\mathrm{cells},i}$ are all cells in the computational domain with density ρ such that

$$\log \rho \in [\log \rho_i, \log \rho_i + d(\log \rho_i)[\ , \tag{7.9}$$

where $d(\log \rho_i)$ is the bin size. Then, the mass-weighted density PDF, P_ρ, for every density bin i is calculated as

$$P_{\rho,i} = \frac{M_i}{M_{\mathrm{tot}}} \, , \tag{7.10}$$

where M_{tot} is the total mass in the simulation.

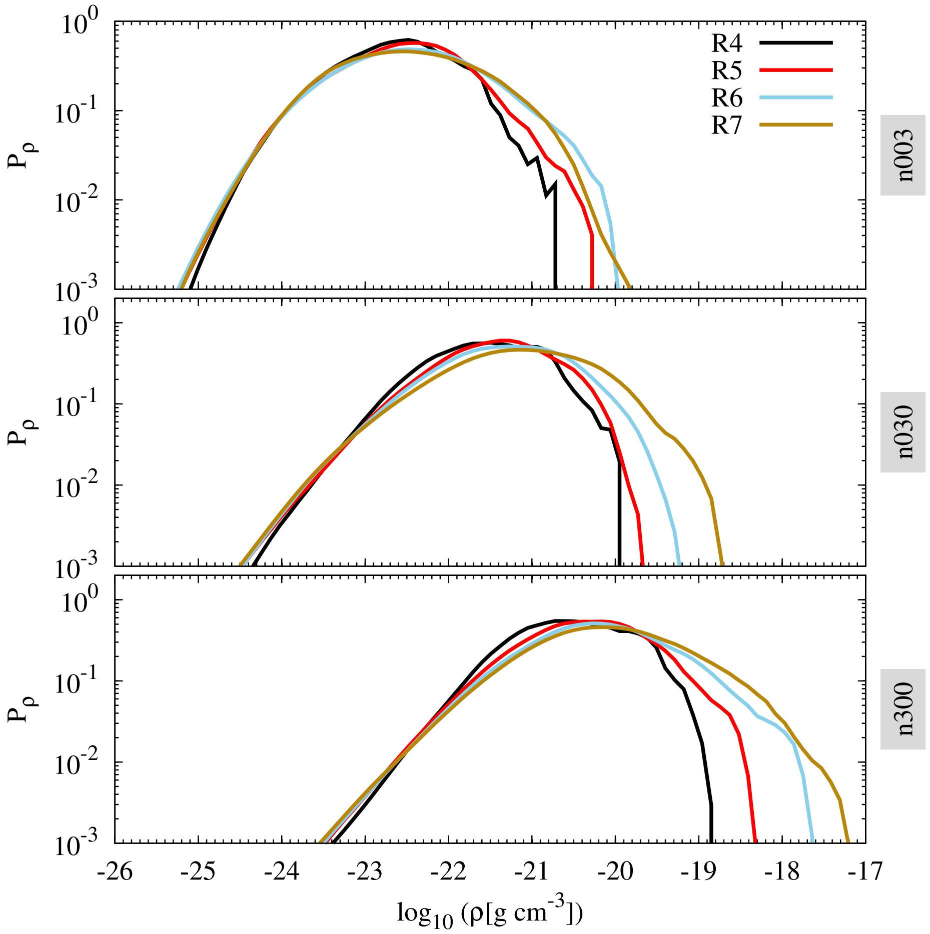

Figure 18: Mass-weighted PDFs (Equation 7.10) of the gas density for the TB simulations with various resolutions. The distributions are averaged from five simulation snapshots between $t = 9.5$ Myr and 10 Myr. Low, intermediate and high density runs are shown from top to bottom. The density distributions are not converged in all three density regimes.

Figure 18 shows the density-PDFs of the 12 TB runs. The distributions are averaged from five simulation snapshots between $t = 9.5$ Myr and 10 Myr, i.e. before gravity is activated. Hence, the PDFs display the density distributions in a medium with well-developed turbulence. The PDFs of low, intermediate, and high density runs are arranged from top to bottom. In all runs, the maximum density increases by a factor of 2 to 3 for each higher resolution. The low density tail is similar for all resolutions but the peak of the distribution as well as the high density tail of runs with different resolutions show significant differences. Thus, the mass-weighted distribution of the gas density is also not converged for the simulations with $\Delta x \geq 0.125$ pc (R7).

7.5 | CHAPTER SUMMARY

In this chapter, the effects of simulation resolution on the column density projections of the gas (and its chemical components), the evolution of total H_2 and CO content, and the PDF of gas-density were investigated in the turbulent box setup. The evolution of molecular gas from three different sets of initial conditions were considered in simulations with spatial resolutions ranging from $\Delta x = 0.5$ pc to $\Delta x = 0.063$ pc. A converged evolution of the total H_2 and CO content was not obtained.

8 | Chemical Evolution in CF simulations

NOTE

This chapter is an adaption of the paper “On the resolution requirements for modelling molecular gas formation in solar neighbourhood conditions" (Joshi et al. 2019).

In this chapter, the detailed results of the colliding flows simulations are presented. The results are structured in the same manner as the results of turbulent box simulations in Chapter 7. Unlike the TB simulations, where the total gas mass in the simulation domain is constant, gas is constantly accreting in the MC forming region in the CF simulations. Hence, the chapter starts with the evolution of the mass of the total gas, H_2, and CO in the CF simulation with highest resolution (CF-R10) in order to provide an insight into the gas accretion process. Then, the effect of the choice of the collision interface on molecule formation is discussed. This is followed by the column densities, the evolution of the total H_2 and CO content, and the gas density distribution at different resolutions. The stream of stable WNM is chemically unimportant and is excluded from all analyses; only the gas with $T < 4000$ K is considered.

Figure 19 shows the time evolution of the mass of total gas, H_2 and CO in the CF-R10 simulation with an effective resolution of $\Delta x = 0.008$ pc. The CO mass is scaled by α_C (see Equation 7.1) for easier comparison with the mass of the total gas and H_2 in the same y-axis range. After about 1 Myr, the shocked gas at the collision interface starts to cool and rapid H_2 formation sets in. At the end of the simulation, $\sim 5 \times 10^3\,M_\odot$ of H_2 has formed, which is about 30% of the total mass. When the rapid H_2 formation slows down after $\sim$ 10% of the gas mass is in H_2, the formation of CO starts. A significant amount of CO is produced only after 14 Myr. At the end of the simulation, about 3 $M_\odot$ of CO has formed, which accounts for $\sim$ 15% of the total mass in carbon atoms.

8.1 | THE CHOICE OF THE COLLISION INTERFACE

Figure 20 shows the H_2 and CO content developing in the CF simulations up to 15 Myr for 9 different interfaces introduced in Section 5.2 (see Figure 6). The inter-

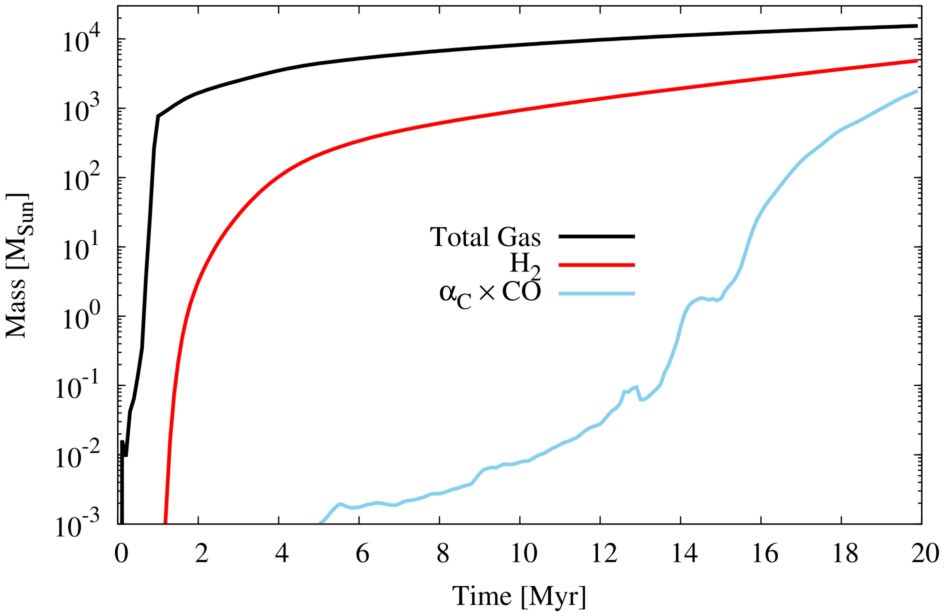

Figure 19: Time evolution of the total, H_2, and CO mass in the CF-R10 run. Note that only the gas with $T < 4000$ K is considered. The CO mass is scaled by α_C (see Equation 7.1) in order to visually compare the formation of CO with H_2.

faces with large, homogeneous sub-structures (I1, I2 and I3) do not provide a lot of surface area for the opposite flows to interact. As a result, gas is easily collected in homogeneous “pockets" and much more H_2 and CO is produced due to more effective shielding. In all other interfaces that lead to more sub-structure, the molecular content is systematically smaller. Interfaces I5a, I5, and I5b are obtained by changing the amplitude ($A = 1$ pc, 1.6 pc, and 2 pc, respectively) in Equation 5.2, while all other parameters are fixed; the slice of the collision interface at the $x = 0$ plane in Figure 6 is identical for all three cases. Figure 20 shows that the molecular content changes slightly with the change in A. The interface I5 (solid black line) results in an intermediate amount of molecular gas and is chosen for all other CF simulations in this thesis.

8.2 | COLUMN DENSITY DISTRIBUTION

Figure 21 shows the column density of the total gas and the two hydrogen-species – H and H_2 (from top to bottom) at $t = 20$ Myr. Out of the seven different resolution runs, four selected runs with the resolution increasing from left to right, are displayed. The maps are produced by integrating along the direction of the stream of the colliding WNM (x–axis). As the resolution gradually increases in the CF-R4, CF-R5, and CF-R6 runs, the total gas column density shows a significant change in the structure of both the diffuse and the dense gas. The CF-R6 run and the highest resolution run (CF-R10) have similar gas distributions except for the most dense regions. In general, the low resolution runs (CF-R4, CF-R5) harbour clumpy

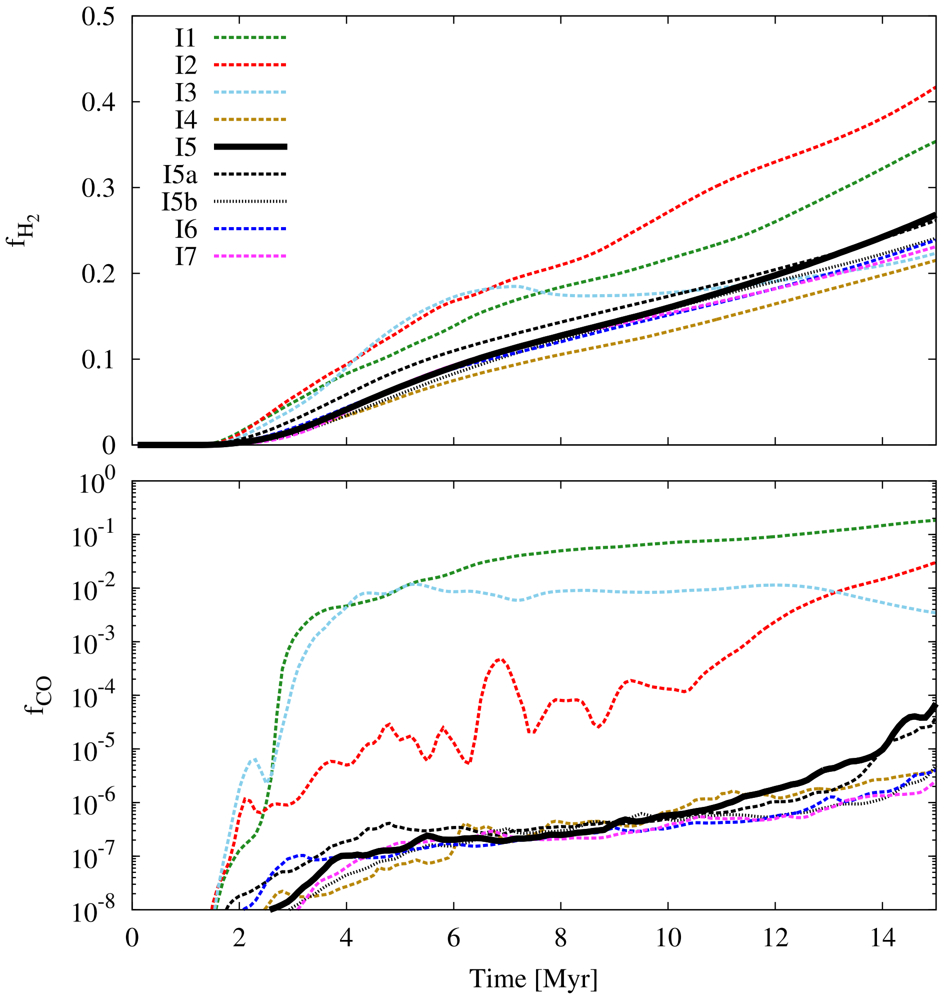

Figure 20: Time evolution of the mass fraction of H_2 (top) and CO (bottom) for the different interfaces shown in Figure 6. The mass fractions f_{H_2} and f_{CO} are defined in Equations 7.2 and 7.5, respectively. The solid black line shows interface I5, which is used for the study of MC evolution in CF setup.

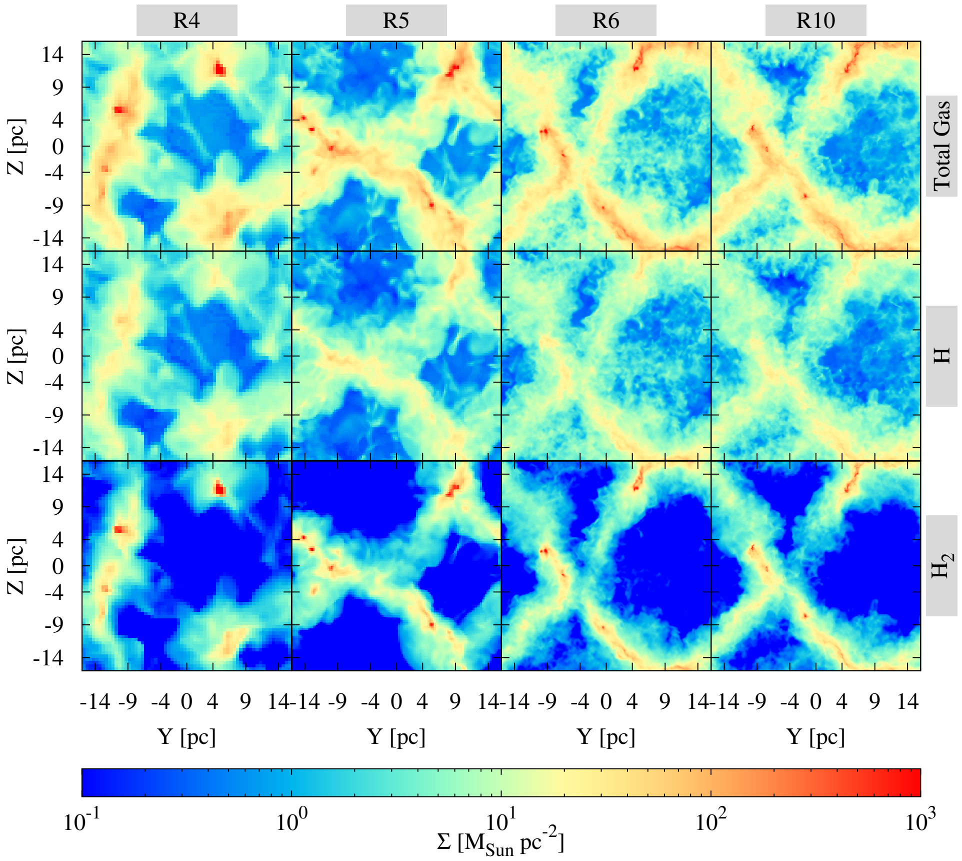

Figure 21: Column density distributions of the total gas, H, and H_2 (from top to bottom) at $t = 20$ Myr for the CF-R[4,5,6,10] runs (left to right). The column density is computed by considering only the gas with $T < 4000$ K and integrating along the x–axis (i.e. the direction of the colliding flow). In the CF-R[4,5,6] runs, the column density distribution is significantly different with increasing resolution. The CF-R6 and CF-R10 runs have similar distributions, except for the dense regions.

and spatially separated high column density regions; in contrast, the higher resolution runs (CF-R[6-10]) produce a network of filaments with compact cores. The H column density in the second row shows the diffuse gas distribution that surrounds the denser H_2 regions.

Figure 22 shows the comparison of the column densities of carbon-species – C^+ (first row), C (second row), and CO (third row) – with the same layout and color-scale as in Figure 21. The column densities of C^+, C and CO are again scaled by α_C to make the carbon content visible on the same color-scale. A diffuse C^+ distribution is seen throughout the simulation domain, similar to the distribution of H in Figure 21. The low and extended column density of atomic carbon is found in the H_2-rich regions and show faint filamentary structures. The fairly isolated CO-rich regions are found in high H_2 column density regions and are surrounded by the atomic carbon column densities.

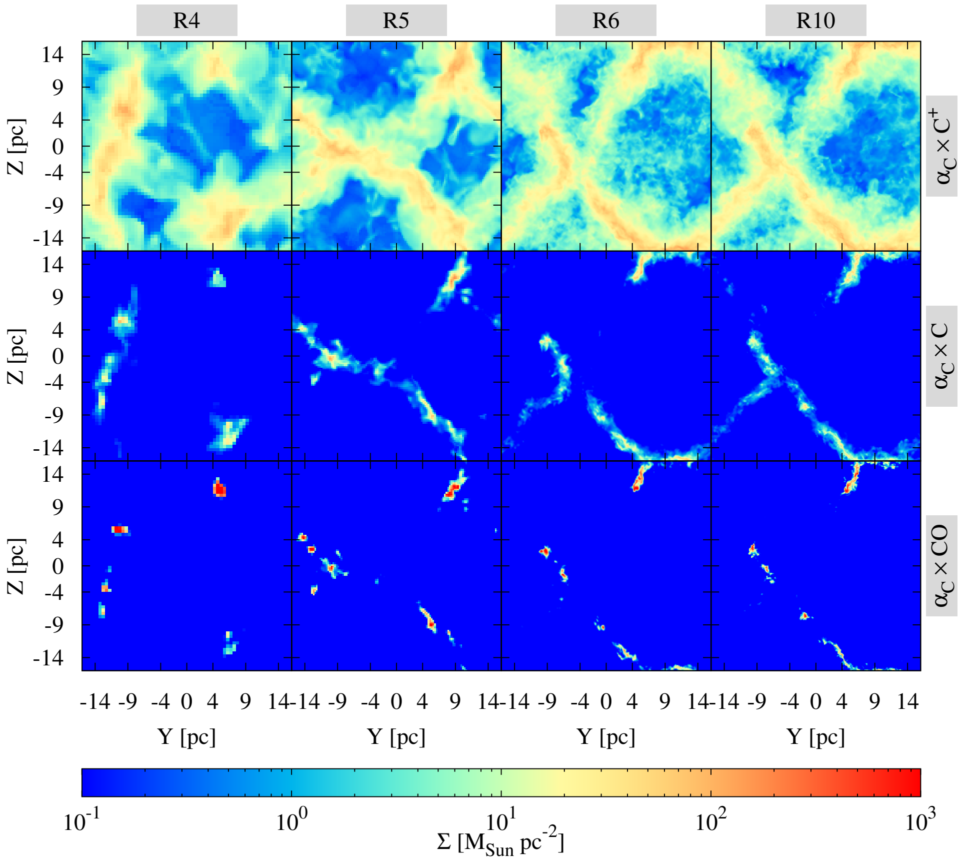

Figure 22: As in Figure 22, now for the carbon species – C^+, C, and CO (from top to bottom). The maps are scaled by α_C (see Equation 7.1) for direct comparison with the column density maps in Figure 22. Compared to C^+, the column density of C and CO are more sensitive to the resolution of the simulation.

8.3 | EVOLUTION OF H_2 IN CF SETUP

The left column of Figure 23 shows the evolution of H_2 in the CF runs. Similar to the results of the TB runs, the evolution of the molecular content is shown starting from 2 Myr. The top panel shows the evolution of f_{H_2} (Equation 7.2). About 40% of H atoms are found in H_2 towards the end of the simulations. Compared to the higher resolution runs, the CF-R4 and CF-R5 runs have lower f_{H_2} before 10 Myr and then higher f_{H_2} towards the end of the simulation. The values of f_{H_2} in CF-R6 and higher resolution runs are similar.

The middle panel shows the evolution of τ_{H_2} (Equation 7.3). The dashed line depicts the equilibrium H_2 formation time scale $\langle\tau_{H_2,eq}\rangle_{mass}$ given by Equation 3.7. After the rapid H_2 formation phase (i.e. $t < 6$ Myr), τ_{H_2} is always shorter than $\langle\tau_{H_2,eq}\rangle_{mass}$. As the mean density of the MC forming gas gradually increases with time, τ_{H_2} decreases to < 20 Myr towards the end of the simulation. Particularly interesting is the fact that the CF-R4 and CF-R5 runs have longer τ_{H_2} than the other runs during the early evolutionary phase, but have shorter τ_{H_2} after $t \sim 10$ Myr. Since a similar scenario is observed for the evolution of CO, this phenomena is discussed together for H_2 and CO later in the chapter. There are only minor differences

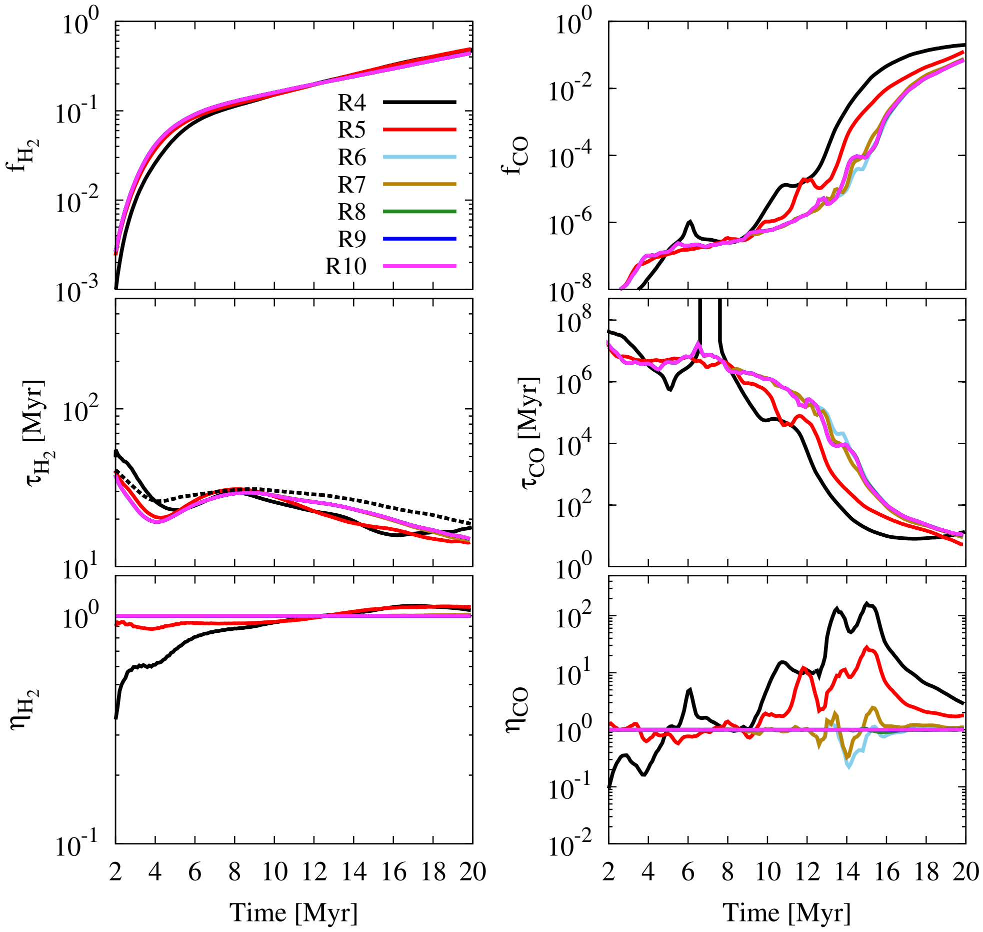

Figure 23: Time evolution of the molecular gas mass-fraction (top), formation time-scale (middle), and η with respect to the highest resolution run CF-R10 (bottom) for H_2 (left column) and CO (right column) in the CF setup. The dashed line in the middle-left panel shows the equilibrium H_2 formation time scale (see Equation 3.7). The H_2 formation is converged for refinement level 6 with $\Delta x = 0.125$ pc (CF-R6) and higher. The CO formation is converged for refinement level 8 (CF-R8 simulation with $\Delta x = 0.032$ pc) and higher.

in the evolution of τ_{H_2} for the other high resolution runs (CF-R[6,7,8,9,10]).

The bottom panel shows the time evolution of η_{H_2} (Equation 7.4) in order to compare f_{H_2} in the runs with various resolutions. Here, the reference simulation is CF-R10 with $R_{max} = R10$, corresponding to an effective resolution of $\Delta x = 0.008$ pc. The CF-R4 and CF-R5 runs have $\eta_{H_2} < 1$ at early times but eventually exceed the amount of H_2 produced by the higher resolution runs ($\eta_{H_2} > 1$) towards the end of the simulation. There is no significant difference in f_{H_2} between the other higher resolution runs.

Overall, the H_2 formation is not sensitive to the (Jeans-)refinement of the dense regions; the total H_2 abundance and average H_2 formation time-scale are converged for an effective resolution of $\Delta x = 0.125$ pc (CF-R6) and higher. This is in agreement with the required resolution for H_2 chemistry as noted by Glover et al. (2010);

Micic et al. (2012); Valdivia et al. (2016) and Seifried et al. (2017). A theoretical background developed to explain this resolution requirement is presented in Chapter 9.

8.4 | EVOLUTION OF CO IN CF SETUP

The right column of Figure 23 shows the evolution of CO in the CF runs. The top panel shows the evolution of $f_{\rm CO}$ (Equation 7.5). The CF-R4 run generally has lower $f_{\rm CO}$ than the other higher resolution runs in the beginning. With time, $f_{\rm CO}$ becomes significantly larger for the low resolution CF-R4 and CF-R5 runs. The spikes in H_2 formation (and subsequent destruction) seen in the low resolution runs (e.g. in CF-R4 at $t = 6$ Myr or in CF-R5 at $t = 12$ Myr) are absent in higher resolution runs. Between $t = 12$ and 16 Myr, the CF-R6 and CF-R7 runs show some deviation in $f_{\rm CO}$ from the higher resolution runs.

The middle panel shows the evolution of $\tau_{\rm CO}$ (Equation 7.6). The CF-R4 run shows $\tau_{\rm CO} \rightarrow \infty$ when a significant amount of CO is gradually destroyed for more than 2 Myr after $t \sim 6$ Myr. The CO formation time-scale is extremely long before 10 Myr. Afterwards, the CF-R4 and CF-R5 runs have a shorter $\tau_{\rm CO,form}$ than the higher resolution runs. With time, the differences in $\tau_{\rm CO,form}$ at various resolutions become smaller and all the runs have an average CO formation time of about 10 Myr towards the end of the simulations.

The bottom panel shows the time evolution of $\eta_{\rm CO}$ (Equation 7.7, with $\rm R_{max}$ =R10). Before 5 Myr, the CF-R4 and CF-R5 runs have $\eta_{\rm CO} < 1$, but they quickly produce as much CO as the CF-R10 run. After 10 Myr, $\eta_{\rm CO} \gg 1$ for the CF-R4 and CF-R5 runs. With increasing resolution, the deviation from the reference value decreases. The runs CF-R6 and CF-R7 show fluctuations with $0.2 < \eta_{\rm CO} < 2$ and only the CF-R8 and CF-R9 runs show $\eta_{\rm CO} \approx 1$. Hence, the sub-structure of small, dense regions significantly affects the CO formation; the total CO abundance and the average CO formation time-scale are converged for an effective resolution of $\Delta x = 0.032$ pc (CF-R8) and higher.

HIGHER MOLECULAR CONTENT IN LOW RESOLUTION SIMULATIONS

The formation of a higher amount of H_2 and CO in lower resolution simulations is explained by the distribution of the visual extinction, $A_{\rm V}$, experienced by the cells in the simulation, shown in Figure 24. For each cell, $A_{\rm V}$ is the average value over the 48 HEALPIX pixels, computed by the OPTICALDEPTH module (see Section 4.4). The top panel shows the $A_{\rm V}$-PDF at $t = 5$ Myr and the bottom panel at $t = 20$ Myr, when both H_2 and CO are being produced rapidly. It is clearly seen that the mass of well-shielded gas ($0.1 < A_{\rm V} < 1$) is similar at early times; however, at $t = 20$ Myr, the shielding in lower resolution runs (CF-R4 and CF-R5) has become more effective than in the higher resolution runs. Indeed, the column densities of the CF runs in Figure 21 show that a coarser resolution produces large, clumpy structures. Such a gas configuration eventually leads to higher shielding of the gas within, resulting in a more effective molecule formation. As more molecules form, the non-linear effects due to (self–)shielding and density further increase the molecular content of the cold gas.

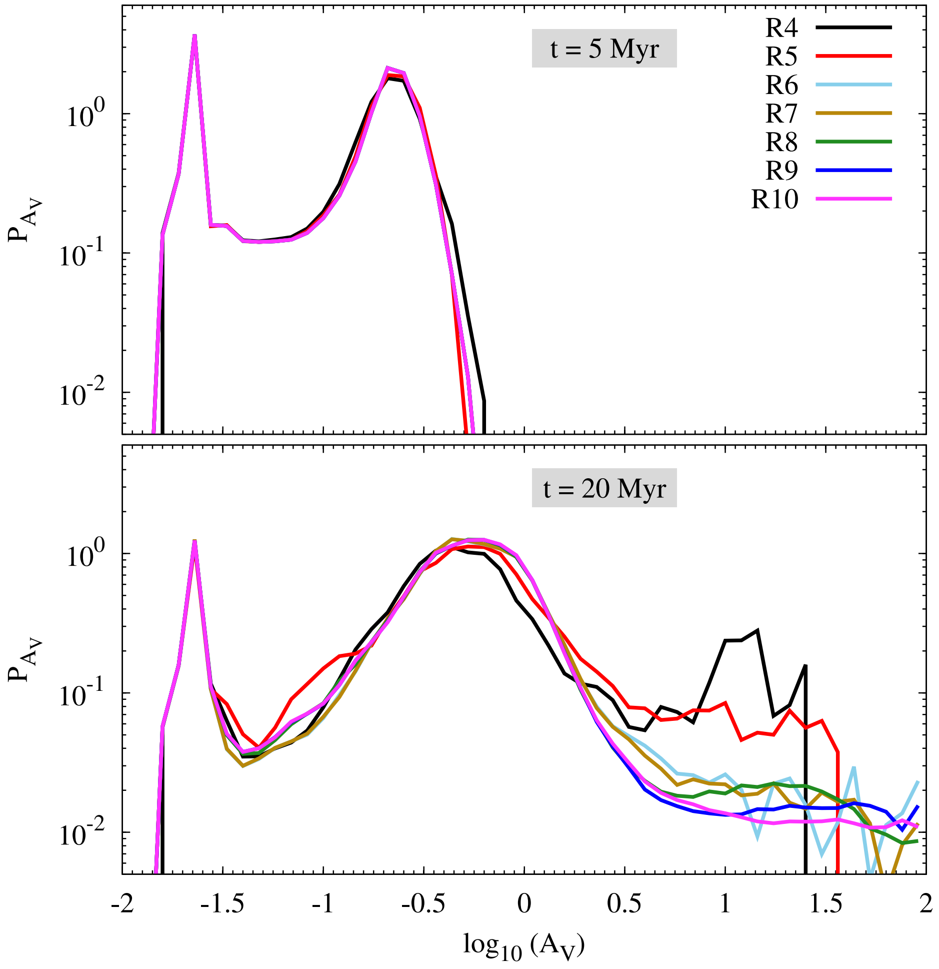

Figure 24: The mass-weighted A_V-PDFs of the CF runs with different resolutions. Top: at time $t = 5$ Myr, bottom: at $t = 20$ Myr. Lower resolution runs eventually produce more gas with $A_V > 1$ and hence more molecular gas.

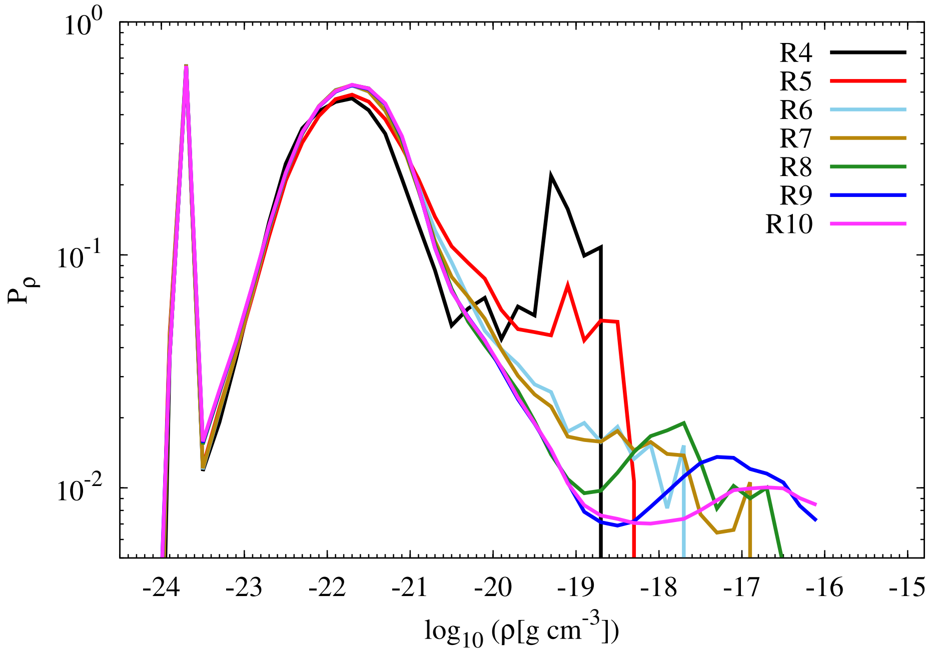

Figure 25: Mass-weighted density PDFs (Equation 7.10) of the CF runs with various resolutions. The distributions are averaged from 5 simulation snapshots between $t = 19.5$ Myr and 20 Myr. The high density tails show significant differences with increasing resolution and the density at which the distributions deviate from one another increases with increasing resolution.

8.5 | DENSITY DISTRIBUTION

Figure 25 shows the mass-weighted density PDFs (Equation 7.10) of the CF simulations with various resolutions. The distributions are averaged from five simulation snapshots between $t = 19.5$ Myr and 20 Myr. The spike at low density ($\rho \sim 10^{-24}$ g cm^{-3}) belongs to the incoming warm gas that begins to cool below 4000 K near the collision interface. The distribution of the gas below the density of $\rho \sim 10^{-22}$ g cm^{-3} (peak of the distribution) is similar for all the resolutions. The high density tails in Figure 25 clearly show the effect of resolution on the distribution of gas. With increasing resolution, the density structures of interest – i.e. shocks or gravitating regions – are better resolved and higher densities are obtained. This occurs because the gas is collected in relatively large cells in a low resolution run, whereas the same gas is compressed into smaller sub-structures for higher resolution runs. It is also apparent that the density at which the PDFs start to deviate from one another increases with increasing resolution. This influences the convergence of the molecular gas formation in the simulations and is discussed in detail in the next chapter.

8.6 | CHAPTER SUMMARY

In this chapter, the effects of simulation resolution on the column density projections of the gas (and its chemical components), the evolution of total H_2 and CO content, and the PDFs of visual extinction A_V and gas-density were investigated in the colliding flow setup. Spatial resolutions ranging from $\Delta x = 0.5$ pc to $\Delta x = 0.008$ pc were considered. Even for the relatively quiescent environment modelled in the CF setup, the converged evolution of the total H_2 and CO content were obtained for a high resolution of $\Delta x = 0.125$ pc and $\Delta x = 0.032$ pc, respectively.

9 | Resolution criteria to model molecule formation

NOTE

This chapter contains sections some of which are part of the paper “On the resolution requirements for modelling molecular gas formation in solar neighbourhood conditions" (Joshi et al. 2019).

The previous two chapters indicate that the resolution required to obtain a converged molecule formation in numerical modelling depends on the physical properties of the gas in the simulation. The molecule formation is converged only in the CF simulations. In addition, the H_2 and CO formation in the same simulation setup do not show convergence at the same resolution. Qualitatively, the required spatial resolution for converged H_2 formation in multiple chemical networks has been shown to be $\Delta x_{H_2,\text{form}} \sim 0.1$ pc by Glover et al. (2010), Micic et al. (2012), Valdivia et al. (2016), and Seifried et al. (2017); the CF runs agree with this requirement. A theoretical foundation to explain such a resolution requirement is, however, still missing.

There are three important time-scales that should be considered to understand the chemical evolution of the gas in numerical models – the molecule formation time ($\tau_{\text{mol,form}}$), the molecule dissociation time ($\tau_{\text{mol,dissoc}}$), and the local cell-crossing time ($t_{\text{cell,cross}}$) of the gas. In this chapter, the relations between these time-scales are investigated to introduce two conditions that are relevant for a converged formation of any given molecule in a simulation.

Section 9.1 describes the **physical condition** that arises from the molecule formation and dissociation times; it deals with whether molecules are being formed or destroyed in general. Section 9.2 describes the **dynamical condition** that arises from the molecule formation time and the cell-crossing times; it deals with how the molecule formation in a cell is affected by the dynamics of the gas. Each condition results in a density criterion, indicating which densities need to be resolved by simulation. In Sections 9.3 and 9.4, the two conditions are applied to the molecule forming gas in the CF and TB runs, respectively. The required density criteria are identified and the derived resolution requirements are compared with the numerical results presented in Chapters 7 and 8.

9.1 | CONDITION 1: PHYSICAL CONDITION

The first condition is a relation between two physical time-scales, which is given by

$$\tau_{\mathrm{mol,form}} \leq \tau_{\mathrm{mol,dissoc}}\,, \tag{9.1}$$

such that effective molecule formation is possible. If a simulation is not able to resolve the minimum density at which this physical condition is satisfied, then the qualitative correctness of the molecule formation is questionable; i.e. regions that should contain molecular gas are not likely to have any molecules. For the simulations presented in this thesis, the physical condition is investigated via the limiting reactions for H_2 and CO evolution in the NL99 chemistry network.

H_2 MOLECULE

The H_2 formation occurs predominantly on the surface of dust grains via the reaction

$$\mathrm{H} + \mathrm{H(s)} \longrightarrow \mathrm{H_2}\,, \tag{9.2}$$

with the H_2 formation time-scale $\tau_{\mathrm{H_2,form}}$ given by Equation 3.8. Photo-dissociation is the main destruction mechanism of H_2 molecules via the reaction

$$\mathrm{H_2} + \gamma \longrightarrow \mathrm{H} + \mathrm{H}\,, \tag{9.3}$$

with the photo-dissociation rate given by Equation 4.13; the corresponding H_2 dissociation time-scale is

$$\begin{aligned} \tau_{\mathrm{H_2,dissoc}} &= 1/R_{\mathrm{pd,H_2}} \\ &= \frac{1}{3.3\times10^{-11}\ \mathrm{s^{-1}}\,G_0}\,\frac{1}{f_{\mathrm{shield,H_2}}}\exp(3.5A_{\mathrm{V}})\,, \end{aligned} \tag{9.4}$$

Thus, the H_2 formation time (Equation 3.8) depends linearly on the factor $1/n$, where n is the gas density. On the other hand, the H_2 dissociation time (Equation 9.4) depends on the strength of the incident radiation field and the shielding of the ISRF by the inhomogeneous distribution of dust and H_2 molecules around the fluid element. Therefore, the density criterion given by the physical condition for H_2 depends on the physical properties of the gas in the simulation. For instance, the dissociation time is shorter in environments with higher G_0 (e.g. near star-forming regions); as a result, the density required to fulfill the physical condition is higher in such regions.

CO MOLECULE

The shielding of CO by H_2 is important for CO formation. Therefore, effective CO formation sets in only when enough H_2 is formed (Glover et al. 2010, see also Figure 19) and hence the formation of H_2 on dust grains is a limiting reaction for CO formation. In addition, the formation of CH_2^+ via the reactions

$$
\begin{aligned}
&C^+ + H_2 \longrightarrow CH_2^+ + \gamma\,, && (9.5)\\
&C + H_3^+ \longrightarrow CH_2^+ + H\,, && (9.6)\\
&H_2 + \text{cosmic-ray} \longrightarrow H_2^+ + e^-\,, && (9.7)\\
&H_3^+ + e^- \longrightarrow H_2 + H\,, && (9.8)
\end{aligned}
$$

have been identified as the limiting reactions for CO formation (see Section 3.3). The net CO formation time $\tau_{\rm CO,form}$ is given by Equation 3.27. When the cosmic ray ionization rate is moderate ($\lesssim 10^{-15}\ {\rm s}^{-1}$, Bisbas et al. 2015) and the X-ray energy density is low ($\lesssim 10^{-12}\ {\rm erg\ cm}^{-3}$, Mackey et al. 2018), the CO molecules are destroyed mostly by photo-dissociation via the reaction

$$
CO + \gamma \longrightarrow C + O\,, \tag{9.9}
$$

with the CO photo-dissociation rate given by Equation 4.15; the corresponding CO dissociation time-scale is $\tau_{\rm CO,dissoc} = 1/R_{\rm pd,CO}$.

$$
\begin{aligned}
\tau_{\rm CO,dissoc} &= 1/R_{\rm pd,CO}\\
&= \frac{1}{1.235\times 10^{-10}\ {\rm s}^{-1}\ G_0}\ \frac{1}{f_{\rm shield,CO}}\ \exp(2.5A_{\rm V})\,,
\end{aligned} \tag{9.10}
$$

Therefore, the CO formation time (Equation 3.27) also depends linearly on the factor $1/n$, although the relation is not as trivial as for H_2. Similarly, the CO dissociation rate depends on the strength of the incident radiation field and the shielding of the ISRF by the inhomogeneous distribution of dust, H_2, and CO molecules around the fluid element.

9.2 | CONDITION 2: DYNAMICAL CONDITION

The second condition is a relation between the physical and numerical time-scale, which is given by

$$
\tau_{\rm mol,form} \leq t_{\rm cell,cross}\,. \tag{9.11}
$$

Cells that fulfill the dynamical condition become fully molecular within one cell-crossing time regardless of the physical properties of the gas. The molecule formation in cells that do not satisfy Equation 9.11 is susceptible to even the small dynamical changes in the non-linear evolution of the turbulent gas; it is important that such cells are free from numerical artefacts. Therefore, a simulation should be able to resolve the minimum density at which $\tau_{\rm mol,form} = t_{\rm cell,cross}$.

It is evident that the physical condition in Equation 9.1 is a necessary but not a sufficient condition for converged molecule formation. Suppose the dynamical condition gives a stronger density criterion for a certain molecule. If a simulation resolves the typical densities that are high enough to satisfy the physical condition but too low to satisfy the dynamical condition, then the molecule formation may be qualitatively correct, but quantitatively incorrect. In other words, the simulation will correctly predict that the gas in a certain region should be molecular, but might get the molecular fraction or the time to reach the equilibrium wrong.

The local (M)HD time step (Δt) given by Equation 4.17 provides the lower limit of the cell-crossing time ($t_{\text{cell,cross}}$) in a simulation. Equating $t_{\text{cell,cross}}$ to Δt, which is calculated from the velocity of individual cells, is a conservative estimate. The reason is that the chemical abundances are advected with the flow and therefore large advection velocities do not change the density distribution of the gas. Since molecule formation occurs in dense and turbulent gas, it is intuitive to take the mass-weighted mean velocity dispersion $\langle\sigma\rangle_{\text{mass}}$ of such dense gas as an estimate for the typical velocity in molecule forming gas. This results in the typical cell-crossing time of the gas, defined as

$$t_{\text{cell,cross}} = \frac{\Delta x}{\langle\sigma\rangle_{\text{mass}}} . \tag{9.12}$$

The formation time of molecules ($\tau_{\text{mol,form}}$) is proportional to $1/n$, as described above in Section 9.1. Therefore, the minimum density at which the dynamical condition is fulfilled ($n_{\text{dyn,min}}$) is given by

$$\begin{aligned} & \tau_{\text{mol,form}} = t_{\text{cell,cross}} , \\ \longrightarrow \quad & n_{\text{dyn,min}} \propto \frac{\langle\sigma\rangle_{\text{mass}}}{\Delta x} \end{aligned} \tag{9.13}$$

The dynamical condition requires that a simulation resolves all densities $n < n_{\text{dyn,min}}$. As the resolution of a simulation increases, the cells in shocked or gravitating regions are better resolved, allowing the formation of denser regions. The column density maps and density PDFs in previous chapters demonstrate this for all the simulations performed in this study. In simulations with self-gravitating gas, densities higher than the Jeans density (Jeans 1902) corresponding to the spatial resolution will produce artificial fragmentation in the gas (Truelove et al. 1997). Therefore, the maximum density resolved by the simulation is

$$\rho_{\text{Jeans}} = \frac{\pi c_{\text{s}}^2}{\lambda_{\text{J}}^2 G} , \tag{9.14}$$

where $\lambda_{\text{J}} = N_{\text{J}}\,\Delta x$ is the Jeans length resolved with N_{J} cells (see Section 4.7), G is the gravitational constant, and the isothermal sound speed c_{s} in the dense molecule-forming regions is given by Equation 2.4. Thus, the relation between the number density n and the spatial resolution Δx for a simulation is

$$n_{\text{Jeans}} = \frac{\rho_{\text{Jeans}}}{\mu\, m_{\text{p}}} = \frac{\pi k_{\text{B}} T}{(\mu\, m_{\text{p}}\, N_{\text{J}}\, \Delta x)^2 G} , \tag{9.15}$$

$$\longrightarrow \quad n_{\text{Jeans}} \propto \frac{1}{(\Delta x)^2} \tag{9.16}$$

Therefore, for the molecule formation in TB and CF runs, the minimum density satisfying the dynamical condition $n_{\text{dyn,min}}$ (Equation 9.13) and the maximum density resolved by the simulation n_{Jeans} (Equation 9.16) scale differently with the resolution Δx. The sketch in Figure 26 shows how the low resolution simulations (in the white region) are not able to resolve the minimum density required by the dy-

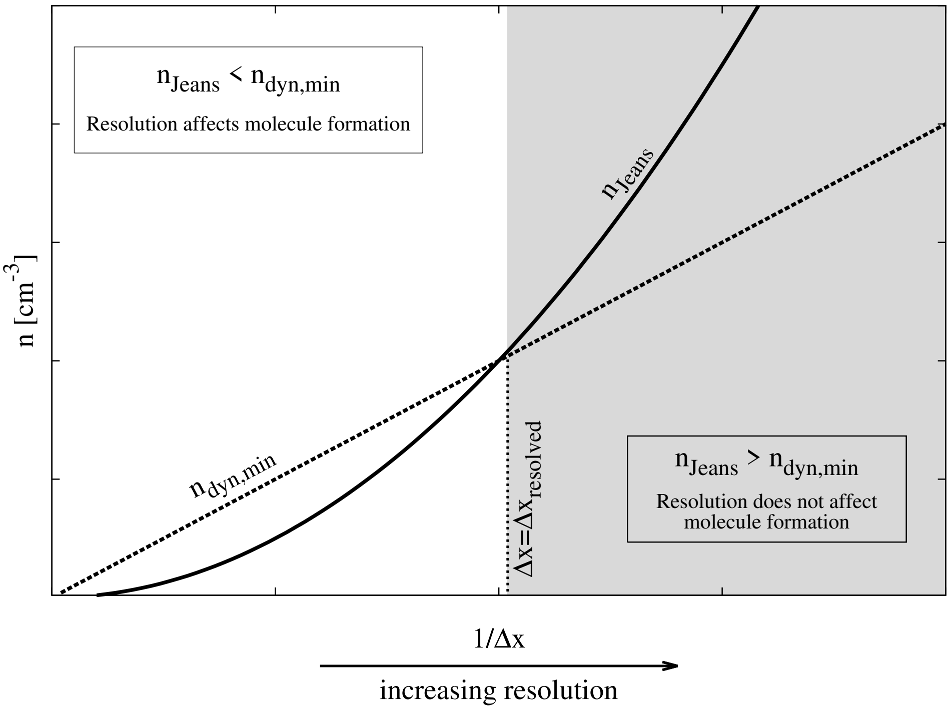
$n_{Jeans} < n_{dyn,min}$
Resolution affects molecule formation
n_{Jeans}
$n_{dyn,min}$
$\Delta x = \Delta x_{resolved}$
$n_{Jeans} > n_{dyn,min}$
Resolution does not affect molecule formation
n [cm^{-3}]
1/Δx
increasing resolution

Figure 26: Sketch of $n_{\mathrm{dyn,min}}$ (Equation 9.13) and n_{Jeans} (Equation 9.16) as a function of the simulation resolution. In the shaded region, any further increase in resolution does not affect the molecule formation.

namical condition. For high resolutions in the shaded region, $n_{\mathrm{Jeans}} \geq n_{\mathrm{dyn,min}}$; any further increase in the resolution beyond $\Delta x_{\mathrm{resolved}}$ will not affect the molecule formation in cells, since $n_{\mathrm{dyn,min}}$ is always resolved by the simulation.

9.3 | RESOLUTION REQUIREMENTS IN CF RUNS

In this section, the theory of resolution requirement developed in the previous sections is applied to the results of the CF simulations.

REQUIREMENT FOR H_2 CONVERGENCE

The 2D-histogram in Figure 27 shows how the H_2 formation and dissociation timescales (Equations 3.8 and 9.4) are related with the gas number density in the CF-R10 run at $t = 20$ Myr. The colour code shows the mass of H_2 in each bin. The H_2-mass-weighted mean of the each distribution is displayed by the black, dashed ($\tau_{\mathrm{H_2,form}}$) and dotted ($\tau_{\mathrm{H_2,dissoc}}$) lines. The H_2 formation time is a direct function of the gas density; therefore, the tight power law relation is expected. On the other hand, the H_2 dissociation time is a function of the shielding parameters, that depend on the global distribution of the gas around a computational cell. Therefore, it is surprising that the mean dissociation time is well-correlated with the gas density as well; note that the dispersion around the mean is still large because the dissociation time depends only indirectly on density via shielding. The intersection of the

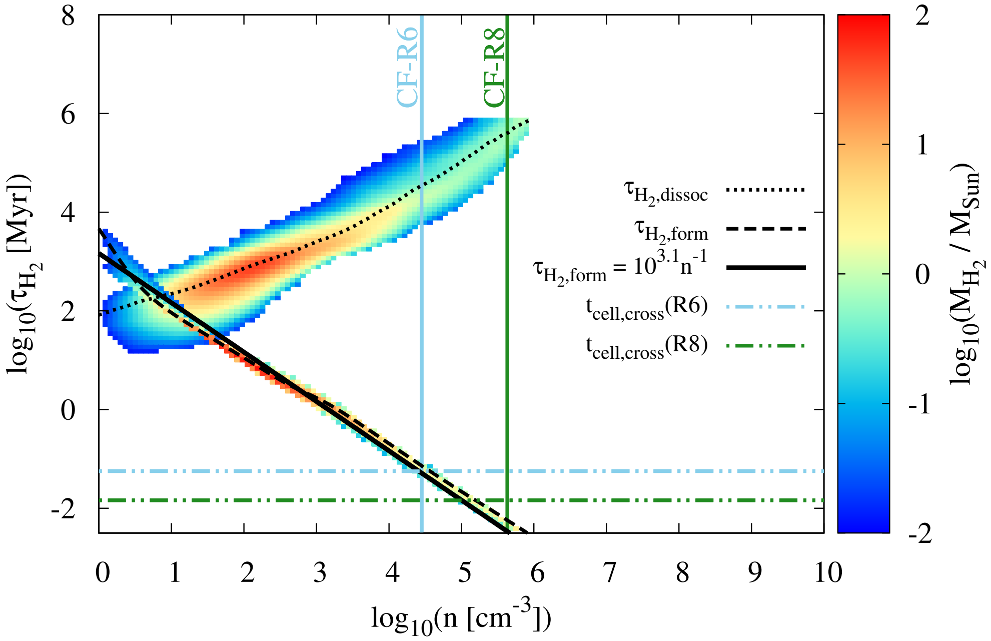

Figure 27: The distribution of the H_2 formation time-scale ($\tau_{H_2,form}$) and dissociation time-scale ($\tau_{H_2,dissoc}$) as a function of the number density of the cells in the highest resolution CF-R10 run at $t = 20$ Myr. The colour code denotes the mass of H_2. The dashed and dotted black lines denote the H_2-mass-weighted mean of the distributions. The solid, black line represents the power law fit for $\tau_{H_2,form}(n)$. The coloured, horizontal, dot-dashed lines show the cell-crossing time (Equation 9.12, with $\langle\sigma\rangle_{mass} = 2\,\mathrm{km\,s^{-1}}$) for two different resolution runs – cyan: CF-R6 and green: CF-R8. The coloured, vertical, solid lines refer to the Jeans density limit (Equation 9.15) of the CF-R6 and CF-R8 runs.

mean formation and dissociation times denote the minimum density at which the physical condition is fulfilled. The coloured, vertical, solid lines refer to the Jeans density corresponding to the spatial resolution of the CF-R6 and CF-R8 runs, as given by Equation 9.15 for cold gas. They provide an estimate of the maximum density resolved by the simulations.

The density criteria corresponding to the physical condition (Equation 9.1) is determined visually as

$$n_{phys,H_2} \gtrsim 10\,\mathrm{cm^{-3}}\,, \tag{9.17}$$

for which H_2 forms faster than it is dissociated.

In order to find the density criteria from the dynamical condition (Equation 9.11), the actual formation time of H_2 in the simulation is required. The solid, black line in Figure 27 denotes the linear fit for $\log_{10} \tau_{H_2,form}(\log_{10} n)$ for the cells that satisfy the physical condition. This leads to the power law relation

$$\tau_{H_2,form} = 10^{3.1}\,\mathrm{Myr}\left(\frac{n}{1\,\mathrm{cm^{-3}}}\right)^{-1}, \tag{9.18}$$

which is similar to the equilibrium H_2 formation time-scale ($\tau_{H_2,eq}$, Equation 3.7).

Substituting the time-scales from Equations 9.18 and 9.12 in Equation 9.11, the gas number density which fulfills the dynamical condition for the H_2 molecule is

$$n_{\mathrm{dyn,H_2}} \geq 10^{3.1}\ \mathrm{cm^{-3}} \left(\frac{\langle\sigma\rangle_{\mathrm{mass}}}{1\ \mathrm{km\ s^{-1}}}\right) \left(\frac{\Delta x}{1\ \mathrm{pc}}\right)^{-1} . \tag{9.19}$$

These density estimates are sufficient for the theoretical understanding of the resolution criteria. However, it is practical to have an estimate of the spatial resolution required to simulate the formation of a molecular cloud with converged molecule formation. Therefore, Equation 9.15 can be used to find an expression for the required spatial resolution as a function of the gas number density, gas composition, and temperature

$$\begin{aligned} \Delta x &= \frac{1}{\mu\, m_{\mathrm{p}}\, N_{\mathrm{J}}} \sqrt{\frac{\pi k_{\mathrm{B}} T}{n\, G}} , \\ &= 50\ \mathrm{pc} \frac{1}{\mu\, N_{\mathrm{J}}} \left(\frac{T}{10\ \mathrm{K}}\right)^{1/2} \left(\frac{n}{1\ \mathrm{cm^{-3}}}\right)^{-1/2} . \end{aligned} \tag{9.20}$$

For simplicity, $N_{\mathrm{J}} = 1$ is used for the conversion between the number density and spatial resolution.

Substituting the density from Equation 9.17 in Equation 9.20, and taking $\mu = 1.27$, $N_{\mathrm{J}} = 1$, and $T = 100$ K for the H_2 forming cold atomic gas, the required spatial resolution to satisfy the physical condition for H_2 formation is

$$\Delta x_{\mathrm{phys,H_2}} \lesssim 40\ \mathrm{pc} . \tag{9.21}$$

Therefore, a low spatial resolution of $\sim$ 40 pc is enough to obtain densities for which H_2 formation from the warm neutral medium is faster than H_2 dissociation.

Similarly, for the dynamical condition, substituting Equation 9.19 in Equation 9.20, the expression for H_2 is

$$\Delta x_{\mathrm{dyn,H_2}} \leq 2\ \mathrm{pc} \left(\frac{1}{\mu\, N_{\mathrm{J}}}\right)^2 \left(\frac{T}{10\ \mathrm{K}}\right) \left(\frac{\langle\sigma\rangle_{\mathrm{mass}}}{1\ \mathrm{km\ s^{-1}}}\right)^{-1} . \tag{9.22}$$

The molecule formation is effective for the dense gas with $n > 10\ \mathrm{cm^{-3}}$ (Equation 9.17). An important parameter to determine the required spatial resolution is the velocity dispersion of the dense gas. Figure 28 shows the evolution of the mass weighted mean velocity dispersion of the dense gas with number density $n > 10\ \mathrm{cm^{-3}}$ for the CF setup. Note that the mean velocity dispersion is independent of the resolution of the simulation. Nevertheless, the highest resolution CF-R10 run is taken, in which $\langle\sigma\rangle_{\mathrm{mass}} \sim 2\ \mathrm{km\,s^{-1}}$ is maintained after 5 Myr of evolution as the dense regions become progressively more massive. The CF setup is able to maintain this velocity dispersion because the gravitational collapse of such dense regions is delayed due to a continuous inflow of the WNM. The gravitational energy is not able to quickly overcome the turbulent kinetic energy provided by the colliding WNM. In addition, the periodic boundary conditions for gravity in the y– and z– directions does not allow the cloud to easily collapse in these directions. If the turbulent support from the inflow is stopped, a significant increase in the velocity dispersion due to both local and global gravitational collapse occurs, as demonstrated by Vázquez-Semadeni et al. (2007) in their colliding

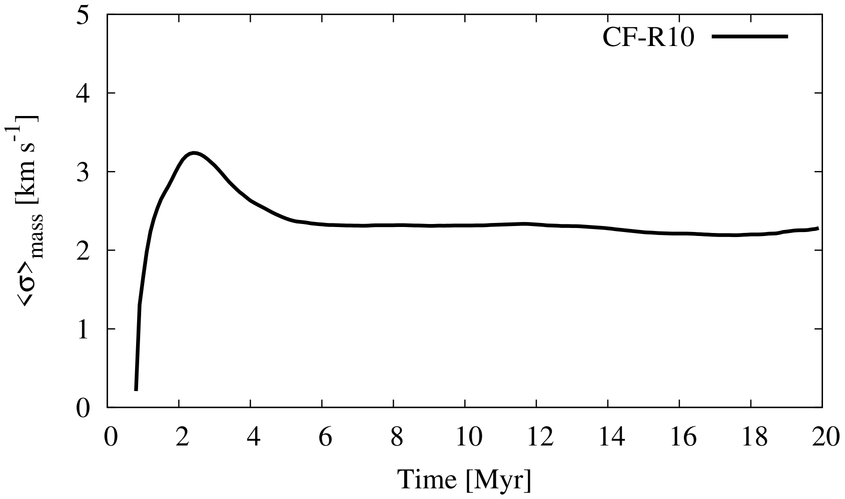

Figure 28: The evolution of the mass weighted mean velocity dispersion $\langle\sigma\rangle_{\rm mass}$ in the CF-R10 run. Only the cells with density $n > 10~{\rm cm}^{-3}$ are considered, for which $\langle\sigma\rangle_{\rm mass} \sim 2~{\rm km\,s}^{-1}$ is maintained.

flow simulations.

For the typical velocity dispersion $\langle\sigma\rangle_{\rm mass} \sim 2~{\rm km\,s}^{-1}$, the cell-crossing time $t_{\rm cell,cross}$ for two different resolution runs is shown by the horizontal, dot-dashed lines (cyan: CF-R6 and green: CF-R8) in Figure 27. The intersection of the formation time (Equation 9.18) and the cell-crossing times denote the minimum density at which the dynamical condition is fulfilled.

In the dense regions where the dynamical condition is important, $T = 10\,{\rm K}$ and $\mu \in [1.27, 2.35]$ depending on whether the H_2 forming region is locally predominantly atomic or molecular. This results in the required spatial resolution of

$$\Delta x_{\rm dyn,H_2} \lesssim \begin{cases} 0.6~{\rm pc} & \text{for } \mu = 1.27 \\ 0.2~{\rm pc} & \text{for } \mu = 2.35\,, \end{cases} \tag{9.23}$$

that are two orders of magnitude higher than the resolution required to fulfill the physical condition.

Requirement for CO convergence

The 2D-histograms in Figure 29 show the distribution of the formation and dissociation time-scales of CO (Equations 3.27 and 9.10) as a function of the gas number density in the CF-R10 run at $t = 20$ Myr. The colour code denotes the mass of CO in each bin. The CO-mass-weighted mean of the each distribution is displayed by the black, dashed ($\tau_{\rm CO,form}$) and dotted ($\tau_{\rm CO,dissoc}$) lines. The horizontal dot-dashed lines and the vertical, solid lines are identical to those in Figure 27.

The density criteria corresponding to the physical condition (Equation 9.1) for CO is

$$n_{\rm phys,CO} \gtrsim 10^4~{\rm cm}^{-3}\,, \tag{9.24}$$

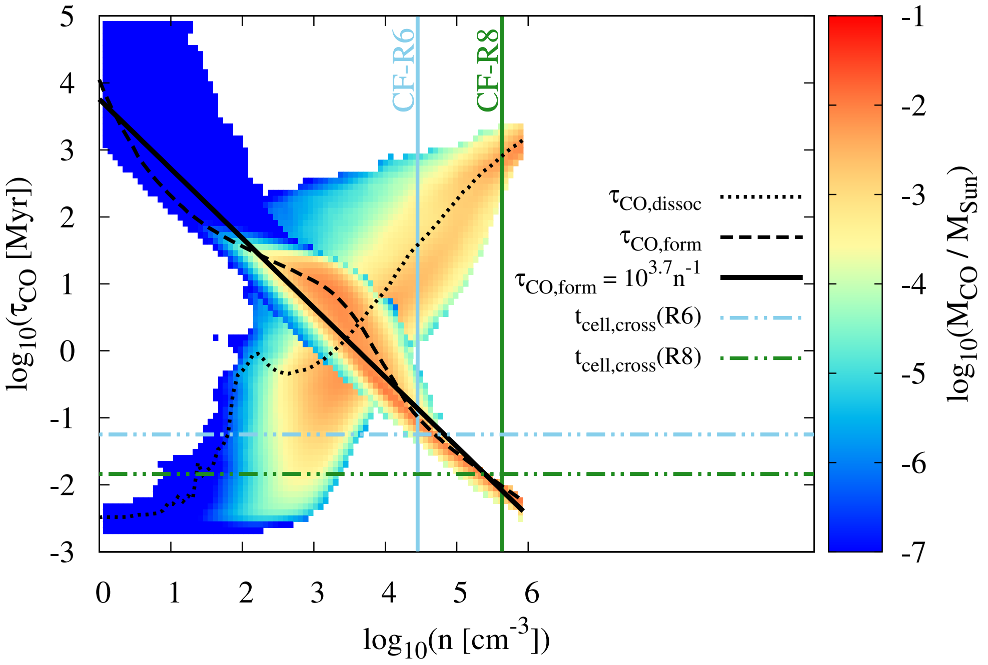

Figure 29: As in Figure 27 now for CO. The solid, black line represents the power law fit for $\tau_{CO,form}(n)$ for densities $n > 10^4$ cm^{-3} that fulfill the physical condition (Equation 9.1). The dynamical condition (Equation 9.11) is fulfilled at a much higher density associated with the CF-R8 run.

and cells fulfilling this criterion contain most of the CO mass.

The solid, black line in Figure 29 shows the linear fit of $\log_{10} \tau_{CO,form}(\log_{10} n)$ for the cells that satisfy the physical condition. This leads to the power law relation

$$\tau_{CO,form} = 10^{3.7} \text{ Myr} \left(\frac{n}{1 \text{ cm}^{-3}}\right)^{-1} . \tag{9.25}$$

Thus, the typical CO formation time-scale is slightly longer than the H_2 formation time-scale (Equation 9.18). Note that this fit is not as good a representative as the similar fit for $\tau_{H_2,form}$, due to the complex chemistry of CO. In particular, the mean $\tau_{CO,form}$ is significantly longer than the time given by this fit for the range 10^3 cm^{-3} $< n <$ 10^4 cm^{-3} .

Now, from Equations 9.25, 9.12, and 9.11, the gas number density which fulfills the dynamical condition for the CO molecule is found to be

$$n_{dyn,CO} \geq 10^{3.7} \text{ cm}^{-3} \left(\frac{\langle\sigma\rangle_{mass}}{1 \text{ km s}^{-1}}\right) \left(\frac{\Delta x}{1 \text{ pc}}\right)^{-1} . \tag{9.26}$$

Therefore, the density required for the CO formation process to fulfill the dynamical condition is ~ 4 times higher than that for H_2.

The required spatial resolution to satisfy the physical condition for CO formation is obtained by substituting the density from Equation 9.24 in Equation 9.20. Taking

$\mu = 2.35$, $N_\mathrm{J} = 1$, and $T = 10$ K for the CO forming molecular (H_2) gas,

$$\Delta x_\mathrm{phys,CO} \lesssim 0.2 \text{ pc}. \tag{9.27}$$

Therefore, a fairly high spatial resolution is required to obtain densities for which CO formation is faster than CO dissociation.

Similarly, for the dynamical condition, Equations 9.26 and 9.20 result in

$$\Delta x_\mathrm{dyn,CO} \leq 0.5 \text{ pc} \left(\frac{1}{\mu\, N_\mathrm{J}}\right)^2 \left(\frac{T}{10 \text{ K}}\right) \left(\frac{\langle\sigma\rangle_\mathrm{mass}}{1 \text{ km s}^{-1}}\right)^{-1}. \tag{9.28}$$

With $\langle\sigma\rangle_\mathrm{mass} \sim 2$ km s^{-1} and μ, N_J, T as before, the required spatial resolution for converged CO formation is:

$$\Delta x_\mathrm{dyn,CO} \lesssim 0.04 \text{ pc}. \tag{9.29}$$

Overall, for the CF setup, the resolution requirement from the dynamical condition is more strict for both H_2 and CO. The derived resolution requirements for H_2 and CO are in agreement with the simulation results in Chapter 8. Figure 27 shows that the CF-R6 run with $\Delta x = 0.125$ pc is able to fulfill both the physical and dynamical condition for H_2 formation. Similarly, Figure 29 shows that the CF-R8 run with $\Delta x = 0.032$ pc is able to fulfill both conditions for CO formation.

9.4 | RESOLUTION REQUIREMENTS IN TB RUNS

Of the three sets of TB runs, the molecular content in low density TB-R*-n003 runs is negligible (see Figures 14 and 16). This is an extreme case in which the molecule dissociation time (especially for CO) is quite short and any molecule formed is immediately destroyed, and is investigated in the next chapter. In the high density TB-R*-n300 runs, the gas quickly becomes saturated with molecules. These runs are not evolved with gravity, rendering the use of Jeans density to estimate the spatial resolution invalid. Thus, they are not considered for further investigation in this thesis. The intermediate density TB-R*-n030 runs show decent molecule formation in a turbulent medium and therefore, are suitable TB runs to investigate the derived resolution criteria.

REQUIREMENT FOR H_2 CONVERGENCE

Figure 30 shows that the H_2 formation time-scale ($\tau_{H_2\mathrm{,form}}$, mean indicated by dashed line) for the gravitating gas in the TB-n030-R7 run at 20 Myr is in fact similar to that seen in the CF runs (Figure 27). Therefore, the density expression in Equation 9.19 is valid for the TB runs as well.

There is a notable difference in the density at which the physical condition (Equation 9.1) is satisfied because of the significantly different distribution of the dissociation time-scale ($\tau_{H_2\mathrm{,dissoc}}$, mean indicated by dotted line). The TB-R7-n030 run starts with cold atomic gas ($n_0 = 30$ cm^{-3}) and Figure 30 shows that the density criteria corresponding to the physical condition is $n > 1$ cm^{-3}. The coloured, horizontal, dot-dashed lines denote the cell-crossing time $t_\mathrm{cell,cross}$ (Equation 9.12,

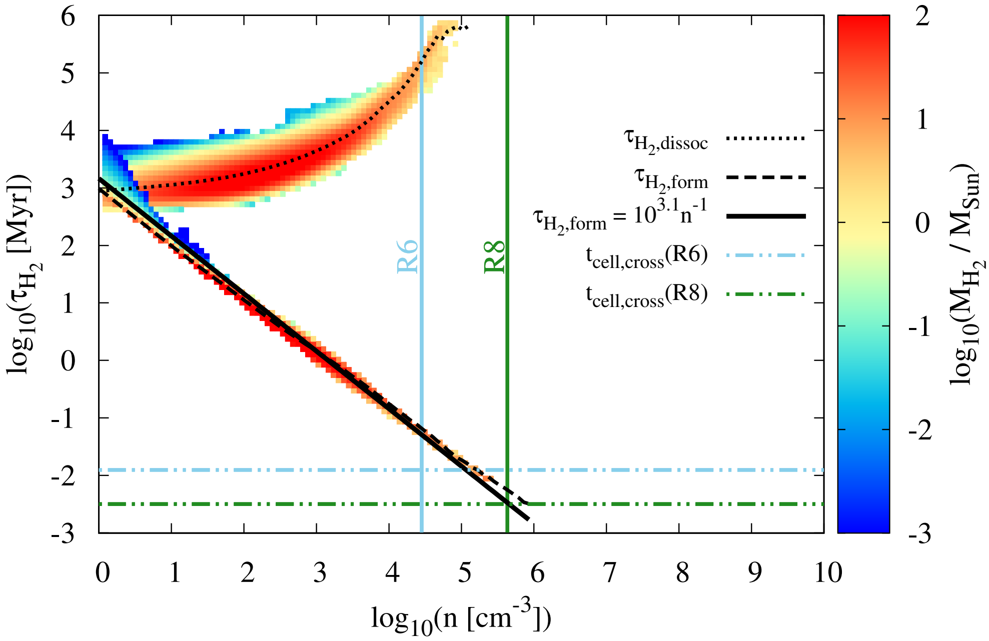

Figure 30: As in Figure 27, now for the TB-R7-n030 run at $t = 20$ Myr. The cell crossing time denoted by the horizontal dot-dashed lines are quite low since the velocity dispersion in the TB runs is high.

with $\langle\sigma\rangle_{\rm mass} = v_{\rm rms} = 10\ {\rm km\,s^{-1}}$ by construction) corresponding to two different resolutions – cyan: R6 and green: R8. The coloured, vertical, solid lines refer to the density corresponding to the spatial resolution of R6 and R8, as in Figure 27. It is evident that the TB-R6-n030 run is not sufficient to fulfill the dynamical condition. Instead, the distribution indicates that refinement level 8 or higher would be required to fulfill both conditions for the H_2 molecule. This is attributed to the very short cell-crossing time.

For the gravitating gas in the TB-R*-n030 runs at $t = 20$ Myr, Equation 9.22 can be directly employed to obtain the necessary spatial resolution for converged H_2 formation. For $\langle\sigma\rangle_{\rm mass} = 10\ {\rm km\,s^{-1}}$, this results in

$$\Delta x_{\rm dyn,H_2} \lesssim \begin{cases} 0.1\ {\rm pc} & \text{for } \mu = 1.27 \\ 0.04\ {\rm pc} & \text{for } \mu = 2.35 \end{cases} \tag{9.30}$$

Requirement for CO convergence

Figure 31 shows the distribution of the CO formation ($\tau_{\rm CO,form}$, mean indicated by dashed line) and dissociation time-scale ($\tau_{\rm CO,dissoc}$, mean indicated by dotted line) in the TB-n030-R7 run at 20 Myr. The distribution of $\tau_{\rm CO,form}$ is similar to that seen in the CF runs (Figure 29). Thus, the density expression in Equation 9.26 is valid for the TB runs as well.

The density at which the physical condition (Equation 9.1) is satisfied ($n \gtrsim 10^3 - 10^4\ {\rm cm^{-3}}$) is the same for both CF and TB simulations. The coloured, horizontal, dot-dashed lines and the vertical, solid lines are identical to those in Figure 30. Des-

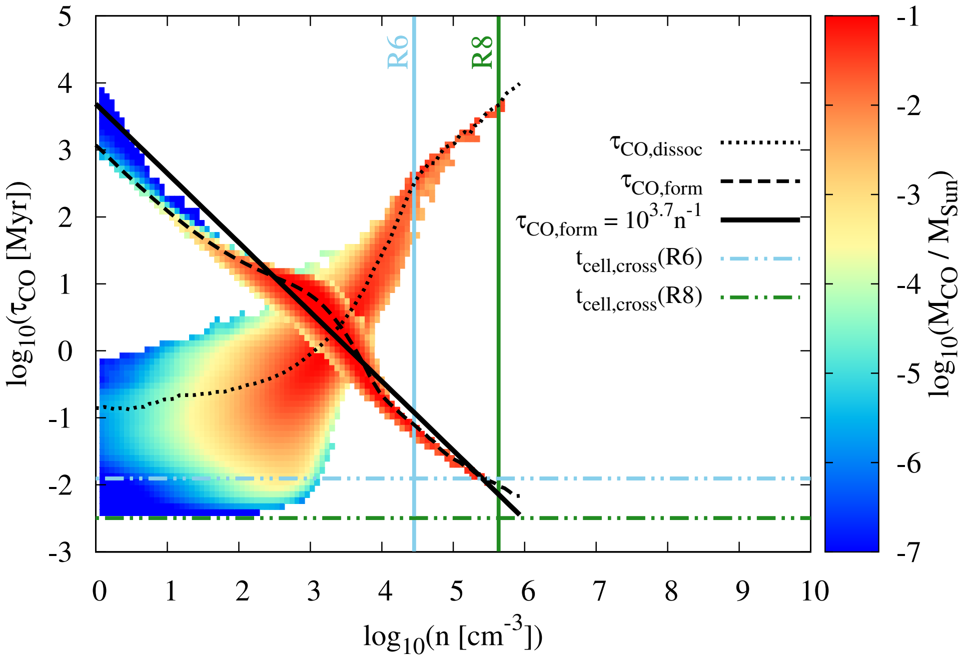

Figure 31: As in Figure 29, now for the TB-R7-n030 run at $t = 20$ Myr. The low cell-crossing time due to high velocity dispersion suggests that even a TB-R8-n030 run would not have a converged CO formation .

pite the similarity in the distribution of $\tau_{\mathrm{CO,form}}$ with that in the CF run (Figure 29), neither TB-R6-n030 nor a run with four times higher resolution (R8) has sufficient spatial resolution to fulfill the dynamical condition.

In order to estimate the required resolution for converged CO formation in the TB runs, Equation 9.28 can be used. For $\langle\sigma\rangle_{\mathrm{mass}} = 10\,\mathrm{km\,s^{-1}}$, this results in

$$\Delta x_{\mathrm{dyn,CO}} \lesssim 0.01\ \mathrm{pc}\,. \tag{9.31}$$

This mean the simulation TB-R10-n030 would have to be performed to reach the convergence of CO formation.

ESTIMATE OF THE RESOLUTION REQUIREMENT FOR NON-GRAVITATING GAS

For non-gravitating gas, Equation 9.20, which converts a density to a spatial resolution using the Jeans condition, is not applicable. In such cases, the effect of the velocity dispersion on the resolution requirement can be explained directly via the density PDFs. Figure 18 shows that the density PDFs in the pre-gravity phase are approximately log-normal, and higher resolution runs sample the high density regions more. According to Equation 9.19, simulations with higher $\langle\sigma\rangle_{\mathrm{mass}}$ require higher densities to satisfy the dynamical condition. Therefore, if the spatial resolution in simulations of non-gravitating gas is high enough to sufficiently sample the minimum densities given by Equation 9.19 and 9.26, the molecule formation converges.

9.5 | CHAPTER SUMMARY

In this chapter, the physical and dynamical conditions that determine the resolution requirements for molecule formation (Equations 9.1 and 9.11) were investigated via the relations between the molecule formation time, the molecule dissociation time, and the typical time spent by fluid elements in a computational cell. The molecule formation and dissociation time determined from the analytic expressions (e.g. Equations 3.8 and 3.27) were applied to the distribution of the gas-density in the CF and intermediate density TB setups. In both cases, the dynamical condition was found to be more restrictive than the physical condition for both H_2 and CO. The correlation obtained between the density and time-scales (Equations 9.18 and 9.25) were taken as representative expressions for the evolution of the gas and the resolution criteria for converged H_2 and CO formation were evaluated. The required spatial resolution was found to depend on the composition, temperature, and the strength of turbulence of the MC forming dense gas. For the less turbulent clouds in the CF setup, H_2 formation is expected to converge for a spatial resolution of $\Delta x \lesssim 0.2$ pc and CO formation for $\Delta x \lesssim 0.04$ pc. These derived requirements are in agreement with the simulation results of the CF setup in Chapter 8. The turbulence in the TB setup is ~ 5 times stronger, indicating ~ 5 times higher resolution requirement for chemical convergence.

10 | Aspects of the resolution criteria

In this chapter, some aspects of the resolution criteria introduced in the previous chapter are further investigated to ascertain the robustness of the criteria.

The physical condition was weaker than the dynamical condition for both H_2 and CO formation in the simulations studied in the previous chapter. A simulation where the physical condition exerts a more restrictive resolution requirement is presented in Section 10.1.

The molecule formation time is well-correlated with the gas-density distribution. This is generally not the case for molecule dissociation time because it is largely dictated by the shielding of the ISRF by the inhomogeneous distribution of dust and molecules around the fluid element. A general density criteria for the physical condition (Equation 9.1), as a function of the strength of the radiation field and the gas shielding properties, is discussed in Section 10.2.

The Jeans density limit for a given spatial resolution was taken as the maximum density resolved by the simulation, and compared against the densities at which the physical and dynamical conditions were fulfilled. The importance of avoiding numerical artefacts in the dense structures for converged chemical evolution is briefly discussed in Section 10.3.

The resolution requirements are strongly related to the velocity dispersion of the gas via the dynamical condition. The effect of velocity dispersion on the requirement, as predicted by Equations 9.22 and 9.28, is verified in Section 10.4.

The resolution criteria for a converged evolution of the molecules in gas was derived from the snapshot at the end of the simulation. The validity of the fitted lines such as Equations 9.18 and 9.25 for the chemical evolution is discussed in Section 10.5.

Finally, the possibility to relax the strict resolution requirement resulting from the cell-crossing time in the dynamical condition (Equation 9.11) is discussed in Section 10.6.

10.1 | A CASE OF FAST MOLECULE DISSOCIATION

The low density TB run (TB-R7-n003) is a suitable simulation to illustrate the chemical evolution in regions with low visual extinction. Here, the ISRF can easily

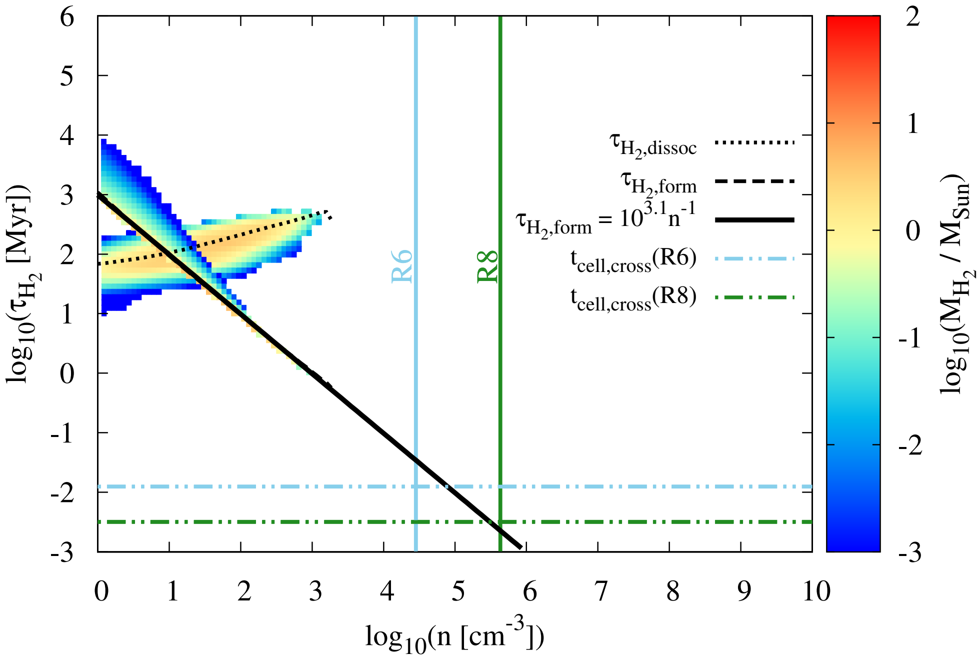

Figure 32: As in Figure 30, now for the TB-R7-n003 run at $t = 20$ Myr. The mean H_2 formation time is defined by the same power-law fit as before. The physical condition is weaker than the dynamical condition.

penetrate into the dense regions, and the molecule dissociation time is quite short. As discussed below, this setup also provides a scenario where the resolution requirement from the physical condition is stronger than that from the dynamical condition (for CO formation).

The 2D-histogram in Figure 32 shows the H_2 formation ($\tau_{\mathrm{H_2,form}}$, dashed line) and dissociation time-scale ($\tau_{\mathrm{H_2,dissoc}}$, dotted line) at various densities in the TB-R7-n003 run at $t = 20$ Myr. The horizontal dot-dashed lines and vertical solid lines are identical to those in Figure 30. The power-law fit given by Equation 9.18 perfectly represents the mean $\tau_{\mathrm{H_2,form}}$ (they overlap in the figure). Similar to the H_2 formation in the CF setup, the density criteria from the physical condition is $n \gtrsim 10\,\mathrm{cm}^{-3}$. Thus, for H_2 formation, the physical condition is weaker than the dynamical condition.

In case of CO formation, however, the situation is quite different. The 2D-histogram in Figure 33 shows the CO formation ($\tau_{\mathrm{CO,form}}$, dashed line) and dissociation time-scale ($\tau_{\mathrm{CO,dissoc}}$, dotted line) in the TB-R7-n003 run at $t = 20$ Myr. The CO dissociation time is orders of magnitude shorter than the CO formation time, even at densities $n \sim 10^3\,\mathrm{cm}^{-3}$. There is no correlation between $\tau_{\mathrm{CO,dissoc}}$ and the density of the gas. Thus, the gas density is no longer a good indicator of the local CO dissociation time to study the physical condition.

In fact, $\tau_{\mathrm{CO,dissoc}}$ is shorter than the typical cell-crossing time in the simulation ($t_{\mathrm{cell,cross}}$, horizontal dot-dashed lines as in Figure 31). A direct consequence of this is that the physical condition is satisfied at much higher densities and potentially becomes more restrictive than the dynamical condition. Therefore, the density criteria given by the physical condition is largely dictated by the effect of the shielding

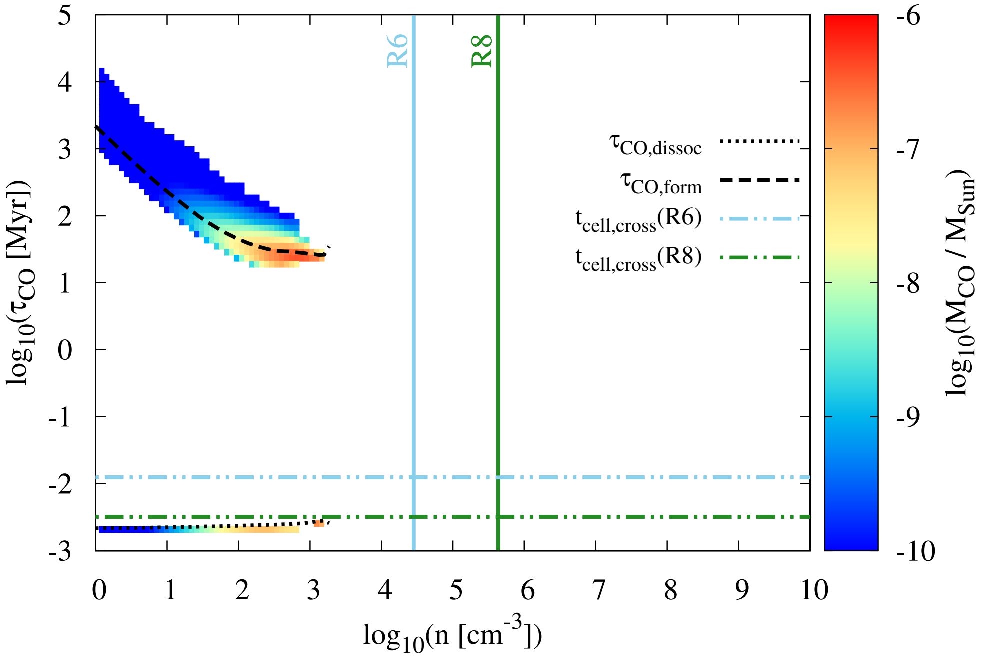

Figure 33: As in Figure 31, now for the TB-R7-n003 run at $t = 20$ Myr. The CO dissociation time is shorter than the cell-crossing time. Therefore, the physical condition is potentially more restrictive than the dynamical condition.

properties of the gas on the molecule dissociation time-scale.

10.2 | A GENERAL EXPRESSION FOR THE PHYSICAL CONDITION

Glover et al. (2010) stressed that in regions with low visual extinction, the molecular chemistry is influenced more by the distribution of the shielding experienced by the fluid element and less by its density. In the 2D-histograms of the molecular formation/dissociation time-scale and the gas density, the same power-law fit is suitable for the H_2 formation time-scale (Figures 27, 30, and 32). Similar is true for the CO formation time-scale (Figures 29 and 31). However, the distribution of molecule dissociation time varies from simulation to simulation. Therefore, the density criteria corresponding to the physical condition (e.g. Equation 9.17) was obtained only via visual inspection of the distributions.

The molecule dissociation times (Equations 9.4 and 9.10) are determined from the shielding factors of the molecules ($f_{\mathrm{shield,H_2}}$ and $f_{\mathrm{shield,CO}}$, see Section 4.4), that are non-linear functions of the molecular column density. On the other hand, the visual extinction A_V is a linear scaling of the total hydrogen column density (Equation 4.11). Thus, if there is a good correlation between $f_{\mathrm{shield,H_2}}/f_{\mathrm{shield,CO}}$ and A_V, the molecule dissociation time can be calculated as a function of A_V. In the following, the analytic expressions for $\tau_{\mathrm{H_2,dissoc}}$ and $\tau_{\mathrm{CO,dissoc}}$ are derived from the gas distribution in the high-resolution CF-R10 run. Then, a general expression for the

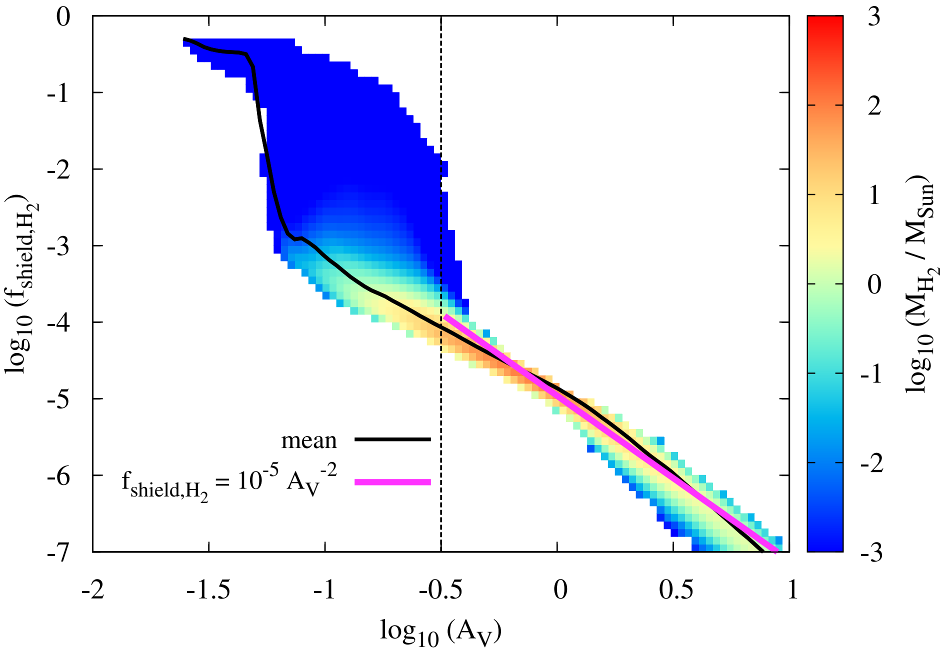

Figure 34: Mass weighted distribution of the shielding factor $f_{\text{shield},\text{H}_2}$ as a function of the visual extinction (A_V) in the CF-R10 run at $t = 20$ Myr. The vertical-dashed line indicates $A_\text{V} = 0.3$, above which most of the H_2 mass is found. Black line denotes the mean of the distribution and the pink line is the power-law fit in the range $0.3 < A_\text{V} < 10$.

density criteria resulting from the physical condition is obtained.

SHIELDING EXPERIENCED BY H_2

The shielding of the ISRF by dust and other H_2 molecules prevents the destruction of H_2 by photo-dissociation in the dense, molecular regions of a cloud. The photo-dissociation rate of H_2 modelled in the chemistry network is given by Equation 4.13. Figure 34 shows the relation between the visual extinction (A_V) and $f_{\text{shield},\text{H}_2}$ experienced by the cells in the CF-R10 run at $t = 20$ Myr. For each cell, these variables are weighted averages over the HEALPIX pixel values computed by the OPTICALDEPTH module (see Section 4.4). The colour-bar shows the mass of H_2 in each bin. As expected, majority of H_2 forms at $A_\text{V} \geq 0.3$ (Röllig et al. 2007, see also Figure 41). At lower A_V values, the scatter in $f_{\text{shield},\text{H}_2}$ is high. The power-law fit in the range $0.3 < A_\text{V} < 10$ is given by

$$f_{\text{shield},\text{H}_2} = 10^{-5} A_\text{V}^{-2} \,. \tag{10.1}$$

SHIELDING EXPERIENCED BY CO

Rapid CO formation sets in only when enough H_2 is formed to effectively shield the photo-dissociating radiation from reaching the CO molecules (see Figure 19). The photo-dissociation rate of CO modelled in the chemistry network is given by Equation 4.15. Figure 35 shows the relation between the visual extinction (A_V) and $f_{\text{shield},\text{CO}}$ experienced by the cells in the CF-R10 run at $t = 20$ Myr. Most of the CO

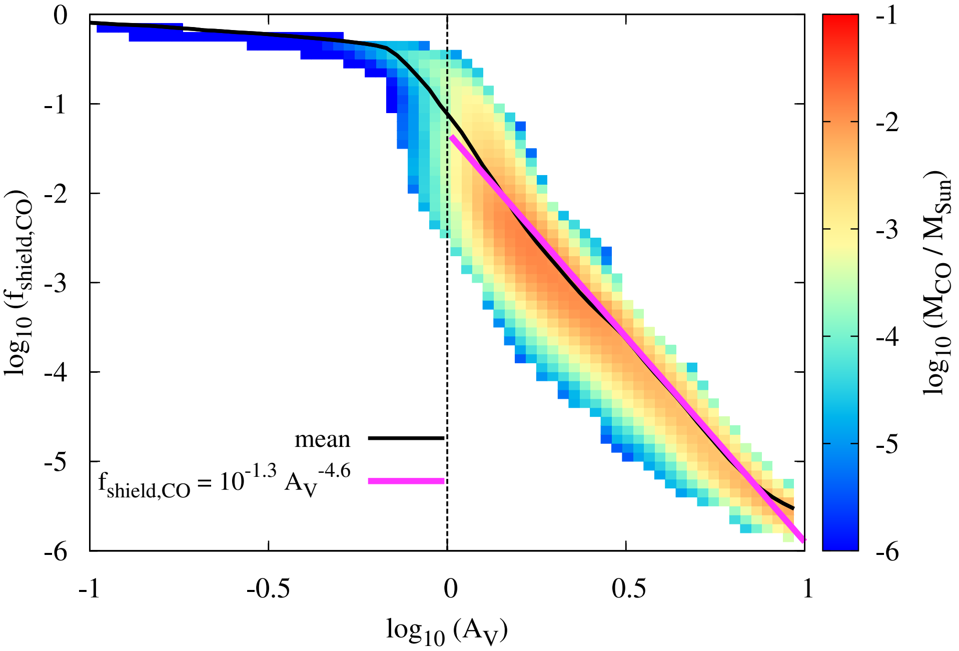

Figure 35: As in Figure 34, now for the CO shielding factor $f_{\text{shield,CO}}$. The vertical-dotted line indicates $A_{\text{V}} = 1$, above which most of the CO mass is found. Black line denotes the mean of the distribution and the pink line is the power-law fit in the range $1 < A_{\text{V}} < 10$.

is found at $A_{\text{V}} \geq 1$, as noted by Röllig et al. (2007), Clark et al. (2012b), and Gong et al. (2018) (see also Figure 41). The power-law fit in the range $1 < A_{\text{V}} < 10$, given by

$$f_{\text{shield,CO}} = 10^{-1.3} A_{\text{V}}^{-4.6} \ . \tag{10.2}$$

THE A_{V} DEPENDENT PHYSICAL CONDITION

From Equations 9.4 and 10.1, the H_2 photo-dissociation time-scale is given by

$$\tau_{\text{H}_2,\text{dissoc}} \approx 96 \, \text{Myr} \, \frac{1}{G_0} \, A_{\text{V}}^2 \exp(3.5 A_{\text{V}}) \, . \tag{10.3}$$

From Equations 9.10 and 10.2, the CO photo-dissociation time-scale is

$$\tau_{\text{CO,dissoc}} \approx 5 \times 10^{-3} \, \text{Myr} \, \frac{1}{G_0} \, A_{\text{V}}^{4.6} \, \exp(2.5 \, A_{\text{V}}) \, . \tag{10.4}$$

Figure 36 displays the newly derived $\tau_{\text{H}_2,\text{dissoc}}$ as solid, black line and $\tau_{\text{CO,dissoc}}$ as solid, blue line. Below the A_{V} where the power-law fits in Figures 34 and 35 are not applicable, the solid lines are cut-off by thin dashed lines. The molecule dissociation time when shielding by dust alone is considered is plotted for H_2 as the black, dot-dashed line and for CO as the blue, dot-dashed line. The dissociation time is much longer when the molecular shielding effects are accounted for. The dissociation time of CO is orders of magnitude shorter than that of H_2 at the same A_{V}, hinting towards a stronger resolution requirement for the convergence of CO

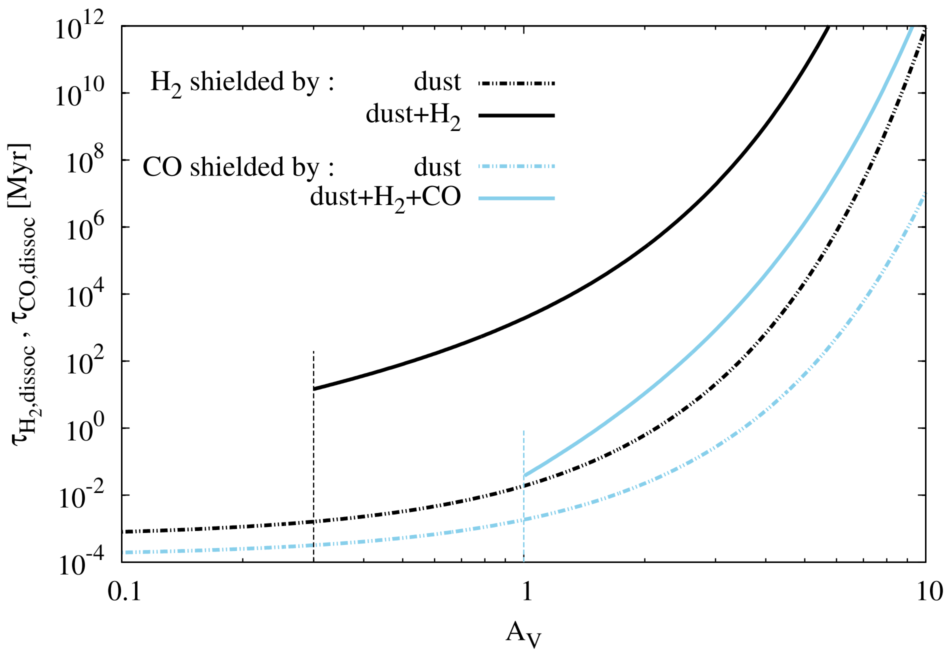

Figure 36: The H_2 and CO photo-dissociation time-scales as functions of A_V. The black lines denote the H_2 dissociation times and the blue lines denote the CO dissociation times. The solid lines indicate when the ISRF is shielded by dust and molecules. These lines are cut-off at the A_V limit below which the fits in Figures 34 and 35 are not applicable. The dot-dashed lines indicate when the dissociating radiation is shielded by dust alone.

formation.

Using Equations 9.18 and 10.3, the physical condition (Equation 9.1) can be investigated. The resulting density criteria is

$$n_{\mathrm{phys,H_2}} \gtrsim 13\ \mathrm{cm}^{-3}\ G_0\, A_V^{-2} \exp(-3.5 A_V)\,. \tag{10.5}$$

Similarly, Equations 9.25 and 10.4 result in the density criteria for CO as

$$n_{\mathrm{phys,CO}} \gtrsim 10^6\ \mathrm{cm}^{-3}\ G_0\, A_V^{-4.6} \exp(-2.5 A_V)\,. \tag{10.6}$$

Thus, the physical condition depends on the strength of the molecule dissociating radiation and the mean A_V experienced by the fluid element in the simulation. Figure 34 shows that the majority of H_2 is found at $0.3 < A_V < 1$. The corresponding density criteria from the physical condition is

$$n_{\mathrm{phys,H_2}} \gtrsim \begin{cases} 86\ \mathrm{cm}^{-3} & \text{for } A_V = 0.3 \\ 1\ \mathrm{cm}^{-3} & \text{for } A_V = 1 \end{cases} \tag{10.7}$$

Similarly, Figure 35 shows the majority of CO is found at $1 < A_V < 3$, leading to the density criteria

$$n_{\rm phys,CO} \gtrsim \begin{cases} 1.4 \times 10^5~{\rm cm^{-3}} & \text{for } A_{\rm V} = 1 \\ 6~{\rm cm^{-3}} & \text{for } A_{\rm V} = 3 \end{cases} \tag{10.8}$$

Therefore, the density criteria arising from the physical condition is very sensitive to the distribution of dust and molecules in the simulation. The density requirements in Equations 10.7 and 10.8 incorporate the visually identified density criteria from the 2D-histograms in Figure 27 and 29.

10.3 | THE MOLECULAR CONTENT OF UNRESOLVED DENSE REGIONS

As explored in the previous sections, the chemical evolution in a cell of a simulation is directly affected by the 3D distribution of gas density around it. In Section 9.2, the Jeans density was introduced as the maximum density resolved by a simulation at a given resolution. Instabilities in the unresolved regions eventually bring significant numerical artefacts in the density structure. When a significant fraction of the gas mass in contained in such unresolved regions, the numerical errors will alter the non-linear dynamical and chemical evolution of the gas.

The top panel in Figure 37 shows the evolution of the percentage of the mass contained in the Jeans unresolved regions (i.e. $\rho > \rho_{\rm Jeans}$, Equation 9.14) of the CF runs. The bottom panel shows the amount of molecular gas (H_2 and CO) in such unresolved regions. The percentage of gas mass in unresolved dense regions is quite high for low resolution simulations ($\sim$ 30% in CF-R4). With increasing resolution, the amount of H_2 and CO in such regions is slightly higher; this is because the unresolved regions of high resolution runs correspond to higher densities, where the molecule formation time is shorter. In general, the percentage of molecular gas in unresolved regions is similar ($\sim$ 70%) at all resolutions. Therefore, the low resolution simulations contain a large amount of molecules in regions that are prone to artificial fragmentation. These regions appear as unphysical spikes in the PDFs of $A_{\rm V}$ and density at low resolutions (see Figures 24 and 25), leading to unnaturally high molecular content as the simulation progresses.

Unlike the CF runs that use the AMR technique to specifically refine the dense and gravitating regions, the TB runs have uniform refinement. Figure 38 shows the evolution of the unresolved dense regions for the intermediate density TB runs (TB-R*-n030). Note that the Jeans density threshold can only be applied to the gravitating gas after $t = 10$ Myr. Similar to the CF runs, the low resolution runs contain $20-30\%$, and the higher resolution runs contain $< 10\%$ of the mass in unresolved regions. Higher resolution runs also have slightly higher percentage of H_2 and CO in the unresolved regions; nevertheless, the unresolved regions contain $\sim$ 70% of the mass in molecules for all resolutions. Interestingly, the low resolution TB runs do not produce more H_2 and CO as the simulation progresses (see Figures 15 and 17). This is because, unlike the mildly turbulent gas in the CF run that retains the formed sub-structures, the high velocity dispersion in the TB runs regularly creates and destroys the unresolved regions making them transient features.

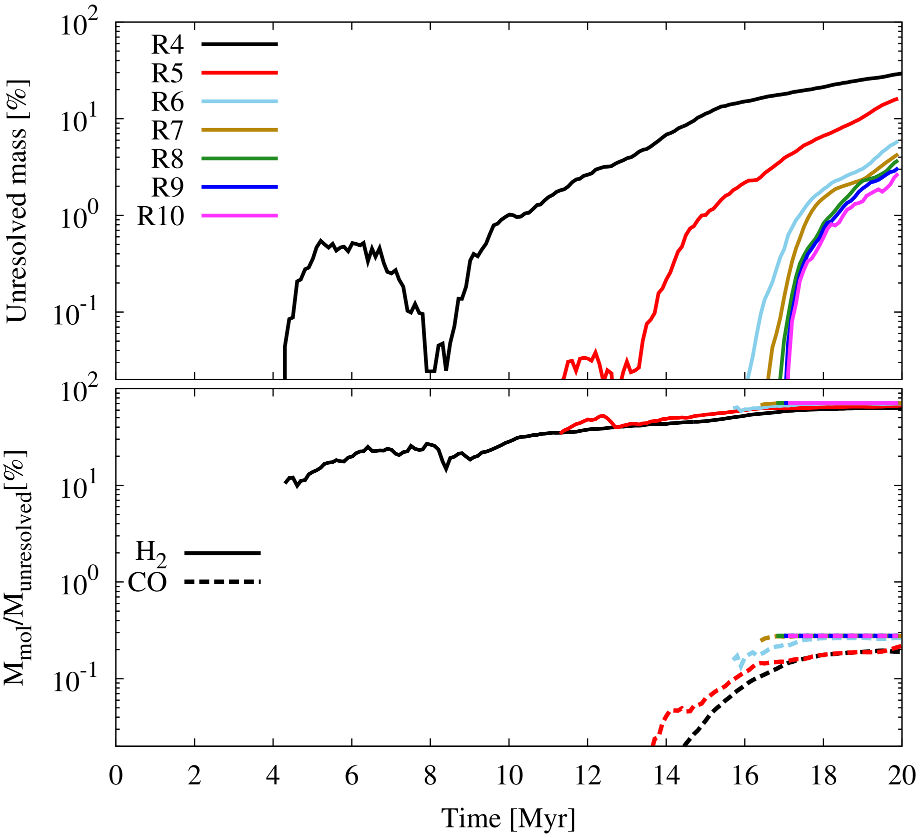

Figure 37: The evolution of the percentage of Jeans-unresolved mass in the CF-R[4-10] runs (see the density threshold relation in Equation 9.14). The top panel shows the percentage of the mass in the Jeans unresolved regions of the CF runs. The bottom panel shows the percentage of the mass of H_2 (solid lines) and CO (dashed lines) in the unresolved regions at different resolutions. In the low resolution runs (CF-R4 and CF-R5), the unresolved regions contain $> 10\%$ of the total gas mass, that in turn have $\sim 70\%$ of their mass in H_2 and CO.

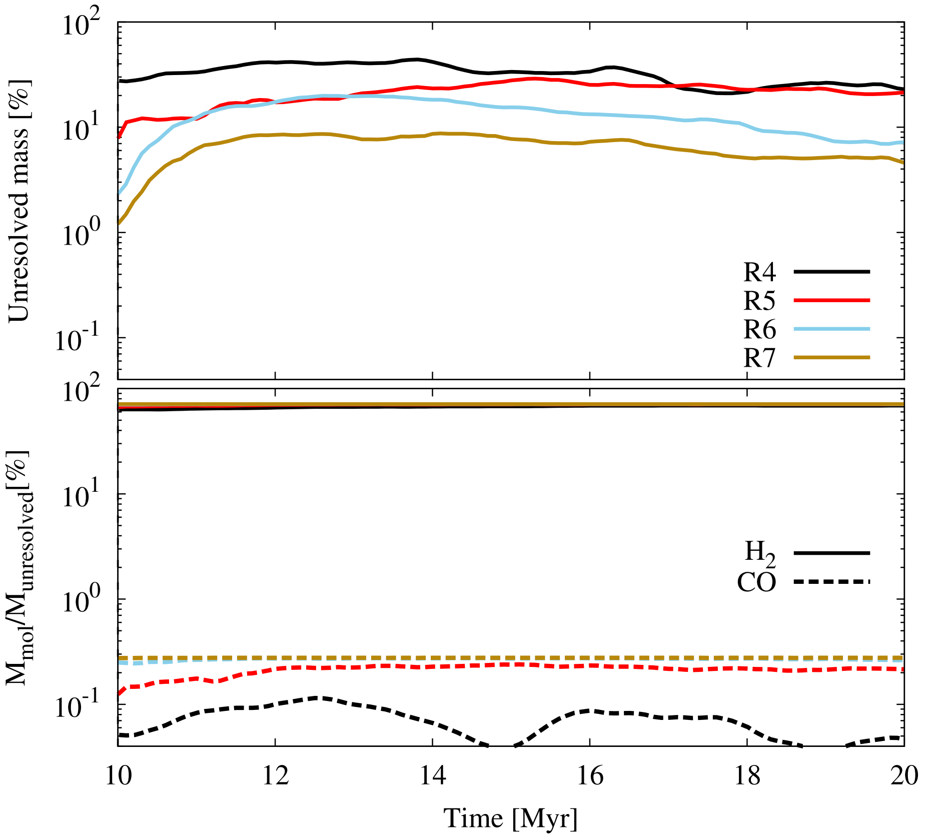

Figure 38: As in Figure 37, now for the TB-R[4-7]-n030 runs. Only the gravitating gas after $t = 10$ Myr is displayed. The unresolved regions in the runs contain $5 - 20\%$ of the total gas mass, depending on the resolution of the simulation. The unresolved regions again have $\sim 70\%$ of their mass in H_2 and CO.

10.4 | THE EFFECT OF VELOCITY DISPERSION

Compared to the resolution required for H_2 convergence in the CF simulations, the requirement given by Equation 9.30 or 9.31 for the TB runs is computationally very demanding. Equation 9.22 indicates that the convergence of H_2 chemistry is possible at lower resolutions if the velocity dispersion is lowered (i.e. if $t_{\mathrm{cell,cross}}$ is increased in Figure 30). This can be easily tested in the TB runs since $\langle\sigma\rangle_{\mathrm{mass}}$ is a tunable parameter of the setup.

The study of multiple velocity dispersion values is not feasible in the computationally expensive $(32\ \mathrm{pc})^3$ box. Therefore, a smaller $(8\ \mathrm{pc})^3$ simulation box is taken to carry out the TB-n030 runs with various $\langle\sigma\rangle_{\mathrm{mass}}$ values (see Table 5) and with resolutions corresponding to the TB-n030-R[5,6,7] runs. These test runs evolve for $t = 10$ Myr without gravity. There is effectively less mass and less shielding capacity of the gas, and this affects the physical condition (Equation 9.1, 10.5, 10.6). However, the physical condition is still less restrictive than the dynamical condition. Therefore, these runs are still valid to test the resolution requirement with various strengths of the supersonic turbulence in the gas.

The first column of Figure 39 shows the evolution of $\eta_{\mathrm{H_2}}$ (Equation 7.4) in the test runs. The results for various velocity dispersions are arranged in rows, increasing from top to bottom. It is evident that the low resolution simulations have converged evolution of H_2 content at low $\langle\sigma\rangle_{\mathrm{mass}}$. With increasing velocity dispersion, however, increasingly larger differences in $\eta_{\mathrm{H_2}}$ are seen between the different resolution runs. The results can be summarized as follows:

- H_2 convergence is possible even for the TB-n030-R5 run with $\Delta x = 0.250$ pc if $\langle\sigma\rangle_{\mathrm{mass}} = 1\ \mathrm{km\,s^{-1}}$.
- The TB-n030-R6 run with $\Delta x = 0.125$ pc is almost converged, with $\eta \gtrsim 80\%$ for $\langle\sigma\rangle_{\mathrm{mass}} = 2\ \mathrm{km\,s^{-1}}$ or $3\ \mathrm{km\,s^{-1}}$.
- When $\langle\sigma\rangle_{\mathrm{mass}} = 6\ \mathrm{km\,s^{-1}}$, $\eta_{\mathrm{H_2}}$ is significantly lower than 1 for the TB-n030-R[5,6] runs.

Equation 9.22 requires $\Delta x_{\mathrm{dyn,H_2}} \lesssim 0.4$, 0.2, 0.12, and 0.06 pc for $\langle\sigma\rangle_{\mathrm{mass}} = 1$, 2, 3, and $6\ \mathrm{km\,s^{-1}}$, respectively. Therefore, the numerical result from the test runs is consistent with the spatial resolution given by Equation 9.22 for various $\langle\sigma\rangle_{\mathrm{mass}}$ in the TB runs.

The second column of Figure 39 shows the evolution of η_{CO} (Equation 7.7) in the test runs. Even for the low velocity dispersion in the first row, the test runs have slightly dissimilar CO content at different resolutions. This is consistent with Equation 9.28, which requires $\Delta x_{\mathrm{dyn,CO}} \lesssim 0.08$ pc for $\langle\sigma\rangle_{\mathrm{mass}} = 1\ \mathrm{km\,s^{-1}}$. The high sensitivity of CO evolution on the resolution is immediately visible for all higher velocity dispersion values, for which there is no sign of CO convergence.

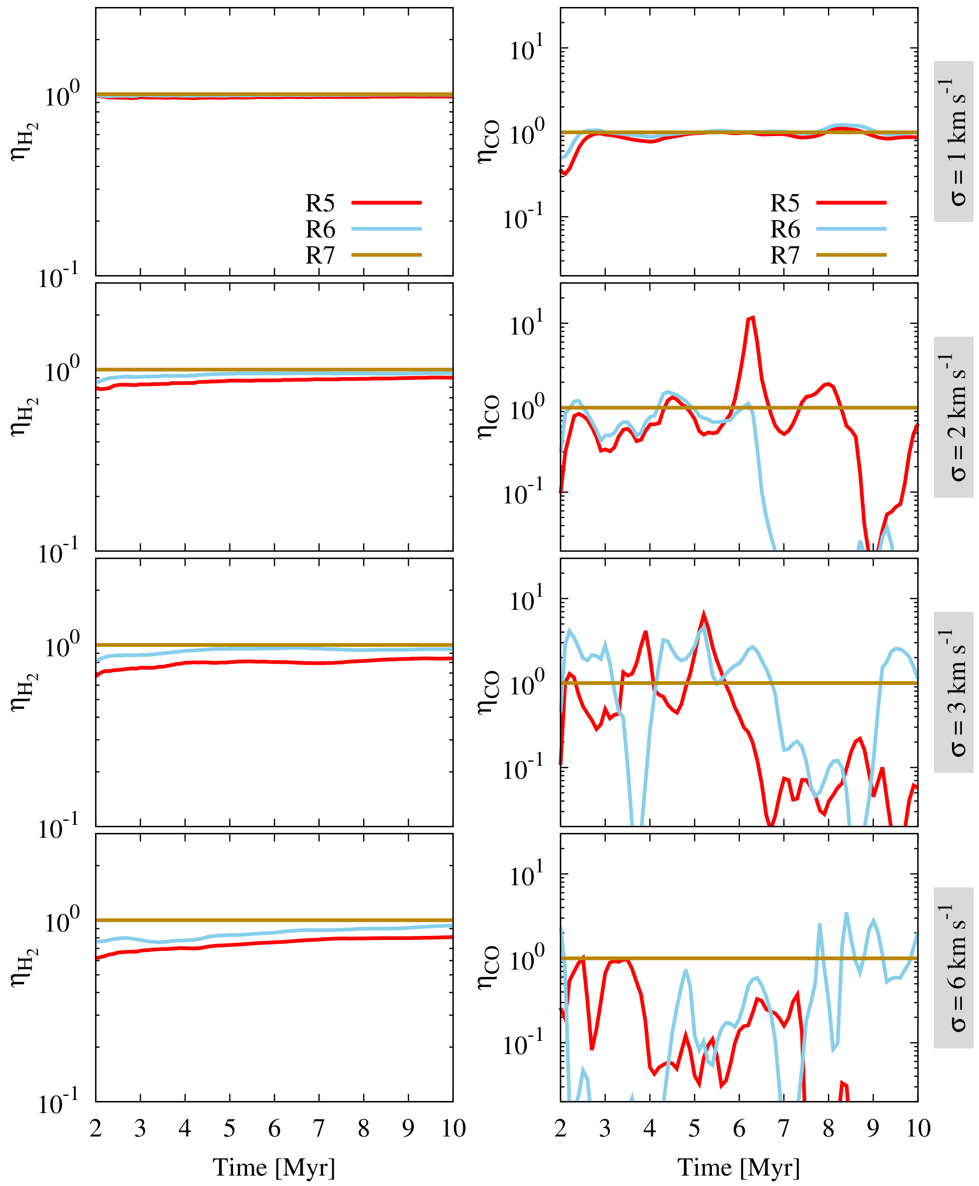

Figure 39: The evolution of η_{H_2} (Equation 7.4) and η_{CO} (Equation 7.7) for the TB runs with various strengths of the supersonic turbulence (runs TB-R[5,6,7]-n030-v[1,2,3,6], see Table 5). As the 3D velocity dispersion increases, η_{H_2} quickly deviates from $\eta_{\mathrm{H}_2} = 1$. The CO formation is even more sensitive to the increase in the velocity dispersion of the gas.

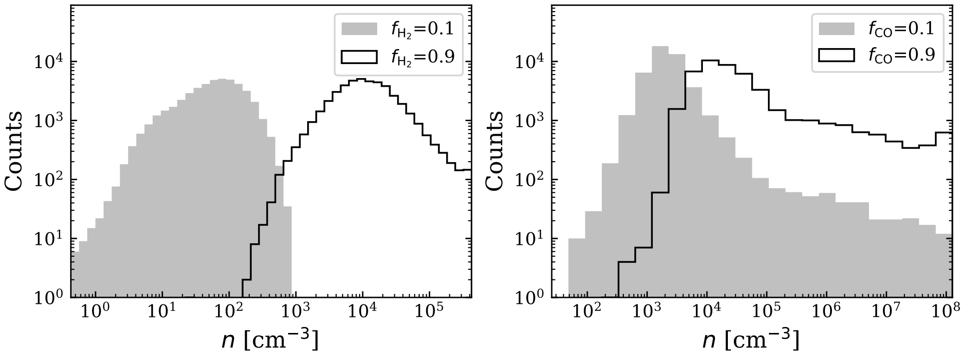

Figure 40: Left: The distribution of the density of fluid elements when they have recently begun to form H_2 ($f_{H_2} = 0.1$, filled histogram) and when almost all of the H in the fluid element is converted to H_2 ($f_{H_2} = 0.9$, not filled). Right: same for CO formation. The peak of the distribution for $f_{H_2} = 0.1$ is $n \sim 100$ cm^{-3} and for $f_{CO} = 0.1$ is $n \sim 2 \times 10^3$ cm^{-3}.

10.5 | TIME EVOLUTION OF A FLUID ELEMENT

The cells satisfying the dynamical condition (Equation 9.11) will form molecules "instantaneously", i.e. within one hydro-dynamical step. The cells that do not satisfy the dynamical condition, however, need a greater scrutiny in the simulations. It is unnatural to assume that the molecule formation in a cell starts from scratch in each time-step. Instead, the fluid element entering a cell might already be partially molecular. For this fluid element, either the molecule formation is supported or dissociation might begin, depending on the physical properties of the cell. It is not possible to explain this scenario simply via one time snapshot of the simulation. Thus, in order to determine the average time needed for the formation or dissociation of molecules in a dynamical environment, it is necessary to follow the evolution of fluid elements in time.

The implementation of tracer particles in the high resolution CF-R10-tracer run can be used to test the validity of the theoretical arguments made in Chapter 9. In this run with spatial resolution $\Delta x = 0.008$ pc, the evolution of H_2 and CO is converged; the chemistry and dynamics in both the diffuse and dense regions are resolved. The tracer particles are injected into the simulation domain to follow the evolution of the fluid elements that transform from the WNM phase to the MC phase. They contain information of not only the position and velocity of the fluid elements but also their thermodynamical and chemical properties at each point in time.

The molecular content of a fluid element is given by the mass-fraction of the molecule (Equations 7.2 and 7.5). The left panel of Figure 40 shows the distribution of the gas density at which H_2 formation has recently begun in a fluid element ($f_{H_2} = 0.1$, filled histogram) and the density at which the same fluid element later becomes almost fully molecular ($f_{H_2} = 0.9$, not filled). H_2 formation begins in a broad range of gas densities, anywhere between 1 and 1000 cm^{-3}, with a peak for $f_{H_2} = 0.1$ at $n \sim 100$ cm^{-3}. The range of densities at which the fluid ele-

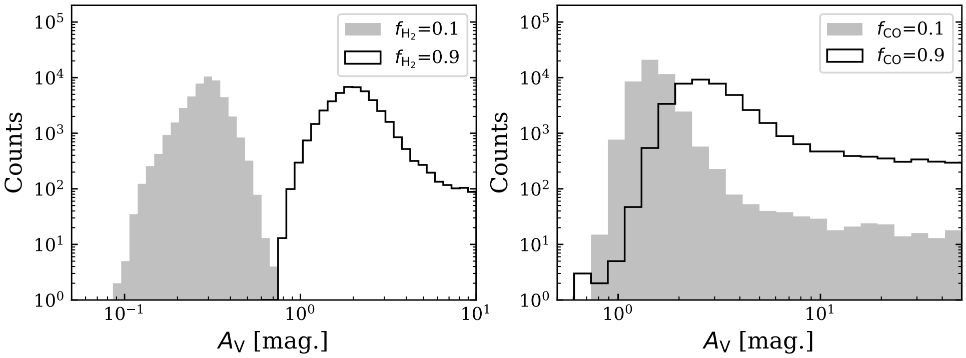

Figure 41: Left: the distribution of the A_V experienced by fluid elements at which they begin to form H_2 ($f_{H_2} = 0.1$, filled histogram) and when most of the H in the fluid element is converted to H_2 ($f_{H_2} = 0.9$, not filled). Right: same for CO formation. The peak of the distribution for $f_{H_2} = 0.1$ is $A_V \sim 0.3$ and for $f_{CO} = 0.1$ is $A_V \sim 2$.

ments reach $f_{H_2} = 0.9$ is also quite broad; some fluid elements have $f_{H_2} = 0.9$ at $n \sim 100$ cm^{-3} while some become almost fully molecular only for $n > 10^5$ cm^{-3}. The right panel shows the similar density distribution for in case of CO evolution. The formation of CO begins at all densities above 100 cm^{-3}, with a peak at $n \sim 2 \times 10^3$ cm^{-3}. Most of the fluid elements become molecular in CO ($f_{CO} = 0.9$) at $n \sim 10^4$ cm^{-3}.

Figure 41 shows the distribution of mean A_V experienced by a fluid element when molecule formation begins and when it is close to becoming fully molecular. The left panel shows that the majority of the fluid elements start H_2 formation in regions with $A_V \sim 0.3$ and become largely molecular at $A_V \sim 2$. The right panel shows that rapid CO formation sets in at A_V between 1 and 3. This is consistent with the findings by Röllig et al. (2007); Clark et al. (2012b); Gong et al. (2018), and resembles the distribution of A_V seen in Figures 34 and 35.

VALIDITY OF THE FITTED MOLECULE FORMATION TIME

The histograms in Figure 42 show the distribution of the time required by the fluid elements to become molecular, i.e. for the transition $f_{H_2} = 0.1 \rightarrow 0.9$ in the left panel and for the transition $f_{CO} = 0.1 \rightarrow 0.9$ in the right panel. In other words, these are the distributions of the H_2 and CO formation time-scale in the simulation. The large spread in the transition time for $f_{H_2} = 0.1 \rightarrow 0.9$ corresponds to the broad ranges of densities at which $f_{H_2} = 0.1$ and $f_{H_2} = 0.9$ are reached in Figure 40. The peak of the H_2 formation time in the gas is $\sim$ 10 Myr, which is in good agreement with the formation time given by Equations 3.7 and 9.18 for the gas at density $n \sim$ 100 cm^{-3} (peak of the density distribution in Figure 40).

The broad distribution of the transition time $f_{CO} = 0.1 \rightarrow 0.9$ in the right panel shows that once the CO formation begins, the fluid elements undergo the transition anywhere between 0.1 and 4 Myr. For comparison, the CO formation time given by Equation 9.25 is 2.5 Myr for the gas with $n = 2 \times 10^3$ cm^{-3} (peak of the density distribution in Figure 40). Therefore, the power-law fits (Equations 9.18 and 9.25) obtained from a snapshot of the simulation are good approximations of

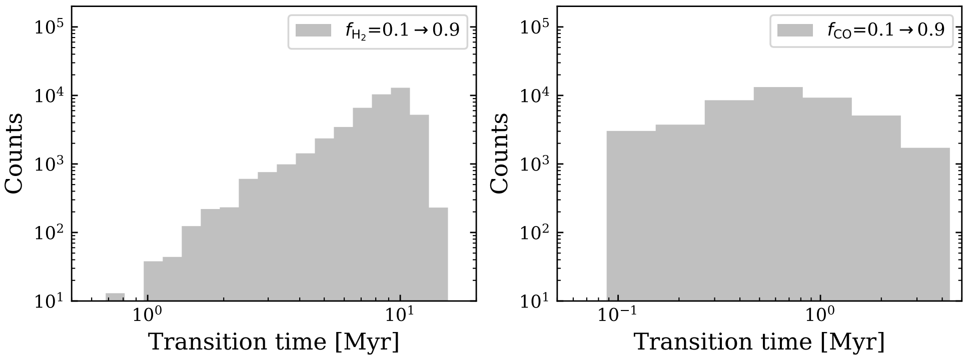

Figure 42: The distribution of the time taken by the tracer particles to become molecular (left: for H_2 and right: for CO). The peak of the time taken in case of H_2 formation is $\sim$ 10 Myr and in case of CO formation is $\sim$ 1 Myr.

the molecule formation time-scales for an average fluid element evolving in time. A detailed study of the molecule formation time for each tracer particle reveals if the fits are representative of all fluid elements in the simulation; this is however out of the scope of the thesis.

10.6 | FLUID ELEMENT THROUGH A REGION

In the formulation of the dynamical condition (Equation 9.11), the time taken by the fluid element to cross a computational cell was compared against the molecule formation time; this provides a strict constraint on the resolution requirement. However, the properties of the gas in a simulation do not change strictly on a cell-by-cell basis. For instance, the gas density or A_V can remain similar in a region that spans multiple computational cells, as shown in the cartoon in Figure 43. The time taken to cross the region $t_{\rm region,cross}$ is usually longer than the typical cell-crossing time $t_{\rm cell,cross}$ (Equation 9.12). In such a scenario, the resolution criteria determined from the dynamical condition can be relaxed, since fluid elements with lower gas densities can also become fully molecular within this longer time-scale.

In principle, the size of the region is required to calculate $t_{\rm region,cross}$, which can be cumbersome and in fact, unrealistic. Fortunately, with the help of tracer particles, the value of $t_{\rm region,cross}$ can be easily determined by recording the total time spent by particles in a certain A_V range, before leaving the region. Figure 44 shows the average time spent by tracer particles in regions with various A_V values. The peak at low $A_V = 0.02$ refers to the time spent by the fluid elements as low density WNM that flow from the x–boundaries towards the collision interface in the CF-setup. As the fluid elements travel into denser regions with higher A_V, they spend less than 1 Myr in each A_V range. The typical A_V in regions where H_2 and CO formation begin are shown in Figure 41. On average, the fluid elements remain in regions with $A_V = 0.3$ (H_2 forming regions) for $\sim$ 0.6 Myr and in regions with $A_V = 2$ (CO forming regions) for $\sim$ 0.2 Myr.

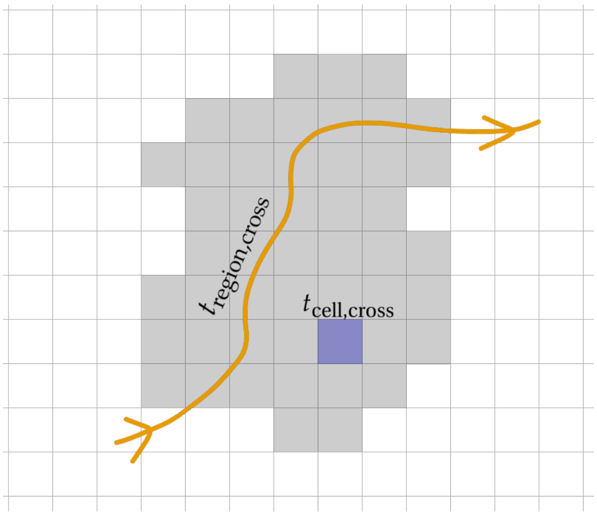

Figure 43: A cartoon of the trajectory of a fluid element crossing a region with a constant A_V and/or density (shown as the dark region). The time taken by a fluid element to cross this region is longer than the time taken to cross a computational cell (shown in blue). The longer time helps to relax the resolution criteria for molecule formation.

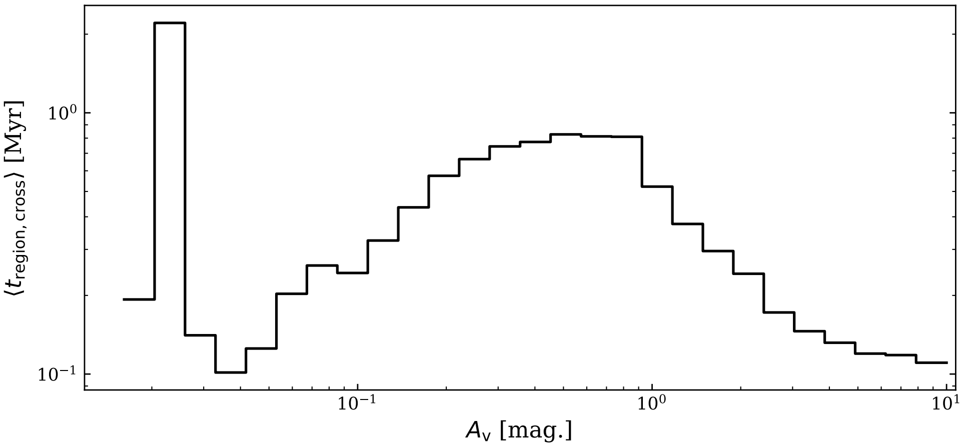

Figure 44: The average time spent by tracer particles (i.e. $t_{\text{region,cross}}$) in different A_V intervals. The peak at low A_V refers to the tracers in the stable WNM. As the fluid elements are advected to denser regions with high A_V, they generally spend less than 1 Myr in each A_V interval.

THE RELAXED RESOLUTION REQUIREMENT

In the CF setup, the H_2 formation is converged for the CF-R6 run with $\Delta x = 0.125$ pc and CO formation is converged for the CF-R8 run with $\Delta x = 0.032$ pc. For $\langle\sigma\rangle_{\rm mass} = 2\,{\rm km\,s^{-1}}$ in the CF setup (see Figure 28), the cell-crossing times (Equation 9.12) are $t_{\rm cell,cross} \sim 0.06$ Myr and ~ 0.02 Myr for H_2 and CO, respectively. The corresponding average region-crossing times, determined above, are 10 times longer. This means, the minimum density that the simulations need to resolve, following to the "realistic" dynamical condition with $t_{\rm region,cross}$ instead of $t_{\rm cell,cross}$, is 10 times lower. Equation 9.20 implies that simulations with ~ 3 times lower resolution can resolve this lower density. This explains why the H_2 formation in CF-R4/CF-R5 runs and CO formation in CF-R6/CF-R7 runs are quite close to convergence. Therefore, if only the total molecular content is of interest, the typical region-crossing time can be implemented to accept the weak convergence from simulations that have lower resolutions. However, the cell-crossing time should be considered for the convergence of not only the total H_2 and CO content, but also the 3D distribution of the molecules in the simulation domain.

10.7 | CHAPTER SUMMARY

In this chapter, the resolution requirements for converged molecule formation, derived in the previous chapter, were scrutinized. A case in which the physical condition required stronger resolution criteria for converged CO formation due to short CO photo-dissociation time-scale was presented. A general expression for the density criteria arising from the physical condition, that exhibits the sensitivity of the resolution requirement on the shielding properties of the gas, was presented. The effect of velocity dispersion on the resolution requirement, as predicted by Equations 9.22 and 9.28, was confirmed. The possible shortcomings in the determination of the molecule formation and dissociation times, via the density distribution the gas at the end of the simulation, were investigated. The derived resolution criteria were found to be consistent with the results obtained from the time-evolution of fluid elements. Finally, a possibility to relax the resolution criteria by considering a more realistic view of a fluid element traveling through the simulation domain was presented.

11 | Formation of MC cores

This chapter presents MC cores that form self-consistently from the gas whose dynamical and chemical evolution is converged. In the inner regions of the molecular clouds, $n \gtrsim 10^5$ cm^{-3} is easily reached. These high-density regions can be 0.1 – 2 pc in size and have masses of $10 - 10^3 M_{\odot}$. Such regions are generally referred to as massive MC cores; they are different from the protostellar cores which are < 0.1 pc in size and have only up to $10_{\odot}$ in mass.

In Section 11.1, four massive MC cores formed in the MCs of the colliding flow setup are described and general properties of the cores are listed. In Section 11.2, the mechanism of gas accretion from the molecular cloud onto the cores (or cluster of cores) is studied. The investigation is limited to the accretion of gas at parsec scales to determine whether the surrounding gas flows into the MC cores predominantly through selected channels or via radial collapse.

11.1 | IDENTIFICATION OF MC CORES

The dense structures in the CF-R10-tracer run are resolved with a spatial resolution of $\Delta x = 0.008$ pc. Since MC cores are typically $\lesssim 0.1$ pc in size, they are still not well-refined in the CF-R10-tracer run for an investigation of their internal dynamics. However, the resolution is sufficiently high to study the accretion of gas from the parent MC onto these cores. The gas accretion is followed by using tracer particles. Figure 45 shows the evolution of mass-weighted mean number density of the gas for the CF-R10-tracer run. For the first 17 Myr, the mean density is < 100 cm^{-3} and shows a slow increase. The formation of molecular cloud cores is indicated by the rapid rise of mean gas density between 17 and 18 Myr. The increase in mean density due to gas accretion onto the cores continues after 18 Myr, but at a slower rate.

The positions of cores at the end of the simulation are identified with a simple search for the local minimum of the gravitational potential in a subset of the computational domain containing high column density regions. Figure 46 shows the column density of the total gas in the CF-R10-tracer run at the end of the simulation. The left panel shows the gas column integrated along the y–direction. Filamentary structures, that are stretched along the direction of flow (x-axis), are formed near the collision interface. The location of four cores, that are identified as described above, are denoted by black circles. The radii of the circles are the actual radii of spherical surface considered around the cores to study the accretion process. The right panel shows the gas column integrated along the x–direction. There

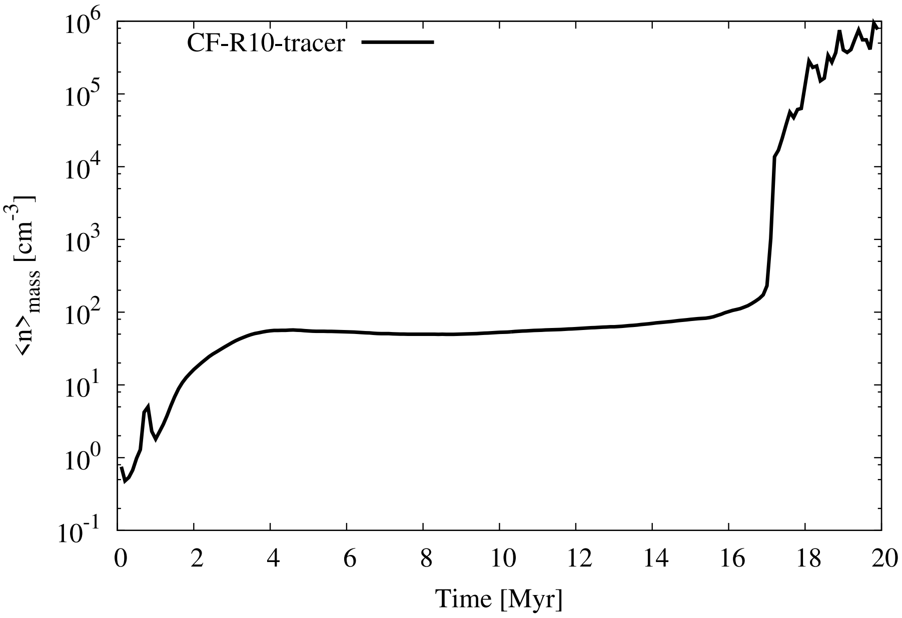

Figure 45: The evolution of the mass-weighted mean number density of the gas in the CF-R10-tracer run. The formation of MC cores is evident from the drastic increase in the mean density after $t = 17$ Myr.

are numerous regions of high column density, formed all over the dense cloud near the collision interface. In this thesis, only four of them are considered.

The properties of these cores are listed in Table 6. Cores 1 and 2 are isolated while Cores 3 and 4 are clusters of multiple cores. Core 2 is very close to Core 3; in fact, it is a core located in one of the filaments that meet at the “hub" which is Core 3. In the third column, the radius R of the “sphere of influence" around each core is given. The spheres for isolated cores are naturally smaller than those for the cluster of cores. These spherical volumes are chosen such that the core or the cluster of cores are completely incorporated. At this scale, the accretion from the parent MC is not affected by the internal dynamics of the core. The total mass of gas M contained in the sphere around each core is given in the fourth column. Note that this mass is much larger than the actual mass of the core at the centre of the sphere. For instance, the dense gas ($n > 10^5$ cm^{-3}, see Section 2.4) of Core 1 contains $\sim 33 M_\odot$. The mean density of the gas in the spherical volume is given in the fifth column, and the $t_{\rm ff}$ in the sixth column denotes the corresponding free-fall time (Equation 2.7). The free-fall velocity $v_{\rm ff}$ is given by

$$v_{\rm ff} \lesssim \sqrt{\frac{GM}{R}}\,. \tag{11.1}$$

Finally, the last column shows the number of tracer particles that have entered the spherical volume by the end of the simulation and that have been marked to follow the journey from the parent cloud to the core.

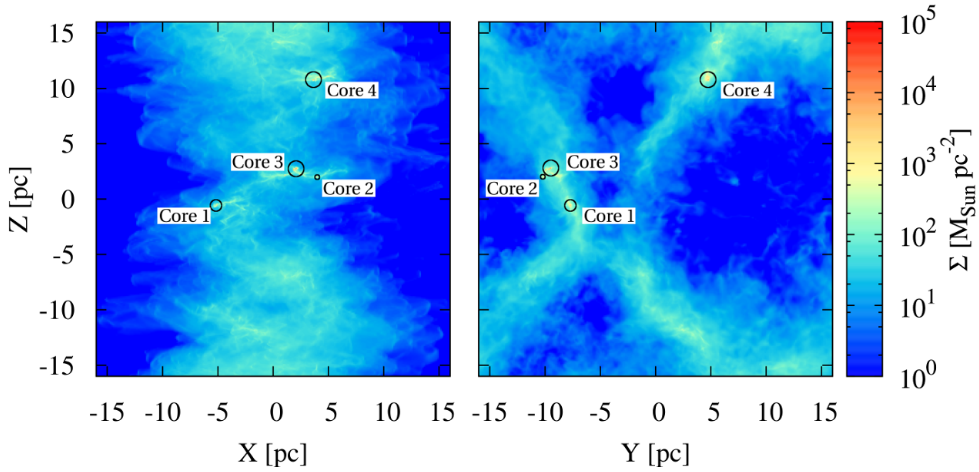

Figure 46: The column densities of the total gas in the CF-R10-tracer run, integrated along the y-direction (left) and along the x-direction (right). The black circles denote the position and size of four molecular cloud cores listed in Table 6.

Table 6: The identified MC cores in the CF-R10-tracer simulation. The type of the core is given in the second column. R, M, and $\langle n \rangle$ denote respectively, the radius, total mass, and the mean number density of the spherical volume considered around the core. The free-fall time (t_{ff}) and velocity (v_{ff}) are given in the sixth and seventh column, respectively. The last column lists the number tracer particles that are in the spherical volume at the end of the simulation and whose trajectories are followed.

Name	Type	R [pc]	M [$M_\odot$]	$\langle n \rangle$ [cm^{-3}]	t_{ff} [Myr]	v_{ff} [km s^{-1}]	# particles
Core 1	Isolated	0.5	66	2.2×10^3	0.9	0.7	20114
Core 2	Isolated	0.2	27	1.4×10^4	0.4	0.7	9114
Core 3	Cluster	0.7	269	3.2×10^3	0.8	1.3	77050
Core 4	Cluster	0.7	155	1.8×10^3	1	0.98	34182

11.2 | ACCRETION ONTO THE CORES

In order to determine the nature of gas-accretion, the trajectory of all the tracer particles associated with the cores, listed in Table 6, are extracted. The evolution of the particles are followed starting at 17 Myr. When these particles reach the surface of the sphere around the core, their angular coordinates (the azimuthal angle ϕ and the polar angle θ) are measured at the centre of the core. Note that the motion of the core itself is also tracked to determine these angles. In addition to the angles, the densities of the particles are noted and their radial infall velocity towards the core are calculated. As more and more tracers enter the sphere of influence around the core during the 3 Myr evolution (17–20 Myr), a distribution of the direction, density, and infall velocity of the accreting gas is obtained.

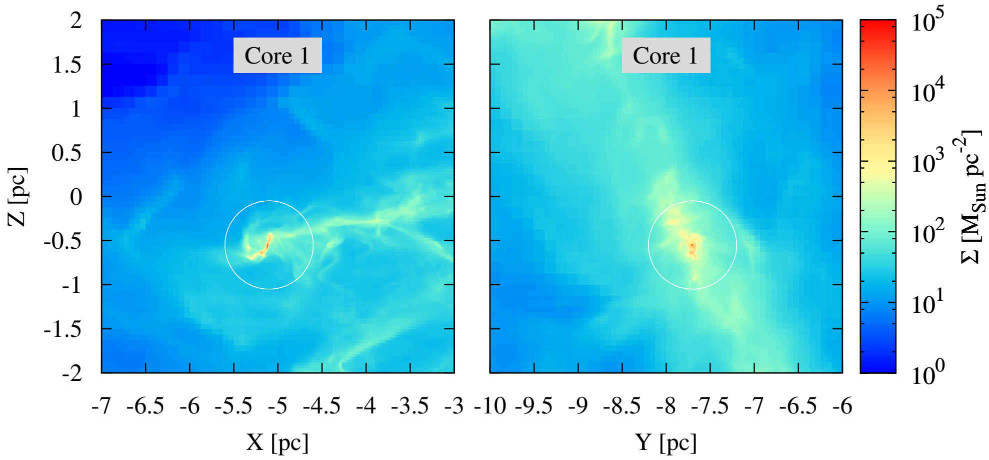

(a) The column densities of Core 1, integrated along the y-direction (left) and along the x-direction (right). The white circles denote the spherical surface of radius 0.5 pc at which the information of tracer particles are recorded as they accrete onto the core.

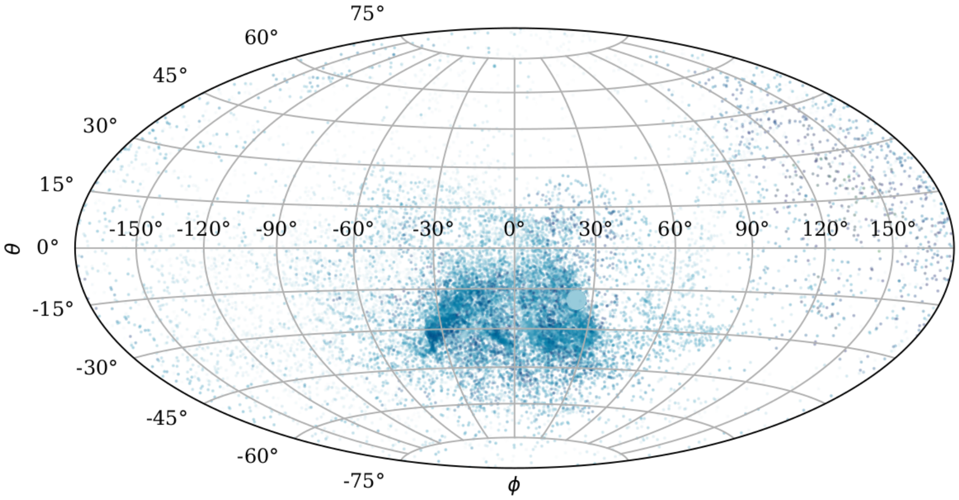

(b) The Hammer projection to visualize the accretion of gas by Core 1. The size of the marker increases with increasing density of the infalling gas. Similarly, darker regions denote infalling gas with higher velocities.

Figure 47: The gas-accretion in Core 1. (a) The column density maps show how the core is embedded in the dense regions of the CF setup. (b) The Hammer projection shows the core accretes high-density and high-velocity gas through one specific direction. Isotropic accretion is not observed.

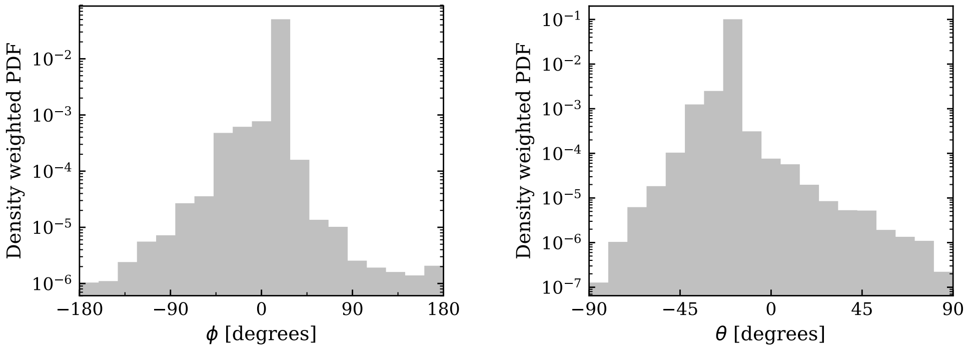

(a) The density weighted PDFs of the azimuthal angle (ϕ, left) and the polar angle (θ, right) at which the tracer particles enter Core 1.

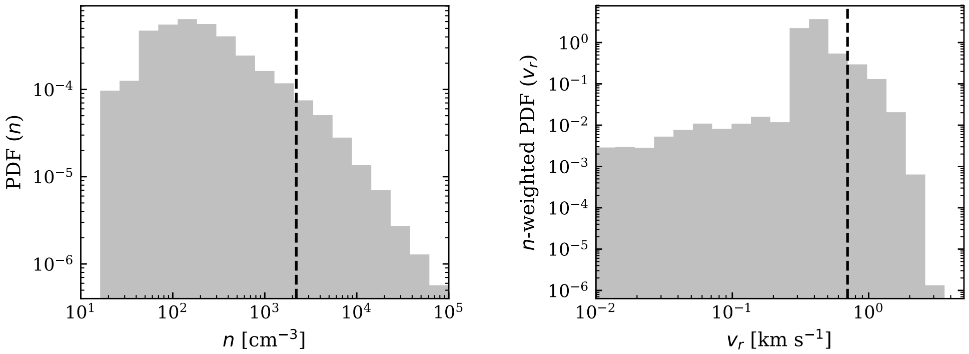

(b) Left: the PDF of the number density of fluid elements entering Core 1. The dashed line denotes the mean density of the sphere considered for the core. Right: the density-weighted PDF of the radial infall velocity of the fluid elements. The dashed line marks the free-fall velocity at the surface of the sphere around the core.

Figure 48: The gas-accretion in Core 1. (a) The PDFs of the angular coordinates show that there is one preferred direction of gas-accretion onto the core. (b) Most of the fluid elements being accreted onto the core have $n \sim 100\ \mathrm{cm}^{-3}$ and most of the dense gas is falling into the core with a velocity close to the free-fall velocity of $v_{\mathrm{ff}} = 0.7\,\mathrm{km\,s}^{-1}$.

CORE 1

Figure 47(a) shows the column density projections of the isolated Core 1 (left: integrated along y–axis, right: integrated along x–axis). The white circles denote the spherical surface at which the particles entering the core are investigated. From the two column density maps, it can be inferred that the core accretes from one specific direction. However, this is not so obvious since the column density maps contain the information of all the gas along the direction of integration in the computational domain. Figure 47(b) shows the Hammer projection to visualize the 3D gas accretion onto the core, inspired by the usage of this projection for the study of collapsing protostellar cores in Smith et al. (2011). The size of the markers increases with the density of the fluid element approaching the core, while the darkness of the markers increases with the radial infall velocity measured at the surface of the sphere. It is obvious that the high-density and fairly high-velocity gas is being accreted onto Core 1 along one particular direction ($\phi \in [-30°, 30°]$ and $\theta \in [-45°, -15°]$). This corresponds to the filamentary structure reaching the core from right side in the first panel of Figure 47(a).

The density-weighted PDFs of the two angular coordinates in Figure 48(a) display one prominent peak in each distribution, further constraining the dominant direction of accretion.

In Figure 48(b), the PDF of the number density of the fluid elements accreting onto the core is shown in the left panel. The dashed line denotes the mean density of the core at the end of the simulation, which is an order of magnitude higher than the peak of the density distribution ($n \sim 100\ \mathrm{cm}^{-3}$). The core is also accreting some high density gas at $n \sim 10^4 - 10^5\ \mathrm{cm}^{-3}$ along the filamentary structure. It is important to note that the density at the central region of the core is orders of magnitude higher than the mean density displayed here. For instance, the mass-weighted mean density of the core enclosed in the sphere is $\langle n \rangle_{\mathrm{mass}} = 2.8 \times 10^6\ \mathrm{cm}^{-3}$. The right panel of Figure 48(b) shows the density-weighted PDF of the radial infall velocity v_r of the gas reaching the spherical surface around Core 1. The vertical dashed line denotes the free-fall velocity (v_{ff}, Equation 11.1). Most of the dense gas approach the core with velocity similar to $v_{\mathrm{ff}} = 0.7\ \mathrm{km\,s^{-1}}$.

CORE 2

Figure 49(a) shows the close-up of the isolated Core 2, located in a filament leading up to the hub containing Core 3. A spherical surface with 0.2 pc radius is indicated by the white circles around the core. Figure 49(b) shows the corresponding Hammer projection for the core. Similar to Core 1, there is a distinct direction of the accretion of high-density and high-velocity gas onto the core. The PDFs of the angular coordinates in Figure 50(a) constrain the single prominent direction at $\phi \in [-120°, -90°]$ and $\theta \in [45°, 60°]$. The lack of two channels of accretion means that the core is not able to accrete the dense gas that flow past Core 2 and towards Core 3 along the filament.

The left panel of Figure 50(b) shows the PDF of density of the accreting gas. This is similar to the density PDF in Figure 48(b). However, the core is mostly accreting slightly denser gas ($n \sim 200 - 300\ \mathrm{cm}^{-3}$) and the mean density of the core is $n \sim 10^4\ \mathrm{cm}^{-3}$. The PDF of infall velocity in the right panel shows that most of the dense gas approach the core with $v_r \sim 0.5\ \mathrm{km\,s^{-1}}$, which is lower than $v_{\mathrm{ff}} = 0.7\ \mathrm{km\,s^{-1}}$.

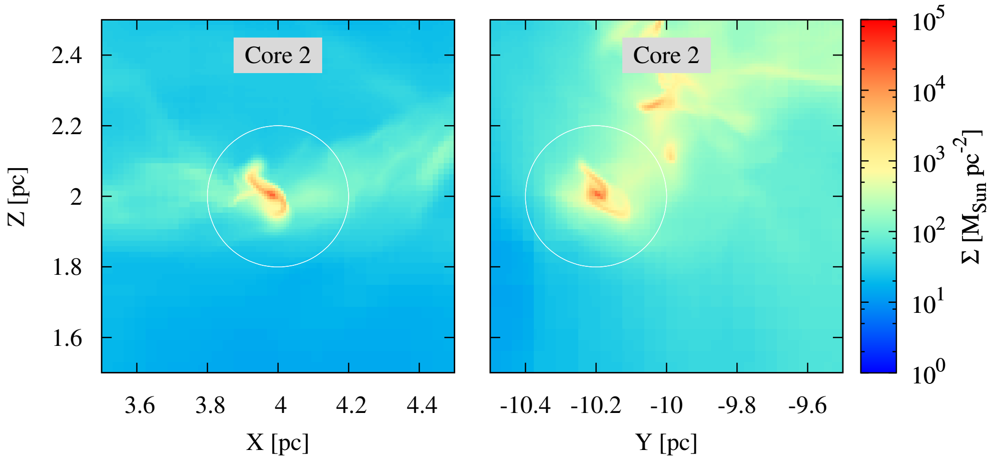

(a) As in Figure 47(a), now for Core 2. The white circles denote the spherical surface of radius 0.2 pc at which the information of tracer particles are recorded.

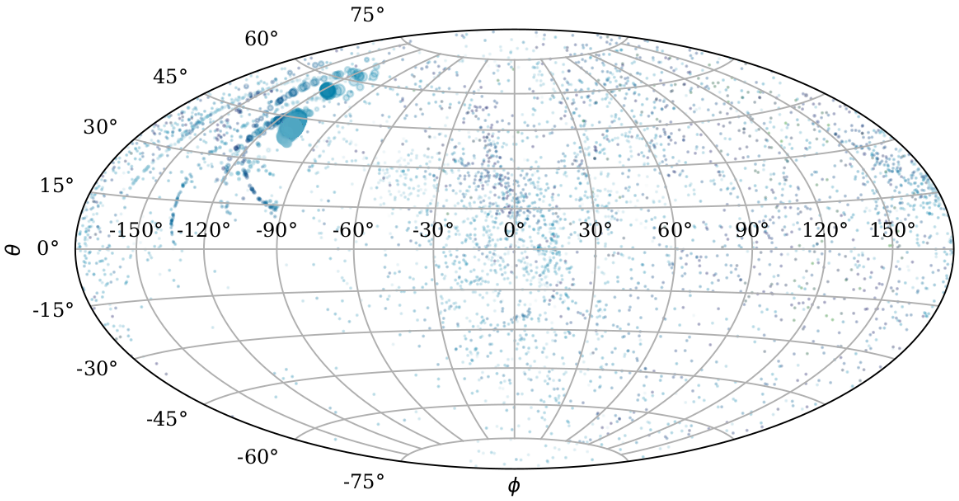

(b) The hammer projection to visualize the accretion of gas by Core 2.

Figure 49: The gas-accretion in Core 2. (a) The column density maps show that the isolated core is embedded in a single stretch of dense gas. (b) The hammer projection shows the core accretes high-density and high-velocity gas through one specific direction. Together, the maps imply that Core 2 is accreting some of the dense gas flowing along the filamentary structure towards Core 3.

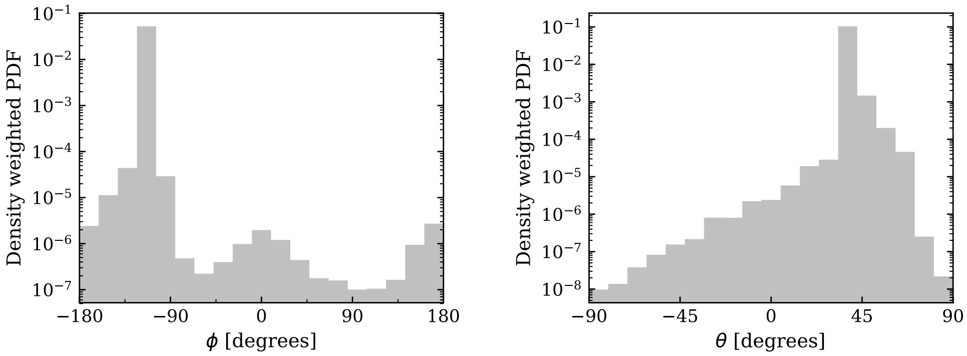

(a) As in Figure 48(a), now for Core 2.

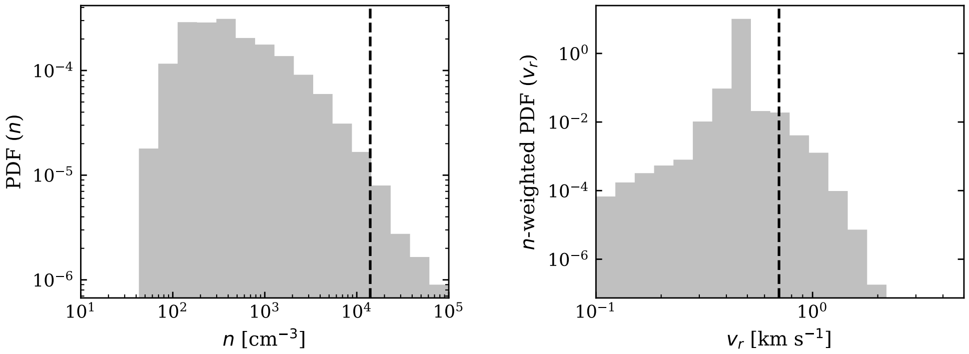

(b) As in Figure 48(b), now for Core 2.

Figure 50: The gas-accretion in Core 2. (a) The PDFs of the angular coordinates show that there is again one preferred direction of gas-accretion onto the core. (b) Most of the fluid elements being accreted onto the core have $n \sim 200 - 300\,\mathrm{cm}^{-3}$ and the majority of the dense gas approach the core with $v_r \sim 0.5\,\mathrm{km\,s}^{-1}$, slightly lower than the free-fall velocity of $v_{\mathrm{ff}} = 0.7\,\mathrm{km\,s}^{-1}$.

CORE 3

Figure 51(a) shows the close-up of the cluster of cores, that are altogether referred to as Core 3. In the multiple filamentary structures that are linked at Core 3, many small, individual cores are present. The spherical surface of radius 0.7 pc around the centre of the cluster incorporates all the major cores. It is difficult to estimate the channels of accretion from the column density projections alone, because of the complex network of the filamentary structures. The Hammer projection in Figure 51(b) shows a more extended accretion as compared to the individual cores 1 and 2. However, one prominent accretion channel of dense and high-velocity gas is again obvious. The distributions of the angular coordinates in Figure 52(a) constrain the azimuthal angle at $\phi \in [-30^\circ, 0^\circ]$ and $\theta \in [0^\circ, 30^\circ]$. Thus, it is likely that the two filamentary structures combine and reach the cluster of cores together through one channel.

Figure 52(b) shows that the density PDF in the left panel is surprisingly similar to the PDF obtained for isolated cores 1 and 2. A major difference is that the core is accreting a considerable amount of low density gas ($n \sim 10\ \mathrm{cm}^{-3}$) as well. Nevertheless, the peak of the PDF is at $n \sim 100\ \mathrm{cm}^{-3}$ and the mean density of the spherical volume incorporating multiple cores is an order of magnitude higher. The PDF of v_r in the right panel shows the dense gas accretes mostly at $v_r \sim v_{\mathrm{ff}} = 1.3\ \mathrm{km\,s}^{-1}$. This infall velocity is notably larger than the infall velocities seen for Cores 1 and 2. This is consistent with the results from Peretto et al. (2013) that massive cores (or clusters) formed at the filamentary hubs show larger infall velocities, compared to the infall velocities seen in individual cores.

CORE 4

Figure 53(a) shows Core 4, which is another cluster of cores. This cluster is part of a long *helical* chain of cores extended along the x–direction, as seen in the left panel. The spherical surface is centered on the heavy core, which is accreting mainly via the two azimuthal directions, that are well-separated from each other. The Hammer projection in Figure 53(b) shows that accretion from one channel is more prominent than the other. From Figures 53(b) and 54(a), it can be concluded that a majority of the accretion occurs at $\phi \in [0^\circ, 30^\circ]$ and $\theta \in [-60^\circ, -15^\circ]$. This direction corresponds to the filament reaching the core from the right in the first panel of Figure 53(a). For the channels reaching the core from the left, the polar angle has a broad distribution and no particular direction can be determined.

The PDF of density in the left panel of Figure 54(b) is similar to that of Core 3 (Figure 52(b)). The PDF of infall velocities is however, broad. The dense gas that reaches the cluster via different channels has velocity anywhere between 0.1 and $2\ \mathrm{km\,s}^{-1}$. Similar to Core 3, this cluster of cores also accretes gas with higher velocities than the isolated cores 1 and 2.

Overall, the nature of gas accretion onto the MC cores is in good agreement with the geometry of accretion onto the protostellar cores as presented by Smith et al. (2011). This similarity of accretion mechanism at ~ 1 pc scales of the MC cores with the $\lesssim 0.1$ pc scales of the protostellar cores is attributed to the self-similar nature of the molecular clouds. The larger radial infall velocities for massive cores is also in good agreement with the observational results from Peretto et al. (e.g. 2013). The lack of isotropic radial collapse suggests that the core is in its early stage of grav-

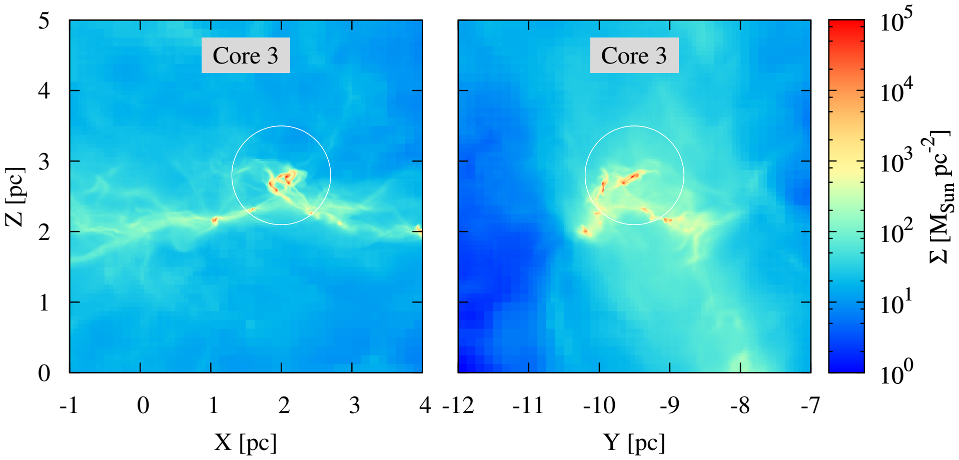

(a) As in Figure 47(a), now for Core 3. The white circles denote the spherical surface of radius 0.7 pc that incorporates multiple cores, and the collective accretion by all such cores is investigated.

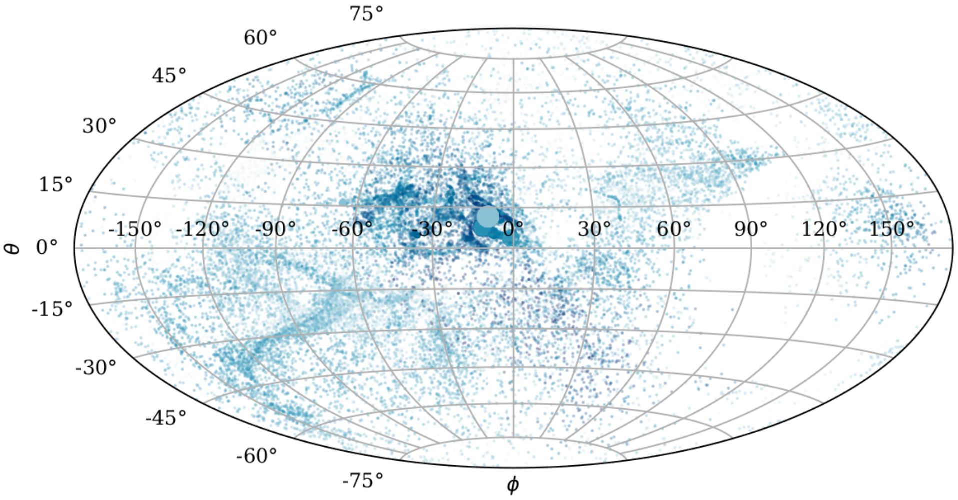

(b) The hammer projection to visualize the accretion of gas by Core 3.

Figure 51: The gas-accretion in Core 3. (a) The column density maps show multiple cores existing as a cluster and resembles a “hub" of filamentary structures. (b) The hammer projection shows that the cluster is accreting gas from multiple directions; however, there is again one prominent channel through which high-density and high-velocity gas reach the cluster.

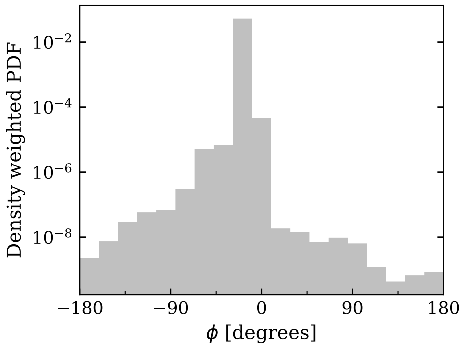

(a) As in Figure 48(a), now for Core 3.

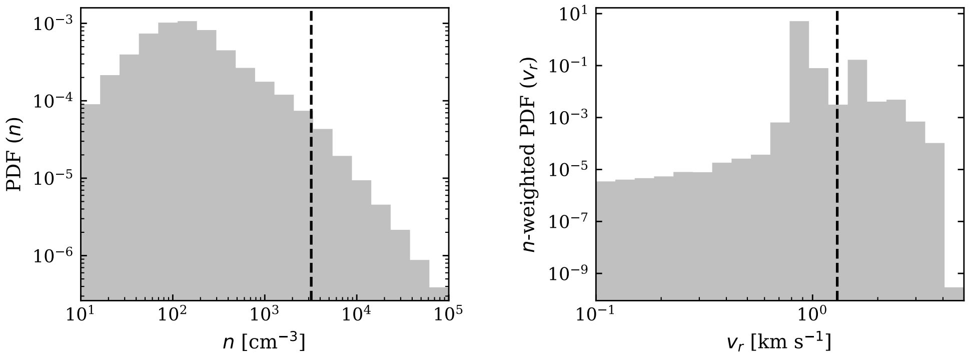

(b) As in Figure 48(b), now for Core 3.

Figure 52: (a) The PDFs of the angular coordinates show that there is one dominant channel of gas-accretion for the cluster of cores as well. (b) Most of the fluid elements being accreted onto the core have $n \sim 100\ \mathrm{cm}^{-3}$ and the infall velocity of most of the dense gas is similar to the free-fall velocity of $v_{\mathrm{ff}} = 1.3\ \mathrm{km\,s}^{-1}$.

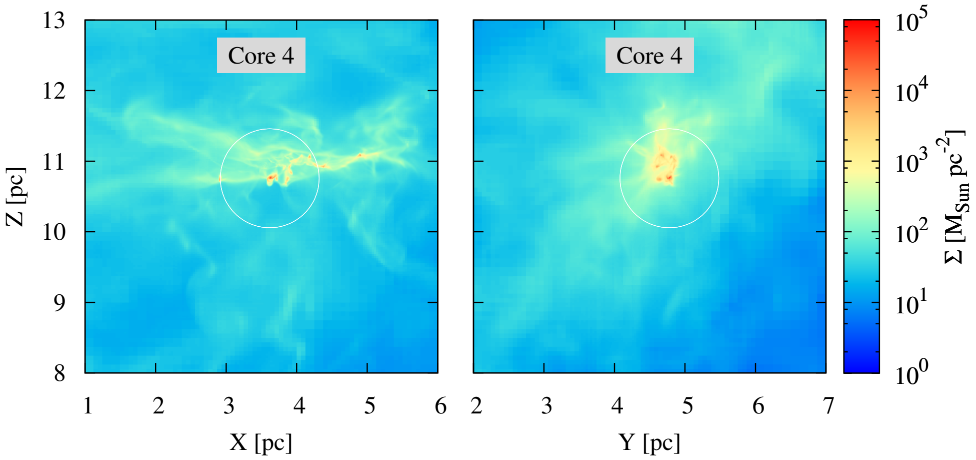

(a) As in Figure 47(a), now for Core 4. The radius of the spherical volume considered around this cluster of cores is 0.7 pc.

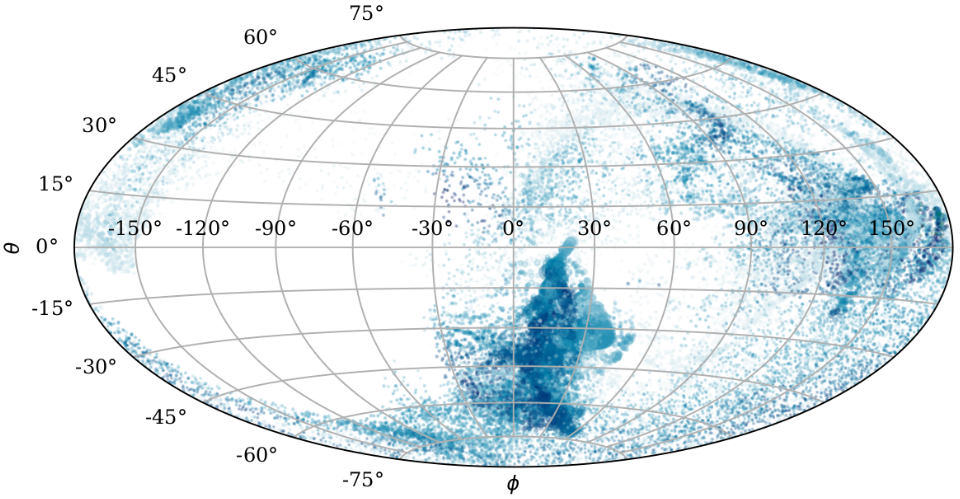

(b) The hammer projection to visualize the accretion of gas by Core 4.

Figure 53: The gas-accretion in Core 4. (a) The column density maps show that the cluster of cores is again a hub-structure at which multiple filaments meet. (b) The hammer projection shows the clustered core accretes high-density and high-velocity gas through one specific direction, although fairly significant accretion from other directions is also seen.

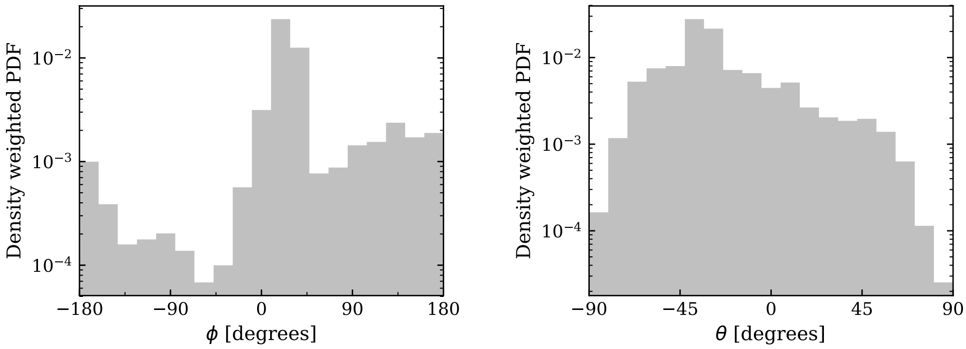

(a) As in Figure 48(a), now for Core 4.

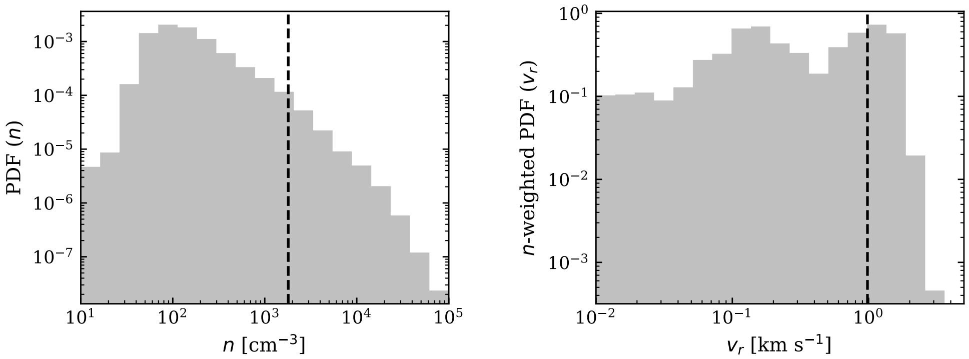

(b) As in Figure 48(b), now for Core 4.

Figure 54: The PDFs of the angular coordinates show that the cluster of cores have a prominent direction of accretion for the azimuthal angle ϕ. The polar angle θ, however, has a broad distribution, implying a slightly extended region of accretion. (b) The PDF of density of the fluid elements being accreted onto the core is similar to that of Core 3 in Figure 52(b) with the peak at $n \sim 100$ cm^{-3}. The infall velocity of the dense gas has a broad distribution suggesting the different channels of accretion have different typical infall velocities.

itational accretion, and the turbulent medium is facilitating the accumulation of dense gas via selected channels. This is in agreement with the findings by Weis et al. (in prep.) that the turbulent motions in molecular clumps, formed in MHD simulations of colliding flow, dominate over the gravitational accretion.

11.3 | CHAPTER SUMMARY

In this chapter, the formation of cores inside the molecular clouds was investigated in the high-resolution CF-R10-tracer run. A network of filamentary structures form in the MCs, and the filaments host multiple MC cores. From the nature of accretion of gas onto two isolated cores and two clusters of cores, it is concluded that the cores mainly accrete dense gas through designated channels, defined by the filamentary structures formed in the turbulent medium. As noted in observations, the massive cluster of cores were found to have larger infall velocities. The mechanism of accretion onto the MC cores is strikingly similar to the accretion process onto the protostellar cores at much smaller scales, consistent with the turbulent, hierarchical nature of molecular clouds.

12 | Conclusion

Recently, the inclusion of chemical networks has become more and more common in hydrodynamical simulations of the interstellar medium. However, a comprehensive study on the spatial resolution required to model different molecules is missing. For the investigation of such a resolution requirement, 3D hydrodynamic simulations coupled with a non-equilibrium chemistry network carried out using the MHD code FLASH (version 4.3) are presented in this thesis. For a self-consistent evolution of the formation of molecular clouds from the diffuse medium, the effects of gas self-gravity, turbulence, and diffuse radiative transfer are taken into account.

The chemical evolution under solar neighbourhood conditions is studied in two prevalent molecular cloud formation scenarios, (a) a turbulent periodic box and (b) a colliding flow. A large set of simulations with spatial resolution ranging from $\Delta x = 0.5$ pc to $\Delta x = 0.063$ pc for the turbulent box and up to $\Delta x = 0.008$ pc for the colliding flow simulations are performed. The investigation of the “convergence" is limited to the evolution of total H_2 and CO content in the simulations. For the turbulent box setup, the molecular cloud formation from the cold neutral medium with initial mean number densities of 3, 30, and 300 cm^{-3} is considered. For the colliding flow setup, the formation of molecular cloud from the diffuse warm neutral medium is followed. Finally, with the usage of tracer particles, the evolution of molecular cloud cores in a high-resolution colliding flow simulation is studied.

RESOLUTION REQUIREMENTS FOR MOLECULE FORMATION

In all simulations, the morphology of the gas changes significantly with increasing resolution on both small and large scales. Typically, molecules form initially more slowly in low resolution runs. After some time, however, large clumps of gas form at low resolutions whereas numerous smaller, filamentary structures form at high resolutions. The dust and molecular (self-)shielding become more effective in gaseous clumps if the turbulence in the cloud is not strong enough to destroy them. As a result, low resolution runs eventually produce more H_2 and CO than the higher resolution runs. The simulations suggest that the resolution required to obtain the convergence of *simple* quantities such as the total H_2 and CO content is high, even in quiescent environments subject to moderate levels of turbulence. It follows that more complex simulations with e.g. magnetic fields, stronger radiation fields, or stellar feedback mechanisms potentially demand an even higher spatial resolution for the convergence of various chemical species than the one derived here.

The derived resolution requirements follow from the understanding that the simulation needs to resolve typical densities at which (1) the molecule formation and the dissociation time scale are equal, which is referred to as a physical condition;

and (2) the molecule formation and the cell crossing time scale are equal, which is referred to as a dynamical condition. For the simulations presented in the thesis, the dynamical condition is usually found to be more restrictive than the physical condition for both H_2 and CO. It requires the simulation to resolve

$$n_{\mathrm{dyn,H_2}} \geq 10^{3.1}\ \mathrm{cm}^{-3} \left(\frac{\langle \sigma \rangle_{\mathrm{mass}}}{1\ \mathrm{km\ s}^{-1}} \right) \left(\frac{\Delta x}{1\ \mathrm{pc}} \right)^{-1} .$$

for converged H_2 formation and

$$n_{\mathrm{dyn,CO}} \geq 10^{3.7}\ \mathrm{cm}^{-3} \left(\frac{\langle \sigma \rangle_{\mathrm{mass}}}{1\ \mathrm{km\ s}^{-1}} \right) \left(\frac{\Delta x}{1\ \mathrm{pc}} \right)^{-1} .$$

for converged CO formation. The required spatial resolutions, corresponding to these densities, depend on the composition, temperature, and the strength of turbulence of the molecular cloud forming dense gas. In cases where the interstellar radiation field can penetrate deep within the cloud and readily destroy molecules, the physical condition is shown to be more restrictive. In particular, for the properties of the molecular cloud formed in the colliding flow setup presented here, the derived resolution requirements are

1. $\Delta x \lesssim 0.2$ pc to model H_2 formation
2. $\Delta x \lesssim 0.04$ pc to model CO formation

This is consistent with the numerical results of the colliding flow simulations; the total H_2 content is converged for a simulation with $\Delta x = 0.125$ pc and the total CO content is converged at $\Delta x = 0.032$ pc.

In the driven turbulent box simulations, in which the velocity dispersion of the gas in maintained at 10 km s^{-1}, neither the total H_2 content, nor the total CO content are converged when a spatial resolution up to $\Delta x = 0.063$ pc is used. The driven turbulence in warm atomic gas severely affects the evolutionary history of the H_2 and CO molecules because any dense region capable of sustaining the molecular gas is quickly disrupted. Similar to the colliding flow runs, the evolution of the CO content is more severely affected by the resolution. The mean velocity dispersion of the dense and molecular gas in the turbulent box simulations is 5 times larger than in the colliding flow simulation. Since the derived resolution requirement is inversely proportional to the mass-weighted velocity dispersion, a factor of 5 higher resolution would be required to model the converged formation of H_2 and CO.

The expressions for the resolution requirement are derived from the distribution of gas density and molecule formation/dissociation time-scales at the end of the simulation. They are found to be consistent with the results when the evolution of individual fluid elements are followed as they transition from the warm, atomic, and diffuse gas phase to the cold, molecular, and dense gas phase. Using the turbulent box simulations that allow to study the chemical evolution in controlled velocity dispersion of the dense gas, the dependence of the resolution criteria on the velocity dispersion is verified. Moreover, the formation and dissociation time-scales are determined via the limiting reactions of the molecules. Thus, a similar resolution criteria can be obtained for any chemical species in any chemical network. Since the limiting reactions for a chemical species do not vary across chemistry networks implemented in numerical modelling of molecular clouds, the resolution criteria derived here are valid for other chemistry networks as well.

FORMATION OF MOLECULAR CLOUD CORES

The formation of molecular clouds from the warm neutral medium in the high-resolution colliding flow simulation is chemically and dynamically resolved up to the scale of molecular cloud cores. The massive cores and cluster of cores are formed self-consistently in the network of filamentary structures in the molecular clouds. From the investigation of gas dynamics at parsec scales, these cores are found to accrete dense gas mainly through designated channels, defined by the filaments produced in the turbulent gas. Isotropic radial collapse of the dense gas onto the cores is rare.

13 | Prospects and Outlook

This thesis presents numerical models of molecular cloud formation in two controlled environments. The investigation of the convergence of chemical evolution was focused on the H_2 and CO formation. The same theoretical considerations can be easily extended to other chemical species included in the network. Furthermore, the derived resolution criteria depend on molecule formation/destruction time-scale, that are in turn determined by the limiting reactions included in the chemical network. If new limiting reactions are introduced, the relevant expressions for the required resolution can be easily updated to obtain the new resolution criteria.

The resolution requirement depends strongly on the composition, temperature, and the strength of turbulence of the MC forming dense gas. The validity of this relation has been investigated in this thesis. For a stronger proof, simulations of molecular cloud formation from a low-metallicity gas or with a stronger radiation field, for example, can be done. Similarly, the simulations presented in this thesis do not consider the effects of magnetic fields or stellar feedback mechanisms. These more complex, but realistic, scenarios influence not only the chemical reactions, but also the distribution of the chemical species in the ISM.

Recently, the cosmic ray ionization rates at high density regions are being revised (Padovani et al. 2018). This revision, along with the update to grain heating mechanisms by Ibáñez-Mejía et al. (2019) and to X-ray ionization effects by Mackey et al. (2018) also need to be considered to perform the CF setup with more accurate molecular cloud chemistry. They are responsible for increasing the dissociation rate of H_2 and CO in the cold, dense cloud, and are expected to make the physical condition more strict than presented in this thesis.

The formation of molecular clouds in the colliding flow setup presented in this thesis has already been used for further studies. Ibáñez-Mejía et al. (2019) studied the distribution of the dust charge in the multi-phase ISM modelled by the CF setup introduced here. The effects of magnetic field on the formation of dense molecular clumps in the CF setup is being investigated by Weis et al. (in prep). The column density distributions of gas and various chemical species in high resolution CF are being utilized by Franeck et al. (in prep) as a follow up to the study of the synthetic CII emission lines (Franeck et al. 2018).

Bibliography

Albertsson, T., Semenov, D. A., Vasyunin, A. I., Henning, T., & Herbst, E., New Extended Deuterium Fractionation Model: Assessment at Dense ISM Conditions and Sensitivity Analysis. 2013, The Astrophysical Journal Supplement Series, 207, 27

Aluie, H., Scale decomposition in compressible turbulence. 2013, Physica D Nonlinear Phenomena, 247, 54

Arzoumanian, D., André, P., Didelon, P., et al., Characterizing interstellar filaments with Herschel in IC 5146. 2011, A&A, 529, L6

Arzoumanian, D., André, P., Könyves, V., et al., Characterizing the properties of nearby molecular filaments observed with Herschel. 2019, A&A, 621, A42

Bakes, E. L. O. & Tielens, A. G. G. M., The Photoelectric Heating Mechanism for Very Small Graphitic Grains and Polycyclic Aromatic Hydrocarbons. 1994, ApJ, 427, 822

Ballesteros-Paredes, J., Hartmann, L., & Vázquez-Semadeni, E., Turbulent Flow-driven Molecular Cloud Formation: A Solution to the Post-T Tauri Problem? 1999, ApJ, 527, 285

Ballesteros-Paredes, J., Klessen, R. S., & Vázquez- Semadeni, E., Dynamic Cores in Hydrostatic Disguise. 2003, ApJ, 592, 188

Banerjee, R., Vázquez-Semadeni, E., Hennebelle, P., & Klessen, R. S., Clump morphology and evolution in MHD simulations of molecular cloud formation. 2009, MNRAS, 398, 1082

Barnes, J. & Hut, P., A hierarchical O(N log N) force-calculation algorithm. 1986, Nature, 324, 446

Bergin, E. A., Hartmann, L. W., Raymond, J. C., & Ballesteros-Paredes, J., Molecular Cloud Formation behind Shock Waves. 2004, ApJ, 612, 921

Bergin, E. A. & Tafalla, M., Cold Dark Clouds: The Initial Conditions for Star Formation. 2007, Annual Review of Astronomy and Astrophysics, 45, 339

Bisbas, T. G., Papadopoulos, P. P., & Viti, S., Effective Destruction of CO by Cosmic Rays: Implications for Tracing H_2 Gas in the Universe. 2015, ApJ, 803, 37

Black, J. H. & Dalgarno, A., Models of interstellar clouds. I. The Zeta Ophiuchi cloud. 1977, The Astrophysical Journal Supplement Series, 34, 405

Bonnor, W. B., Boyle's Law and gravitational instability. 1956, MNRAS, 116, 351

Burkert, A. & Lin, D. N. C., Thermal Instability and the Formation of Clumpy Gas Clouds. 2000, ApJ, 537, 270

Burton, M. G., Hollenbach, D. J., & Tielens, A. G. G. M., Line Emission from Clumpy Photodissociation Regions. 1990, ApJ, 365, 620

Campbell, J. L., Friesen, R. K., Martin, P. G., et al., Contraction Signatures toward Dense Cores in the Perseus Molecular Cloud. 2016, ApJ, 819, 143

Childs, H., Brugger, E., Whitlock, B., et al. 2012, in High Performance Visualization–Enabling Extreme-Scale Scientific Insight, 1st edn. (Chapman & Hall/CRC), 357–372

Clark, P. C., Glover, S. C. O., & Klessen, R. S., TreeCol: a novel approach to estimating column densities in astrophysical simulations. 2012a, MNRAS, 420, 745

Clark, P. C., Glover, S. C. O., Klessen, R. S., & Bonnell, I. A., How long does it take to form a molecular cloud? 2012b, MNRAS, 424, 2599

Courant, R., Friedrichs, K., & Lewy, H., On the Partial Difference Equations of Mathematical Physics. 1967, IBM Journal of Research and Development, 11, 215

Derigs, D., Winters, A. R., Gassner, G. J., & Walch, S., A novel high-order, entropy stable, 3D AMR MHD solver with guaranteed positive pressure. 2016, Journal of Computational Physics, 317, 223

DeZeeuw, D. & Powell, K. G., An Adaptively Refined Cartesian Mesh Solver for the Euler Equations. 1993, Journal of Computational Physics, 104, 56

Dobbs, C. L., Glover, S. C. O., Clark, P. C., & Klessen, R. S., The ISM in spiral galaxies: can cooling in spiral shocks produce molecular clouds? 2008, MNRAS, 389, 1097

Draine, B. T., Photoelectric heating of interstellar gas. 1978, ApJS, 36, 595

Draine, B. T. 2011, Physics of the Interstellar and Intergalactic Medium

Draine, B. T. & Bertoldi, F., Structure of Stationary Photodissociation Fronts. 1996, ApJ, 468, 269

Draine, B. T. & Lee, H. M., Optical Properties of Interstellar Graphite and Silicate Grains. 1984, ApJ, 285, 89

Duarte-Cabral, A., Acreman, D. M., Dobbs, C. L., et al., Synthetic CO, H_2 and H I surveys of the second galactic quadrant, and the properties of molecular gas. 2015, MNRAS, 447, 2144

Dubey, A., Fisher, R., Graziani, C., et al. 2008, in Astronomical Society of the Pacific Conference Series, Vol. 385, Numerical Modeling of Space Plasma Flows, ed. N. V. Pogorelov, E. Audit, & G. P. Zank, 145

Elmegreen, B. G. & Scalo, J., Interstellar Turbulence I: Observations and Processes. 2004, ARA&A, 42, 211

Federrath, C., On the universality of supersonic turbulence. 2013, MNRAS, 436, 1245

Federrath, C., Roman-Duval, J., Klessen, R. S., Schmidt, W., & Mac Low, M.-M., Comparing the statistics of interstellar turbulence in simulations and observations. Solenoidal versus compressive turbulence forcing. 2010, A&A, 512, A81

Field, G. B., Thermal Instability. 1965, ApJ, 142, 531

Field, G. B., Goldsmith, D. W., & Habing, H. J., Cosmic-Ray Heating of the Interstellar Gas. 1969, ApJ, 155, L149

Fogerty, E., Frank, A., Heitsch, F., et al., Molecular cloud formation in high-shear, magnetized colliding flows. 2016, MNRAS, 460, 2110

Franeck, A., Walch, S., Seifried, D., et al., Synthetic [C II] emission maps of a simulated molecular cloud in formation. 2018, MNRAS, 481, 4277

Frisch, U. 1995, Turbulence (Cambridge University Press)

Fryxell, B., Olson, K., Ricker, P., et al., FLASH: An Adaptive Mesh Hydrodynamics Code for Modeling Astrophysical Thermonuclear Flashes. 2000, ApJS, 131, 273

Gatto, A., Walch, S., Low, M.-M. M., et al., Modelling the supernova-driven ISM in different environments. 2015, MNRAS, 449, 1057

Gatto, A., Walch, S., Naab, T., et al., The SILCC project - III. Regulation of star formation and outflows by stellar winds and supernovae. 2017, MNRAS, 466, 1903

Genel, S., Vogelsberger, M., Nelson, D., et al., Following the flow: tracer particles in astrophysical fluid simulations. 2013, MNRAS, 435, 1426

Gingold, R. A. & Monaghan, J. J., Smoothed particle hydrodynamics - Theory and application to non-spherical stars. 1977, MNRAS, 181, 375

Girichidis, P., Walch, S., Naab, T., et al., The SILCC (SImulating the LifeCycle of molecular Clouds) project - II. Dynamical evolution of the supernova-driven ISM and the launching of outflows. 2016, MNRAS, 456, 3432

Glover, S. C. O. & Abel, T., Uncertainties in H_2 and HD chemistry and cooling and their role in early structure formation. 2008, MNRAS, 388, 1627

Glover, S. C. O. & Clark, P. C., Approximations for modelling CO chemistry in giant molecular clouds: a comparison of approaches. 2012, MNRAS, 421, 116

Glover, S. C. O., Federrath, C., Mac Low, M.-M., & Klessen, R. S., Modelling CO formation in the turbulent interstellar medium. 2010, MNRAS, 404, 2

Glover, S. C. O. & Mac Low, M.-M., Simulating the Formation of Molecular Clouds. I. Slow Formation by Gravitational Collapse from Static Initial Conditions. 2007a, ApJS, 169, 239

Glover, S. C. O. & Mac Low, M.-M., Simulating the Formation of Molecular Clouds. II. Rapid Formation from Turbulent Initial Conditions. 2007b, ApJ, 659, 1317

Glover, S. C. O. & Mac Low, M. M., On the relationship between molecular hydrogen and carbon monoxide abundances in molecular clouds. 2011, MNRAS, 412, 337

Gnat, O. & Ferland, G. J., Ion-by-ion Cooling Efficiencies. 2012, ApJS, 199, 20

Goldreich, P. & Kwan, J., Molecular Clouds. 1974, ApJ, 189, 441

Goldsmith, P. F. & Langer, W. D., Molecular cooling and thermal balance of dense interstellar clouds. 1978, ApJ, 222, 881

Goldsmith, P. F. & Li, D., H I Narrow Self-Absorption in Dark Clouds: Correlations with Molecular Gas and Implications for Cloud Evolution and Star Formation. 2005, ApJ, 622, 938

Gong, M., Ostriker, E. C., & Kim, C.-G., The X $_{CO}$ Conversion Factor from Galactic Multiphase ISM Simulations. 2018, ApJ, 858, 16

Gong, M., Ostriker, E. C., & Wolfire, M. G., A Simple and Accurate Network for Hydrogen and Carbon Chemistry in the Interstellar Medium. 2017, ApJ, 843, 38

Górski, K. M., Hivon, E., Banday, A. J., et al., HEALPix: A Framework for High-Resolution Discretization and Fast Analysis of Data Distributed on the Sphere. 2005, ApJ, 622, 759

Gould, R. J. & Salpeter, E. E., The Interstellar Abundance of the Hydrogen Molecule. I. Basic Processes. 1963, ApJ, 138, 393

Grassi, T., Bovino, S., Schleicher, D. R. G., et al., KROME - a package to embed chemistry in astrophysical simulations. 2014, MNRAS, 439, 2386

Habing, H. J., The interstellar radiation density between 912 A and 2400 A. 1968, Bull. Astron. Inst. Netherlands, 19, 421

Haid, S., Walch, S., Naab, T., et al., Supernova blast waves in wind-blown bubbles, turbulent, and power-law ambient media. 2016, MNRAS, 460, 2962

Heitsch, F., Naab, T., & Walch, S., Flow-driven cloud formation and fragmentation: results from Eulerian and Lagrangian simulations. 2011, MNRAS, 415, 271

Heitsch, F., Slyz, A. D., Devriendt, J. E. G., Hartmann, L. W., & Burkert, A., The Birth of Molecular Clouds: Formation of Atomic Precursors in Colliding Flows. 2006, ApJ, 648, 1052

Hennebelle, P. & Audit, E., On the structure of the turbulent interstellar atomic hydrogen. I. Physical characteristics. Influence and nature of turbulence in a thermally bistable flow. 2007, A&A, 465, 431

Hennebelle, P., Audit, E., & Miville-Deschênes, M.-A., On the structure of the turbulent interstellar atomic hydrogen. II. First comparison between observation and theory. Are the characteristics of molecular clouds determined early in the turbulent 2-phase atomic gas? 2007, A&A, 465, 445

Hennebelle, P., Banerjee, R., Vázquez-Semadeni, E., Klessen, R. S., & Audit, E., From the warm magnetized atomic medium to molecular clouds. 2008, A&A, 486, L43

Heyer, M. H. & Brunt, C. M., The Universality of Turbulence in Galactic Molecular Clouds. 2004, ApJ, 615, L45

Hollenbach, D. & McKee, C. F., Molecule formation and infrared emission in fast interstellar shocks. I. Physical processes. 1979, The Astrophysical Journal Supplement Series, 41, 555

Hollenbach, D. & McKee, C. F., Molecule Formation and Infrared Emission in Fast Interstellar Shocks. III. Results for J Shocks in Molecular Clouds. 1989, ApJ, 342, 306

Hollenbach, D. J., Werner, M. W., & Salpeter, E. E., Molecular Hydrogen in H i Regions. 1971, ApJ, 163, 165

Ibáñez-Mejía, J. C., Walch, S., Ivlev, A. V., et al., Dust charge distribution in the interstellar medium. 2019, MNRAS, 212

Jeans, J. H., The Stability of a Spherical Nebula. 1902, Philosophical Transactions of the Royal Society of London Series A, 199, 1

Joshi, P. R., Walch, S., Seifried, D., et al., On the resolution requirements for modelling molecular gas formation in solar neighbourhood conditions. 2019, MNRAS, 484, 1735

Jura, M., Interstellar clouds containing optically thin H_2. 1975, ApJ, 197, 575

Kennicutt, Jr., R. C., Keel, W. C., van der Hulst, J. M., Hummel, E., & Roettiger, K. A., The effects of interactions on spiral galaxies. II - Disk star-formation rates. 1987, AJ, 93, 1011

Keto, E. & Caselli, P., The Different Structures of the Two Classes of Starless Cores. 2008, ApJ, 683, 238

Klessen, R. S. & Glover, S. C. O., Physical Processes in the Interstellar Medium. 2016, Saas-Fee Advanced Course, 43, 85

Klessen, R. S. & Hennebelle, P., Accretion-driven turbulence as universal process: galaxies, molecular clouds, and protostellar disks. 2010, A&A, 520, A17

Konstandin, L., Shetty, R., Girichidis, P., & Klessen, R. S., Hierarchical Bayesian analysis of the velocity power spectrum in supersonic turbulence. 2015, MNRAS, 446, 1775

Körtgen, B. & Banerjee, R., Impact of magnetic fields on molecular cloud formation and evolution. 2015, MNRAS, 451, 3340

Koyama, H. & Inutsuka, S.-I., Molecular Cloud Formation in Shock-compressed Layers. 2000, ApJ, 532, 980

Koyama, H. & Inutsuka, S.-i., An Origin of Supersonic Motions in Interstellar Clouds. 2002, ApJ, 564, L97

Kritsuk, A. G., Norman, M. L., & Wagner, R., On the Density Distribution in Star-forming Interstellar Clouds. 2011, ApJ, 727, L20

Lada, C. J., Muench, A. A., Rathborne, J., Alves, J. F., & Lombardi, M., The Nature of the Dense Core Population in the Pipe Nebula: Thermal Cores Under Pressure. 2008, ApJ, 672, 410

Larson, R. B., Turbulence and star formation in molecular clouds. 1981, MNRAS, 194, 809

Lee, C. W., Myers, P. C., & Tafalla, M., A Survey of Infall Motions toward Starless Cores. I. CS (2-1) and N_2H^+ (1-0) Observations. 1999, ApJ, 526, 788

Lee, H.-H., Herbst, E., Pineau des Forets, G., Roueff, E., & Le Bourlot, J., Photodissociation of H_2_ and CO and time dependent chemistry in inhomogeneous interstellar clouds. 1996, A&A, 311, 690

Lemasle, B., Hajdu, G., Kovtyukh, V., et al., Milky Way metallicity gradient from Gaia DR2 F/1O double-mode Cepheids. 2018, A&A, 618, A160

Leung, C. M., Herbst, E., & Huebner, W. F., Synthesis of complex molecules in dense interstellar clouds via gas-phase chemistry - A pseudo time-dependent calculation. 1984, ApJS, 56, 231

Liszt, H., Gas-phase recombination, grain neutralization and cosmic-ray ionization in diffuse gas. 2003, A&A, 398, 621

Mac Low, M.-M. & Klessen, R. S., Control of star formation by supersonic turbulence. 2004, Reviews of Modern Physics, 76, 125

Mac Low, M.-M., Klessen, R. S., Burkert, A., & Smith, M. D., Kinetic Energy Decay Rates of Supersonic and Super-Alfvénic Turbulence in Star-Forming Clouds. 1998, Physical Review Letters, 80, 2754

Mackey, J., Walch, S., Seifried, D., et al., Non-Equilibrium Chemistry and Destruction of CO by X-ray Flares. 2018, ArXiv e-prints

Mardones, D., Myers, P. C., Tafalla, M., et al., A Search for Infall Motions toward Nearby Young Stellar Objects. 1997, ApJ, 489, 719

McElroy, D., Walsh, C., Markwick, A. J., et al., The UMIST database for astrochemistry 2012. 2013, A&A, 550, A36

McKee, C. F. & Ostriker, J. P., A theory of the interstellar medium: three components regulated by supernova explosions in an inhomogeneous substrate. 1977, ApJ, 218, 148

Micic, M., Glover, S. C. O., Federrath, C., & Klessen, R. S., Modelling H_2 formation in the turbulent interstellar medium: solenoidal versus compressive turbulent forcing. 2012, MNRAS, 421, 2531

Motte, F., Andre, P., & Neri, R., The initial conditions of star formation in the rho Ophiuchi main cloud: wide-field millimeter continuum mapping. 1998, A&A, 336, 150

Motte, F., Nguyên Luong, Q., Schneider, N., et al., The formation of the W43 complex: constraining its atomic-to-molecular transition and searching for colliding clouds. 2014, A&A, 571, A32

Myers, P. C., Dense cores in dark clouds. III. Subsonic turbulence. 1983, ApJ, 270, 105

Myers, P. C., Filamentary Structure of Star-forming Complexes. 2009, ApJ, 700, 1609

Nelson, R. P. & Langer, W. D., The Dynamics of Low-Mass Molecular Clouds in External Radiation Fields. 1997, ApJ, 482, 796

Nelson, R. P. & Langer, W. D., On the Stability and Evolution of Isolated BOK Globules. 1999, ApJ, 524, 923

Oort, J. H., Outline of a theory on the origin and acceleration of interstellar clouds and O associations. 1954, Bulletin of the Astronomical Institutes of the Netherlands, 12, 177

Padoan, P., Bally, J., Billawala, Y., Juvela, M., & Nordlund, Å., Supersonic Turbulence in the Perseus Molecular Cloud. 1999, ApJ, 525, 318

Padoan, P., Haugbølle, T., Nordlund, Å., & Frimann, S., Supernova Driving. IV. The Star-formation Rate of Molecular Clouds. 2017, ApJ, 840, 48

Padoan, P., Pan, L., Haugbølle, T., & Nordlund, Å., Supernova Driving. I. The Origin of Molecular Cloud Turbulence. 2016, ApJ, 822, 11

Padovani, M., Ivlev, A. V., Galli, D., & Caselli, P., Cosmic-ray ionisation in circumstellar discs. 2018, A&A, 614, A111

Pardi, A., Girichidis, P., Naab, T., et al., The impact of magnetic fields on the chemical evolution of the supernova-driven ISM. 2017, MNRAS, 465, 4611

Peretto, N., Fuller, G. A., Duarte-Cabral, A., et al., Global collapse of molecular clouds as a formation mechanism for the most massive stars. 2013, A&A, 555, A112

Peters, T., Naab, T., Walch, S., et al., The SILCC project - IV. Impact of dissociating and ionizing radiation on the interstellar medium and Hα emission as a tracer of the star formation rate. 2017, MNRAS, 466, 3293

Phillips, T. G. & Huggins, P. J., Abundance of atomic carbon /C I/ in dense interstellar clouds. 1981, ApJ, 251, 533

Price, D. J., Smoothed particle hydrodynamics and magnetohydrodynamics. 2012, Journal of Computational Physics, 231, 759

Reynolds, R. J., Scherb, F., & Roesler, F. L., Observations of Diffuse Galactic HA and [n II] Emission. 1973, ApJ, 185, 869

Rolleston, W. R. J., Smartt, S. J., Dufton, P. L., & Ryans, R. S. I., The Galactic metallicity gradient. 2000, A&A, 363, 537

Röllig, M., Abel, N. P., Bell, T., et al., A photon dominated region code comparison study. 2007, A&A, 467, 187

Roman-Duval, J., Jackson, J. M., Heyer, M., Rathborne, J., & Simon, R., Physical Properties and Galactic Distribution of Molecular Clouds Identified in the Galactic Ring Survey. 2010, ApJ, 723, 492

Safranek-Shrader, C., Krumholz, M. R., Kim, C.-G., et al., Chemistry and radiative shielding in star-forming galactic discs. 2017, MNRAS, 465, 885

Salomé, Q., Salomé, P., Combes, F., & Hamer, S., Atomic-to-molecular gas phase transition triggered by the radio jet in Centaurus A. 2016, A&A, 595, A65

Scalo, J. & Elmegreen, B. G., Interstellar Turbulence II: Implications and Effects. 2004, ARA&A, 42, 275

Seifried, D. & Walch, S., Modelling the chemistry of star-forming filaments - I. H_2 and CO chemistry. 2016, MNRAS, 459, L11

Seifried, D., Walch, S., Girichidis, P., et al., SILCC-Zoom: the dynamic and chemical evolution of molecular clouds. 2017, MNRAS, 472, 4797

Sembach, K. R., Howk, J. C., Ryans, R. S. I., & Keenan, F. P., Modeling the Warm Ionized Interstellar Medium and Its Impact on Elemental Abundance Studies. 2000, ApJ, 528, 310

Smith, R. J., Glover, S. C. O., Bonnell, I. A., Clark, P. C., & Klessen, R. S., A quantification of the non-spherical geometry and accretion of collapsing cores. 2011, MNRAS, 411, 1354

Solomon, P. M., Rivolo, A. R., Barrett, J., & Yahil, A., Mass, Luminosity, and Line Width Relations of Galactic Molecular Clouds. 1987, ApJ, 319, 730

Spitzer, L. 1978, Physical processes in the interstellar medium

Stecher, T. P. & Williams, D. A., Photodestruction of Hydrogen Molecules in H I Regions. 1967, ApJ, 149, L29

Stéphan, G., Schilke, P., Le Bourlot, J., et al., Chemical modeling of internal photon-dominated regions surrounding deeply embedded HC/UCHII regions. 2018, A&A, 617, A60

Stone, J. M., Ostriker, E. C., & Gammie, C. F., Dissipation in Compressible Magnetohydrodynamic Turbulence. 1998, ApJ, 508, L99

Stutzki, J. & Guesten, R., High spatial resolution isotopic CO and CS observations of M17 SW - The clumpy structure of the molecular cloud core. 1990, ApJ, 356, 513

Szűcs, L., Glover, S. C. O., & Klessen, R. S., The ^{12}CO/^{13}CO ratio in turbulent molecular clouds. 2014, MNRAS, 445, 4055

Tielens, A. G. G. M. & Hollenbach, D., Photodissociation regions. I. Basic model.

1985, ApJ, 291, 722

Truelove, J. K., Klein, R. I., McKee, C. F., et al., The Jeans Condition: A New Constraint on Spatial Resolution in Simulations of Isothermal Self-gravitational Hydrodynamics. 1997, ApJ, 489, L179

Valdivia, V., Hennebelle, P., Gérin, M., & Lesaffre, P., H_2 distribution during the formation of multiphase molecular clouds. 2016, A&A, 587, A76

van Dishoeck, E. F. & Black, J. H., The photodissociation and chemistry of interstellar CO. 1988, ApJ, 334, 771

van Leer, B., Towards the ultimate conservative difference scheme. V. A second-order sequel to Godunov's method. 1979, Journal of Computational Physics, 32, 101

Vázquez-Semadeni, E., Gómez, G. C., Jappsen, A. K., et al., Molecular Cloud Evolution. II. From Cloud Formation to the Early Stages of Star Formation in Decaying Conditions. 2007, ApJ, 657, 870

Vietri, M., Ferrara, A., & Miniati, F., The Survival of Interstellar Clouds against Kelvin-Helmholtz Instabilities. 1997, ApJ, 483, 262

Vishniac, E. T., Nonlinear instabilities in shock-bounded slabs. 1994, ApJ, 428, 186

Waagan, K., Federrath, C., & Klingenberg, C., A robust numerical scheme for highly compressible magnetohydrodynamics: Nonlinear stability, implementation and tests. 2011, Journal of Computational Physics, 230, 3331

Walch, S., Girichidis, P., Naab, T., et al., The SILCC (SImulating the LifeCycle of molecular Clouds) project - I. Chemical evolution of the supernova-driven ISM. 2015, MNRAS, 454, 238

Walch, S., Wünsch, R., Burkert, A., Glover, S., & Whitworth, A., The Turbulent Fragmentation of the Interstellar Medium: The Impact of Metallicity on Global Star Formation. 2011, ApJ, 733, 47

Walmsley, C. M. & Ungerechts, H., Ammonia as a molecular cloud thermometer. 1983, A&A, 122, 164

Ward-Thompson, D., André, P., & Kirk, J. M., The initial conditions of isolated star formation - V. ISOPHOT imaging and the temperature and energy balance of prestellar cores. 2002, MNRAS, 329, 257

Williams, J. P., Blitz, L., & McKee, C. F. 2000, in Protostars and Planets IV, ed. V. Mannings, A. P. Boss, & S. S. Russell, 97

Wolfire, M. G., Hollenbach, D., & McKee, C. F., The Dark Molecular Gas. 2010, ApJ, 716, 1191

Wolfire, M. G., Hollenbach, D., McKee, C. F., Tielens, A. G. G. M., & Bakes, E. L. O., The Neutral Atomic Phases of the Interstellar Medium. 1995, ApJ, 443, 152

Wolfire, M. G., McKee, C. F., Hollenbach, D., & Tielens, A. G. G. M., Neutral Atomic Phases of the Interstellar Medium in the Galaxy. 2003, ApJ, 587, 278

Wünsch, R., Walch, S., Dinnbier, F., & Whitworth, A., Tree-based solvers for adaptive mesh refinement code FLASH - I: gravity and optical depths. 2018, MNRAS

Zuckerman, B. & Evans, II, N. J., Models of massive molecular clouds. 1974, ApJ, 192, L149

ACKNOWLEDGEMENTS

I am heartily thankful to my PhD advisor, Prof. Dr. Stefanie Walch-Gassner, who provided me the opportunity to pursue the PhD program at the University of Cologne. Her mentoring, suggestions, encouragement, advise, and care throughout the years made it possible for me to take another leap forward in my academic journey.

I would like to express my sincere gratitude towards Prof. Dr. Peter Schilke and Prof. Dr. Joachim Saur for accepting my request to be part of the thesis committee and oversee the completion of my PhD program.

I would like to extend my special gratitude towards S. C. O. Glover as this work would not have been possible without the chemistry network he and his colleagues presented to the astrophysical community. I thank him for his encouraging comments and guiding notes during the preparation of the paper.

I specially thank Daniel Seifried, Sebastian Haid, Anuraag Shakya, and Seamus Clarke for their immense help to bring the thesis to its present form.

I am grateful to Annika Franeck, Daniel Seifried, and Sebastian Haid, the first three of the colleagues and friends with whom my PhD life began in Cologne; I thank them for their support at work and beyond for all these years. I am thankful to all my colleagues in the work-group of Prof. Walch and in the I. Physikalisches Institut for the wonderful moments during meetings, colloquiums, get-togethers, institute retreats, and celebrations.

I dedicate this work to my parents and sisters, whose love, care, and support keeps me happy, content, and inspired.

SELBSTSTÄNDIGKEITSERKLÄRUNG

Ich versichere, dass ich die von mir vorgelegte Dissertation selbständig angefertigt, die benutzten Quellen und Hilfsmittel vollständig angegeben und die Stellen der Arbeit -einschließlich Tabellen, Karten und Abbildungen-, die anderen Werken im Wortlaut oder dem Sinn nach entnommen sind, in jedem Einzelfall als Entlehnung kenntlich gemacht habe; dass diese Dissertation noch keiner anderen Fakultät oder Universität zur Prüfung vorgelegen hat; dass sie -abgesehen von den angegebenen Teilpublikationen- noch nicht veröffentlicht worden ist, sowie, dass ich eine solche Veröffentlichung vor Abschluss des Promotionsverfahrens nicht vornehmen werde. Die Bestimmungen der Promotionsordnung sind mir bekannt. Die von mir vorgelegte Dissertation ist von Prof. Dr. Stefanie Walch-Gassner betreut worden.

Köln, den 12.02.2019

(..............................)

TEILPUBLIKATIONEN

The publication that preceded this thesis work is listed below. Both the underlying research and the manuscripts of the publication were largely authored by first author P. R. Joshi. The scientific advisors of P. R. Joshi, S. Walch and D. Seifried, were involved in the scientific discussion from the beginning of the PhD work. The helpful contribution from each co-author improved the quality of both the analysis of the results and the conclusion from the research presented in the paper. This peer-reviewed publication was further strengthened by the insightful comments from the anonymous referee.

Joshi, P. R., Walch, S., Seifried, D., et al., *On the resolution requirements for modelling molecular gas formation in solar neighbourhood conditions.* 2019, MNRAS, 484, 1735

The thesis project was carried out with the support from the DFG through SFB 956 sub-project C5. The software used in this work was in part developed by the

DOE NNSA-ASC OASCR Flash Center at the University of Chicago[1]. I gratefully acknowledge the Gauss Centre for Supercomputing e.V. (`www.gauss-centre.eu`) for supporting this project by providing 10 million CPU hours of computing time on the GCS Supercomputer SuperMUC at Leibniz Supercomputing Centre (`www.lrz.de`). I thank the Regional Computing Center of the University of Cologne (RRZK) for providing computing time and support on the DFG-funded High Performance Computing (HPC) system CHEOPS. I am also thankful to VisIt (Childs et al. 2012) which allowed to produce the volume-rendered images.

The co-authors of the paper, SW and SDC acknowledge funding by the European Research Council through the ERC Starting Grant “RADFEEDBACK: The radiative ISM" (project number 679852). Similarly, SW and SCOG acknowledge the support of the DFG via the SPP 1573, “Physics of the Interstellar Medium” (grant number GL 668/2-1). SCOG acknowledges support from the DFG via SFB 881, “The Milky Way System” (sub-projects B1, B2 and B8). SCOG also acknowledges support from the European Research Council under the European Community’s Seventh Framework Programme (FP7/2007 - 2013) via the ERC Advanced Grant “STARLIGHT: Formation of the First Stars” (project number 339177).

---

[1] FLASH is available at `http://www.flash.uchicago.edu/`

Prabesh Raj Joshi

I. Physikalisches Institut
University of Cologne
Zuelpicher Str. 77
50937 Cologne
Germany
pjoshi@uni-koeln.de

Nationality	Nepalese
Date of Birth	27/10/1991

Education

07/2015 to 03/2019	**I. Physikalisches Instiut, University of Cologne, Cologne, Germany** Pursuing PhD in Astrophysics Scheduled defense : March 2019
08/2013 – 06/2015	**Jacobs University Bremen, Bremen, Germany** Msc Physics Thesis topic: Test Particle Motion in the Space-time of Charged Black Hole Pierced by a Cosmic String
08/2010 – 06/2013	**Jacobs University Bremen, Bremen, Germany** BSc Physics Thesis topic: Controlling Pattern Formation in Systems of Bistable Frustrated Units
07/2007 – 07/2009	**Prasadi Academy Higher Secondary School, Lalitpur, Nepal** Higher Secondary Education in Natural Sciences.

Research and Project Experience

Joshi, P. R., Walch, S., Seifried, D., et al., On the resolution requirements for modelling molecular gas formation in solar neighbourhood conditions. 2019, MNRAS, 484, 1735

Test Particle Motion in the Space-time of Charged Black Hole Pierced by a Cosmic String, Jacobs University Bremen/Universität Bremen, Germany

Graduate thesis project.

Supervisors: Prof. Dr. Betti Hartmann, University of São Paulo, Brazil
Dr. Eva Hackmann of ZARM, Universität Bremen

Controlling Pattern Formation in Systems of Bistable Frustrated Units, Jacobs University Bremen, Germany

Undergraduate thesis project.

Supervisor: Prof. Dr. Hildegard Meyer-Ortmanns.